# A new strategy for change detection in SAR time-series : application to target detection

Thibault Taillade

Thèse de doctorat

NNT: 2020UPAST050

université PARIS-SACLAY

# A New Strategy for Change Detection in SAR Time-series: Application to Target Detection

**Thèse de doctorat de l'Université Paris-Saclay**

École doctorale n° 575, Electrical, optical, biophysics and engineering (EOBE)
Spécialité de doctorat : Electronique et Optoélectronique, Nano- et Microtechnologies
Unité de recherche : Université Paris-Saclay, CentraleSupélec, ONERA, SONDRA, 91190, Gif-sur-Yvette, France.
Référent : CentraleSupélec

**Thèse présentée et soutenue à Gif-sur-Yvette, le 3 Décembre 2020, par**

**Thibault TAILLADE**

**Composition du jury:**

| | |
|---|---|
| **René GARELLO**<br>Professeur, IMT Atlantique | Président & Rapporteur |
| **Guillaume GINOLHAC**<br>Professeur, Université Savoie Mont-Blanc | Rapporteur & Examinateur |
| **André BEAUDOIN**<br>Chercheur scientifique, Ressources naturelles Canada, Service canadien des forêts (Québec, Canada) | Examinateur |
| **Elise COLIN-KOENIGER**<br>Ingénieur de recherche, ONERA | Examinatrice |
| **Irena HAJNSEK**<br>Professeur, ETH Zurich et DLR | Examinatrice |
| **Régis GUINVARC'H**<br>Professeur, CentraleSupélec | Encadrant & Examinateur |
| **Laetitia THIRION-LEFEVRE**<br>Professeur adjoint, CentraleSupélec | Directrice de thèse |

# Acknowledgements

I am thankful for everyone's support that contributed in some way to this thesis.
First of all, I would like to express my deep gratitude and sincere thanks to my two supervisors Laetitia and Régis. Their mentorship, suggestions, remarks, and time for discussion have been the main support for the completion of this thesis.
I want to thank my Ph.D. defense committee members who accepted to evaluate my thesis and be part of the defense, even considering the complicated circumstances we faced this year 2020. I thank the jury president, René Garello, who remotely chaired my Ph.D defense and made sure that the questions session runs smoothly. I thank again René Garello and Guillaume Ginolhac to review my manuscript and proposed valuable precisions and improvements. I am thankful to Irena Hanjsek, Elise Colin-Koeniger and André Beaudoin for their interesting questions and discussions.
Being three years in the laboratory SONDRA made me discover a wonderful team in a great work environment. I am thankful to Sylvain and Stéphane, who welcomed me in the laboratory. Virginie, not to mention the support and help you provided me through these three years, I would like to point out that you are a great driving teacher. I am deeply grateful to have shared discussion and time with Thierry, Jean-Philippe, Israel and Chengfang. I want to thank the postdoctorate and Ph.D students that welcomed me in the laboratory: Marie-José, Eugénie, Pedro, Ahmad, Uyhour, Orian, Ammar and Vlad. I had the chance to be part with Bruno to a research exchange with the National University of Singapore, I thank him for these great moments spent in his company in Singapore and at SONDRA. I thank as well Koen and Ken Yoong to have helped me during my stay in CRISP laboratory. These three years would have been different without Giovanni that I sincerely thank for everything. I would also like to thank Nathan for this last year in his company and wish him good luck for the rest of his thesis. Finally, I would like as well to wish the best for the new Ph.D. students Dihia, Augustin, Antoine, Cyprien, Thomas and Florent.
Finally, I would like to thank my wife and my family for all their support during my thesis.

# List of Symbols

| | |
|---|---|
| $s^{pq}$ | Complex value of a pixel with polarisation p and q |
| $\alpha^{pq}$ | Amplitude of a pixel with polarisation p and q |
| $\sigma^{pq}$ | Intensity of a pixel with polarisation p and q |
| $\mathbf{x}$ | Polarimetric vector in Sinclair basis |
| $\mathbf{y}$ | Polarimetric vector in Pauli basis |
| $\mathbf{C}$ | Sample covariance matrix (from Sinclair vector) |
| $\mathbf{T}$ | Sample coherence matrix (from Pauli vector) |
| $CV(\bullet)$ | Variation Coefficient of temporal samples |
| $\langle\bullet\rangle_N$ | average over N pixels |
| $\lvert\bullet\rvert$ | Determinant of matrix |
| $tr(\bullet)$ | Trace operator |
| $E[\bullet]$ | Esperance operator |
| $\psi$ | Threshold |
| $L$ | Number of looks |
| $D$ | Number of images |
| $D'$ | Number of candidate acquisitions |
| $\gamma_{GM}$ | GLRT omnibus test |
| $\gamma_G$ | GLRT bi-temporal |
| $\gamma_{MP}$ | GLRT test between MP selected FBR image and a mission image |
| $\gamma_{RP}$ | GLRT test between RP selected FBR image and a mission image |

# Abbreviations

| | |
|---|---|
| NLOS | Non-line-of-sight |
| CD | Change Detection |
| SAR | Synthetic Aperture Radar |
| CFAR | Constant False Alarm Rate |
| UAVSASR | Uninhabited Aerial Vehicle Synthetic Aperture Radar |
| NASA | National Aeronautics and Space Administration |
| DLR | Deutsches Zentrum Luft− und Raumfahrt |
| ESA | European Space Agency |
| RCS | Radar Cross Section |
| GRD | Ground Range Detected |
| SNR | Single-to-noise ratio |
| FBR | Frozen Background Reference |
| RP | Random pixel |
| MP | Multi-temporal pixel |
| GLRT | Generalized Likelihood Ratio Test |
| CV | Variation Coefficient |
| PD | Probability of detection |
| PFA | Probability of false alarms |

# Introduction

## Context of the study

This thesis deals with SAR (Synthetic Aperture Radar) change detection in noisy environments, such as forests, cities, or harbors, with multiple interactions. We want to detect the changes associated with small and potentially mobile objects such as vehicles or boats. In these configurations, targets' detection is challenging due to the strong backscattering signal of surrounding natural or man-made structures. Besides, multiple interactions between the targets and their surrounding environment may lead to multiple signatures - even for a single target - and then to a confusing position of these signatures within the SAR images. For instance, in urban areas, these signatures may be associated with target-wall or target-ground scattering mechanisms. Also, when the target is quite large compared to the wavelength and the resolution, different parts may be involved: the roof, the side, the front, or the back of this target. It typically occurs when the target is in NLOS (Non-Line Of Sight) for the antenna, as illustrated in [1]. In this previous study, simple change detection techniques have been first applied on simulated radar data, then on anechoic chamber measurements mocking a vehicle parked between two buildings. Without prior knowledge, it was not possible to retrieve nor the number of targets nor their locations. These configurations were relatively simple and, above all, without any additional contributions, not even noise. However, all the structures and the target were simulated or built as metallic objects, reinforcing the intensity of the multiple interactions. Our question was then to determine what we would obtain in real conditions.

To investigate this question, we have to find data set combining high-resolution SAR data with a detailed description of the scene. Also, to enable the phenomenology study, we looked for polarimetric SAR images.

These conditions were fulfilled in [2] or [3] for instance. The objects to be detected inside forests

(vehicles and corner reflectors) were assumed to be composed of metallic plates with various orientations. A subspace characterizing the radar signatures of these metallic plates with diverse orientations was then built. Another one was elaborated corresponding to the contributions of the double-bounce scattering mechanism associated with the trunks. The received signal was first projected on the target subspace and then cleared of its component belonging to the trunk subspace. This technique was developed specifically for FoPen (Foliage Penetration) applications in an environment with a low density of targets, where the difficulty was to separate two contributions that could be easily modeled. However, this method required prior knowledge of the targets and their environment. Besides, it has not been tested with a high density of scatterers, as in cities. The work developed in [2] or [3] illustrates what can be done in target detection with a single image when a criterion exists to differentiate the targets from their surrounding environments.

Another strategy may be used for target detection, based on change detection between two or more SAR images. In this case, supposing that an image without any target is available, the change detection between this SAR image (reference image) and another SAR image (mission image) with possible targets enables the cancellation of the background and highlights the targets of interest.

We illustrate in Figure 1 some scenarios where targets are present in SAR images. In Figure 1a, we can observe a ship circled in green that represents a simple case of detection since this target is surrounded by sea. In that case, the usual CFAR detector [4] using a single SAR image would detect it. On the contrary, the ship circled in blue is more challenging to detect because it is adjacent to a strong scatterer (metallic mooring quay). Change detection would offer a better detection in that case because the mooring quay contribution would be canceled. These aspects will be investigated and introduced in Chapter 7 for maritime surveillance applications.
We illustrate in Figure 1b another case where targets are hidden under the canopy. This case represents a critical situation where CD techniques showed to be a good candidate to detect such targets. These aspects will be investigated and introduced in Chapter 8 for FoPen (Foliage Penetration) applications.

Change Detection is appropriate to highlight targets within an observed scene containing strong scatterers because the background environment is canceled. However, the choice of CD strategies implies to have ideal access to a target-free scene. Specific campaigns for target detection can provide such scenes and a detailed ground truth that enables to evaluate the detection [5, 6]. However, in practice, the contents of a scene at a specific date are unknown in open-access SAR images (e.g., Sentinel 1, UAVSAR). In that case, the change detection results between two or more scenes may be ambiguous if a target is present several days or when targets of different natures are occupy-

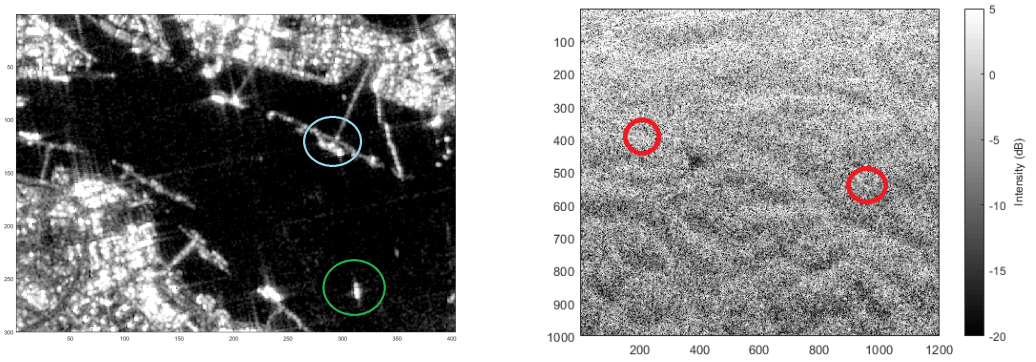


(a) Radiometric SAR image acquired with Sentinel-1 at VV polarization on the 22nd of August 2020.

(b) Radiometric SAR image acquired at HH polarization during the TROPISAR mission.

Figure 1: SAR images with targets: (a) ships visible on a radiometric SAR image collected with Sentinel-1 at VV polarization, on the 22nd of August 2020; (b) Vehicles hidden under foliage in TROPISAR mission SAR image 402 at HH polarization.

ing the same geographic position during several acquisitions (partial or total temporal overlapping).

**In this Ph.D. thesis, we assume that any SAR image consists of immobile objects (e.g., buildings and trees) that are permanently present in the SAR images and ephemeral objects (targets) that can appear and disappear from one acquisition to another (e.g., cars and ships). We propose to exploit open-access SAR time-series to define and compute a reference SAR image only containing what is temporally stable or permanent within the scene at the pixel level. We will then perform CD with this FBR (Frozen Background Reference) image to highlight the targets present at a given mission image. With this technique, we expect to be able to isolate and analyze the targets' signature.**

## Organisation of the manuscript

The first part comprises three chapters that introduce the key elements for the understanding and the analysis of SAR images, present the main datasets used during the study and finally illustrate the different strategies of change detection in SAR time-series. The second part presents the FBR image concept, its computation, representation, and the associated change detection strategy adopted. Finally, the last part, composed of two chapters, presents the applications of our method on two constraining environments for target detection: maritime surveillance in harbor environments and detection of targets in FoPen contexts.

# Contents

# List of Figures

# List of Tables

# Part I

# Generalities on SAR imaging and change detection in SAR time-series

In this part is presented in a first chapter an overview of SAR principles and applications to ease the understanding of the thesis. The main parameters of SAR imaging systems will be presented in the geometrical, physical and statistical aspects. In a second chapter, we present the datasets collected and processed to conduct temporal analysis. In the third chapter, change detection strategies in SAR time-series are presented and the problematic of target detection in SAR images is considered.

**Content of the part I** :

- Chapter 1 : Synthetic Aperture Radar Overview
- Chapter 2 : Preparation and presentation of datasets used for the thesis
- Chapter 3: Introduction to change detection in SAR time-series: applications to target detection

# Chapter 1

# Synthetic Aperture Radar Overview

**Objectives**:
In this chapter, we present the key elements for the understanding and the analysis of SAR images. We will introduce first the potential of SAR imaging in different domains of application. Afterward, technical aspects and most significant parameters of SAR sensors will be presented such as operating frequency, spatial resolution and polarisation. Finally the associated statistical consideration of SAR images will be approached.

Synthetic aperture radar (SAR) is a high-resolution airborne or spaceborne remote sensing technique that produces an image illustrating the capability of a scene to reflect toward the radar the emitted EM (Electromagnetic) waves. Carl Wiley discovered in 1950's the principle of SAR imaging by investigating the Doppler spectrum of the received echos when using a moving radar along a straight direction. This movement during the acquisition enables indeed the synthesis of a long aperture antenna. This patent was issued in 1954 and became the starting point of research and development on SAR remote sensing imaging techniques [18]. After, the first airborne SAR image has been acquired in Florida using a C-46 aircraft [19] and the first on-board satellite SAR system, Seasat, was launched in 1978 by the National Aeronautics and Space Administration (NASA) with a mission duration of 105 days. Since then, several countries and consortium of countries launched their own SAR satellites.

Figure 1.1a presents the diversity of previous, current, and expected SAR satellite missions for different frequency bands of acquisition and operating time. We can notice from Figure 1.1a that

we are currently experiencing an explosion of SAR sensors commissioning in all frequency bands.

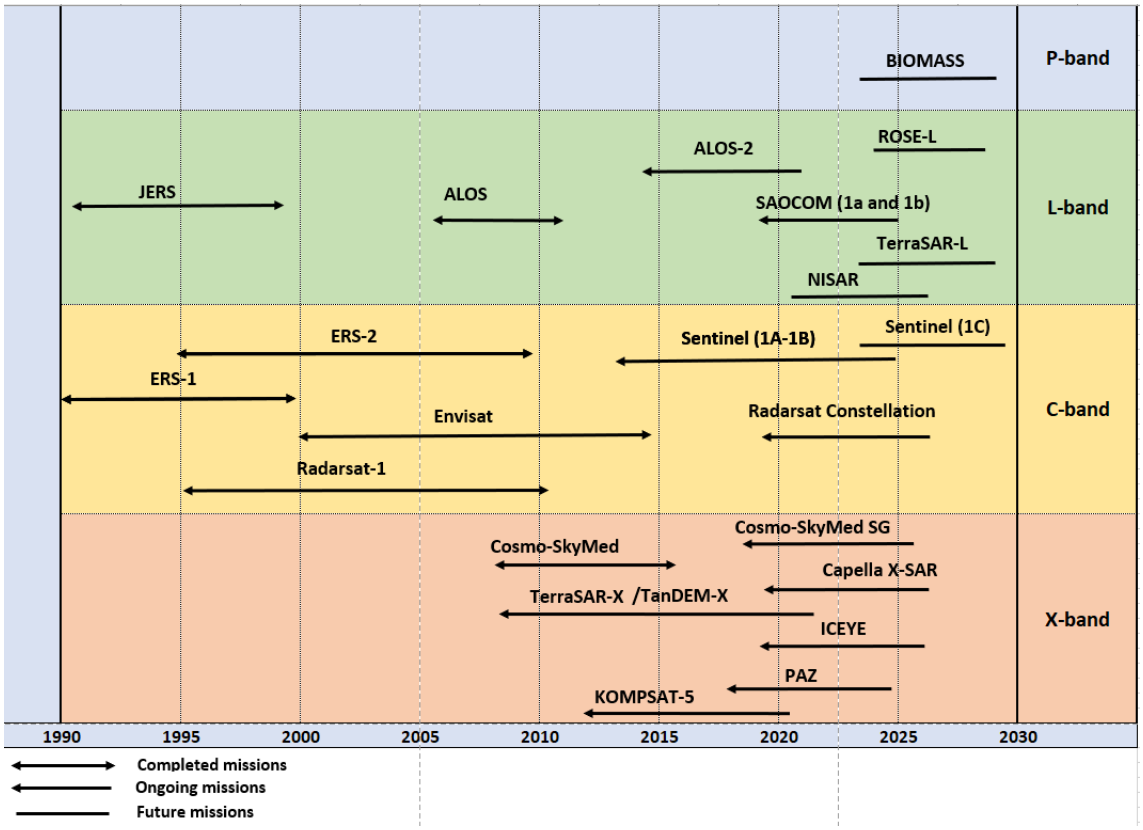


(a) Satellite sensors overview : past, current and future SAR missions

| Frequency band | Frequency range (GHz) | Typical Wavelength | Application |
|---|---|---|---|
| Ka | 27 to 47 | 1 cm | High resolution imaging |
| Ku | 14 to 18 | 2 cm | Glacier study (snow cover mapping) |
| X | 8 to 12 | 3 cm | Agriculture, ocean study |
| C (includes S) | 2 to 8 | 5 cm | |
| L | 1 to 2 | 25 cm | Foliage/Ground Penetration, Biomass study, Desert sub-surface study |
| P | 0.3 to 1 | 50 cm | |
| UHF | 0.03 to 0.3 | 1m | |
| VHF | <0.3 | >5m | |

(b) Typical Radar frequencies and applications

Figure 1.1: Satellite sensors overview and typical usage for different SAR frequencies :

Soon, the first P-band spaceborne measurements will be achieved with the Biomass satellite [20] (theoretically to be launched in 2022) and other satellites will be commissioned within already exploited bands. Regarding L-band satellite missions, NISAR (NASA), ROSE-L (ESA: European Space Agency) and TerraSAR-L (DLR: Deutsches Zentrum für Luft- und Raumfahrt or German Aeropsace Center) will be likely commissioned in the next years (2021-2022). Constellation of SAR satellites are being launched in C and S-band: Radarsat Constellation mission (CSA: Canadian Space Agency) and NovaSAR (UK Space Agency) that are mainly considered for maritime surveillance and operate with a small revisit time (expected daily monitoring). Finally, several X-band

micro-satellites constellations are emerging, such as Capella X-SAR (Capella) and ICEYE (ICEYE Oy), with an unprecedented expected revisit time of one hour when the full constellation is used. This expected revisit time has to be compared with 12 or 6 days revisit time of classical sensors such as Sentinel 1-A and 1-B that represents already an excellent opportunity to monitor earth continuously in different domains. The field of applications are numerous and evolving extremely fast :

- Agriculture (e.g: Crop monitoring)
- Disaster and hazards (e.g :flooding, volcano eruption, landslides, earthquakes, oil spill incident)
- Defense (e.g: Surveillance),
- Geology (e.g: topographic changes, desert subsurface investigation and soil moisture),
- Urban development,
- Ecology (e.g: Biomass measurements and land cover classification)
- Environmental Science (e.g: Glacier evolution studies)
- Oceanography (e.g: current, winds, ocean surface features studies)

From Figure 1.1a, we can observe that the C-band was extensively used before 2010 for satellite SAR missions. One reason might be because it represents an average radar frequency that is a good trade-off between weather robustness and relative penetration within canopy. This enables a plurality of applications in crop monitoring, for example, that would be more challenging using L-band or P-band. Urban or maritime surveillance are also possible applications where C-band is a good candidate. However, the demand increasing in different domains shows an overall coverage of the radar spectrum in the last few years to fulfill the requirements of specific applications more accurately.

## 1.1 Why using SAR imaging?

The main advantage of SAR remote sensing technologies compared to optical technologies relies in their ability to penetrate through clouds, smoke, heavy rain, and provide images during the night. However, it is known that ionospheric phenomenons affect the collected signals at low frequencies (under L-band) [21, 22]. On the contrary, for high frequencies (above X-band), some heavy rain can impact the measurements since those frequencies are also used to detect precipitations [22]. Figure 1.2 presents the estimated cloud coverage over different regions of the world using the cloud products of MODIS optical sensors and Google Earth Engine. Using cloud flag pixels [1],

[1] a binary mask corresponding to the presence of cloud a this pixel

it is possible to estimate (according to a revisit time of 2 days) the temporal cloud coverage for a given pixel at a given geographic position by calculating the ratio between the times where it was detected as cloud divided by the number of available optical images. The observations being collected over three years, we can consider that the representation in terms of cloud coverage is reasonably reliable. It is then not surprising to observe in Figure 1.2d that in the region of Gobabeb (Namib desert) the cloud coverage tends to 0%. In contrast, the cloud coverage in the region of Singapore is in average close to 90% as presented in Figure 1.2a. The region near Kourou in French Guiana is also an area subject to intensive cloud coverage as we can see in Figure 1.2b where we can estimate around 70 to 80% of cloud coverage in the region. Finally, San Francisco represents a middle case of cloud coverage, where 50% of the acquisitions have been detected as clouds.

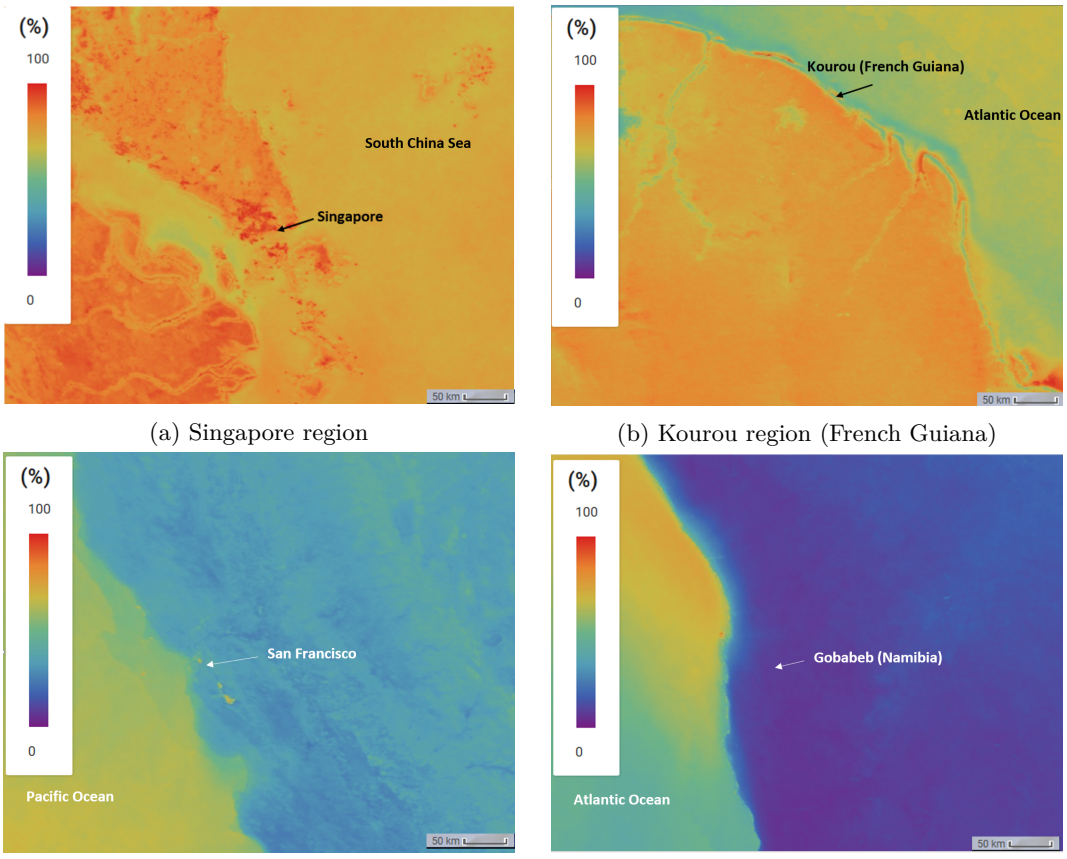


(a) Singapore region

(b) Kourou region (French Guiana)

(c) San Francisco region

(d) Gobabeb region (Namibia)

Figure 1.2: Cloud Coverage representation : calculated for each pixels as a percentage of pixels detected as cloud compared to the number of available temporal pixels from MODIS satellite (optical sensor) acquisitions in the period 2017-2019 processed with Google Earth Engine. (a) Kourou region (French Guiana), (b) Gobabeb region (Namibia), (c) Singapore region and (d) San Francisco region

The prominent presence of clouds is giving credit to the use of SAR sensors especially in tropical region where the percentage of usable images is around 10%. On the contrary, in arid areas such

as Namib desert, if the study rely on line of sight detection (not ground penetration required), the use of optical sensors only or combined with SAR sensors can be an asset since almost all data are usable. SAR sensors represent a rich source of physical information, however, the radar measuring by definition a distance, we will see that several drawbacks and artefacts can lead to misinterpretations. Depending on applications, we can understand that optical technologies or SAR technologies, or both combined can be used to obtain as much information as possible on the physical properties of the observed scene. In this thesis, only SAR images will be exploited, however, fusing technologies for earth observation is an interesting approach that is already being studied especially in land mapping applications [23, 24].

## 1.2 Acquisition Parameters and SAR image formation

Classical SAR systems are generally constituted of an antenna or a set of two close antennas performing the transmission and reception. It is therefore admitted that SAR sensors are monostatic measurement systems. As we can see on Figure 1.3, the sensor illuminate the scene and move at the same time with a constant speed Vs. The scene is illuminated with linear frequency modulated pulses called chirp during a pulse time Tc, creating a frequency diversity of bandwidth B under which the scene is observed. The pulses are emitted according to a given PRF (pulse repetition frequency) as shown in Figure 1.4a. The representation of such signal in temporal domain can be found in Figure 1.4b and in time-frequency domain in Figure 1.4c.

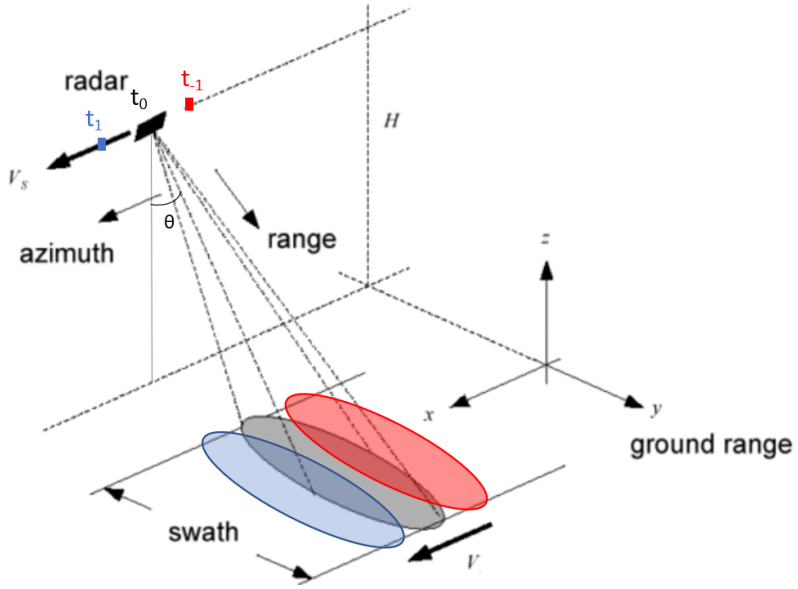


Figure 1.3: Classical Side looking SAR Geometry acquisition adapted from [7]

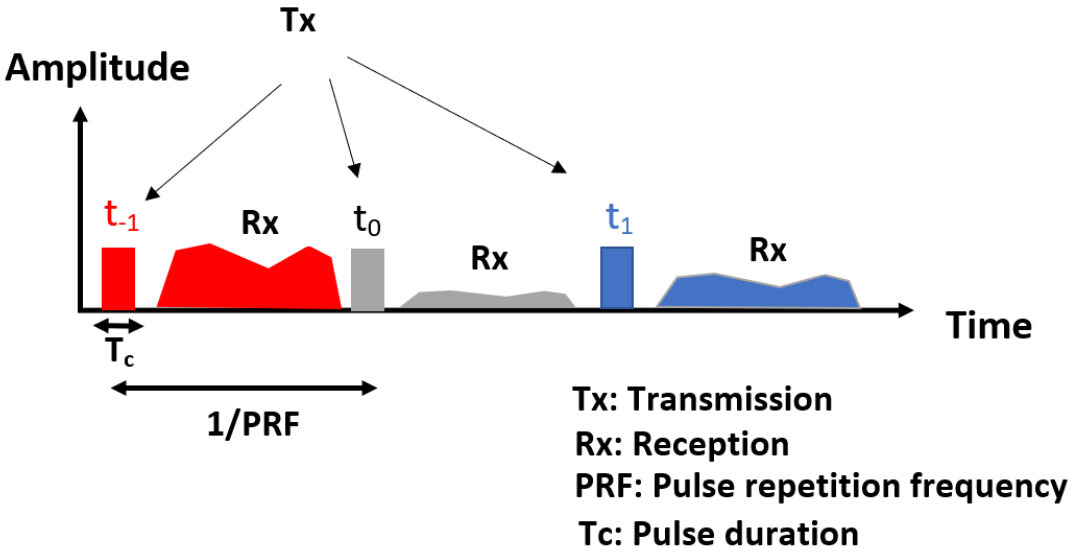


(a) Transmission and reception of SAR signals

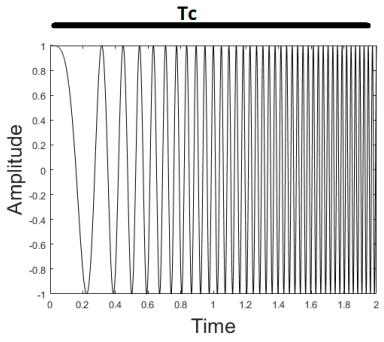


(b) Temporal visualisation of chirp signal

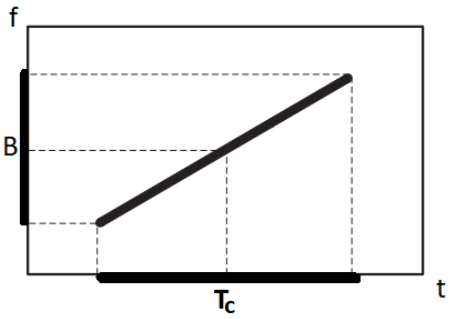


(c) Time/frequency representation of chirp signal

Figure 1.4: Transmission of SAR signals and representation of the chirp pulse : (a) Transmission and reception representation, (b) Chirp pulse representation in time domain and (c) Chirp pulse representation in time/frequency domain

Without going into the details of image reconstruction theory that is beyond the scope of this thesis. We can synthesize the reconstruction of a SAR image by exploiting two diversities during the acquisition: a frequency diversity brought by the chirp signal of bandwidth B and an angle diversity (squint angle) brought by the radial movement of the antenna beam along the observed scene. The acquisition of the same scene using these two diversities enables to generate a two-dimensional map representative of the backscattering capabilities of the illuminated scene. Several works thoroughly explains this principle as in [22, 25, 26, 27, 28].

### 1.2.1 Radar Cross Section and SAR imaging

The reflectivity of an object illuminated by a monochromatic wave is defined by $\sigma_{pq}$ its RCS (Radar Cross Section) in far field with p and q the polarisations:

$$\sigma_{qp} = \lim_{R \to +\infty} 4\pi R^2 \frac{|\overrightarrow{E^s_{qp}}|^2}{|\overrightarrow{E^i_q}|^2} \tag{1.1}$$

Where $\overrightarrow{E^s_{qp}}$ and $\overrightarrow{E^i_q}$ are the backscattered and incident electric field and R the distance between the radar and the target. The RCS is a function on the one hand of the shape, the orientation and the dielectric properties of the observed target and on the other hand of the frequency and the polarization of the emitted wave.

The aim of SAR systems is to obtain an image of the objects RCS within the observed scene. This can be theoretically achievable if the object is a white and isotrop scatterer ($\sigma_{qp}$ stationnary behavior in frequency and angle of observation) and in free space. The radiometric information of a pixel in SAR image cannot be strictly interpreted as the RCS of the object but as the result of the combination between the RCS of this object, other objects in the resolution cell and their interaction with their surroundings (environment for instance). The idea of extended target is then considered over an illuminated area $A_0$ and the averaged coherent contribution of all the scatterers is expressed with the dimensioneless scattering coefficient $\sigma_0$ [29]:

$$\sigma^0_{qp} = \lim_{R \to +\infty} \frac{4\pi R^2}{A_0} \frac{< |\overrightarrow{E^s_{qp}}|^2 >}{|\overrightarrow{E^i_q}|^2} \tag{1.2}$$

with "<>" the spatial averaging over the illuminated area.

### 1.2.2 SAR spatial resolution

Spatial resolution is one of the main parameters of interest when designing an application implying SAR images. This quantity represents the capability of the sensor to separate two closely spaced scatterers [29]. In classical SAR systems, a diversity in frequency (chirp signal) and in observation angle (synthetized array of antenna) is achieved giving the possibility to compute an image of the observed scene along two dimensions. The first dimension is called *slant range* or more usually *range* corresponds to LOS (line of sight) direction (perpendicular to the flight direction) and the second dimension is the *cross range (or azimuth, along track)* corresponds to the direction parallel to the flight direction. The slant range resolution $\Delta r$ (physical range resolution) and the ground

range resolution $\Delta r_x$ (slant range projected on the ground) are defined as following:

$$\Delta r = \frac{c}{2B} \text{ and } \Delta r_x = \frac{\Delta r}{sin\theta} \tag{1.3}$$

B representing the bandwidth of the acquisition (variation of frequency during the chirp), c the light speed and $\theta$ the incidence angle (angle between the middle of the swath and Nadir angle or z axis in the Figure 1.3). As we can see, the slant range resolution depends only on the bandwidth of the signal emitted during the pulse. This is a really interesting property and advantage to achieve high resolution imaging (sub-metric). The azimuthal resolution $\Delta r_y$ is defined as following :

$$\Delta r_y = \frac{R\lambda}{2L_S} \tag{1.4}$$

with $R$ the distance between the radar and the target, $\lambda$ the operating wavelength, $L_s$ the length of the synthetic antenna. These two parameters are essential when designing SAR applications and may be critical for target detection. As an example, the resolution of Sentinel 1 GRD images is approximately 20x20m which is in practice not possible to use in urban areas to detect vehicles. However, it is enough for maritime surveillance and ship detection as we will see in the thesis.

### 1.2.3 Operating frequency

As presented in Figure 1.1, several operating frequencies are used in SAR imaging. This is also a key parameter that enables to see different features of the observed scene leading to a variety of applications as shown in table 1.1b. The backscattering signal from objects within an illuminated scene is highly dependent on their shape and electromagnetic properties. Low frequencies will be preferred to penetrate through media, for desert subsurfaces studies [30] or biomass estimation [31], whereas higher frequencies will penetrate less and therefore can enable to monitor crops or ground surfaces. For biomass estimation, two opposite strategies can be however adopted. Using high frequencies (above C-band) would give the profile of the canopy and a possibility to link this height of vegetation with a biomass quantity [32]. It required however to have an accurate DEM (Digital Elevation Model) to obtain the actual height of the forest. On the contrary, using low frequencies would give more information about the interactions near the ground and under foliage structures. It is admitted that most of the biomass information is contained within the trunks and big branches of vegetation, so characterizing these contributions might link to a biomass informa-

tion [31]. This penetration property at low frequency is used for target detection in FoPen (Foliage Penetration) applications where the SAR operates at low frequencies (under L-band) to penetrate the foliage and reach the ground to detect concealed vehicles [33, 34].

### 1.2.4 NESZ (Noise Equivalent Sigma Zero)

Another important parameter in SAR imaging is the minimum backscattering signal that can be monitored by the sensor so that it will appear against the inherent noise. The parameter to measure the sensitivity of a SAR platform is called NESZ [22]:

$$NESZ = \frac{2(4\pi R)^3 V_s k_B T_0 B}{P_t G^2 \lambda^3 \Delta r_x PRF} \tag{1.5}$$

$R$ is the distance between the radar and the target, $k_B$ the Boltzmann's constant, $T_0$ the noise temperature, $P_t$ the transmitted power, G the gain of the antenna, $\lambda$ the operating wavelength and PRF the pulse repetition frequency. This quantity is a function of the range (function of the incidence angle) and vary depending on the senors but is typically between -25 and 30dB for satellite platforms. This quantity can be seen as the backscattered power of an observed plane surface without roughness.

### 1.2.5 Drawbacks of SAR imaging systems

We previously discussed on the benefits of SAR imaging systems that enable valuable robustness against weather and light conditions. However, there are artifacts that significantly affect the readability of SAR images. The artifacts in SAR images can be classified into two groups:

- Geometrical distortion
- Signal processing artefacts

The first group of artifacts is due to the geometry of the radar acquisition (side looking) and the scene. Those effects occur typically in mountainous regions or in urban areas with tall structures. The second group of artifacts is a consequence of the range and doppler spectrum signal processing while creating the SAR image as described in [35] and [36]. Some strong scatterers may be aliased in the azimuth spectrum generating ghost artifacts visible in low backscattering areas such as sea surface. This scenario is usually observed near harbor areas implying ghost signatures coming from high backscattering man-made infrastructures.

This section presented some key parameters and features of SAR data acquisition and image formation parameters. We introduced the advantages of SAR remote sensing systems compared to optical systems regarding the weather and light conditions. However, SAR systems suffer from physical and signal processing artifacts that are intrinsic to radar systems, sometimes rendering the interpretation of SAR images counter-intuitive. In the next section, we will present one specificity of SAR sensors that relies on polarimetric measurements of the observed scene.

## 1.3 Polarimetry

In this section, we introduce some elements of polarimetry that are frequently used in SAR applications. The scattering matrix will be presented as well as basic polarimetric decompositions that aim to decompose the polarimetric SAR signal into a basis that represent canonical physical mechanisms. Since the dielectric properties and the shapes of the scatterers describing the scene are diverse, the use of polarimetry is essential to highlight some canonical behaviors.

### 1.3.1 Scattering matrix

To simply understand how the scattering matrix is built, we consider a radar system that can emit and receive horizontally and vertically polarized waves. The polarized incident and received EM fields can be expressed using the Jones vectors $\mathbf{E}^i$ and $\mathbf{E}^s$ of respectively the incident and scattered EM fields [29]:

$$\mathbf{E}^i = \begin{bmatrix} E_H^i \\ E_V^i \end{bmatrix} \text{ and } \mathbf{E}^s = \begin{bmatrix} E_H^s \\ E_V^s \end{bmatrix} \tag{1.6}$$

$E_H^i$, $E_V^i$, $E_H^s$ and $E_V^s$ are the complex components of the incident and scattered fields, i stands for incident and s for scattered, H for horizontal and V for vertical component . The incident and baskcattered EM fields can be related in far field with the usual scattering Sinclair matrix $\mathbf{S}$ [29]:

$$\begin{bmatrix} E_H^s \\ E_V^s \end{bmatrix} = \frac{e^{-jkR}}{R}\mathbf{S}\begin{bmatrix} E_H^i \\ E_V^i \end{bmatrix} \text{ with } \mathbf{S} = \begin{bmatrix} s^{HH} & s^{HV} \\ s^{VH} & s^{VV} \end{bmatrix} \tag{1.7}$$

R is the distance between the receiving antenna and the target pixel, k the wavelength of the emitted wave, $s^{HH}$, $s^{HV}$, $s^{VH}$, and $s^{VV}$ the complex components of the scattering matrix that characterize the target under observation.

### 1.3.2 Polarimetric analysis

The purpose of polarimetric decomposition is to express the scattering matrix $\mathbf{S}$ into a combination of K matrices $\mathbf{S_k}$ that represent canonical scattering mechanisms so that :

$$\mathbf{S} = \sum_{k=1}^{K} \beta_k \mathbf{S_k} \tag{1.8}$$

$\beta_k$ represents the weight associated to each elementary matrix $\mathbf{S_k}$. This formalism enables to represent the elements of the scattering matrix $\mathbf{S}$ into different decomposition basis. In particular, for the purpose of the thesis, we will introduce two basis representation of the SAR signals: the lexicographic basis and the Pauli basis. Let consider the lexicographic basis, and define the vector $\mathbf{x}$ as:

$$\mathbf{x} = \begin{bmatrix} s^{HH} & s^{HV} & s^{VH} & s^{VV} \end{bmatrix}^T \tag{1.9}$$

T is defined as the transpose operator of a vector. In the Pauli basis, we will arrange the system of scattering matrix as following denoting $\mathbf{y}$ [37]:

$$\mathbf{y} = \frac{1}{\sqrt{2}} \begin{bmatrix} s^{HH} + s^{VV} & s^{HH} - s^{VV} & s^{HV} + s^{VH} & j(s^{HV} - s^{VH}) \end{bmatrix}^T \tag{1.10}$$

We can assume in remote sensing that $s^{HV} = s^{VH}$ because of the reciprocity. This lead to:

$$\mathbf{x} = \begin{bmatrix} s^{HH} & \sqrt{2}s^{HV} & s^{VV} \end{bmatrix}^T \tag{1.11}$$

In the Pauli basis $\mathbf{y}$ becomes:

$$\mathbf{y} = \frac{1}{\sqrt{2}} \begin{bmatrix} s^{HH} + s^{VV} & s^{HH} - s^{VV} & 2s^{HV} \end{bmatrix}^T \tag{1.12}$$

The covariance matrix $\mathbf{C}$ and the coherency matrix $\mathbf{T}$ are generally used to represent polarimetric SAR data. The matrix $\mathbf{C}$ is associated to the measurement vector in lexicographic basis $\mathbf{x}$, whereas the matrix $\mathbf{T}$ is associated with the measurement vector in Pauli basis $\mathbf{y}$. $\mathbf{C}$ and $\mathbf{T}$ are estimated in practice using temporal or spatial average samples of the measurement vectors in lexicographic or Pauli basis. These estimates are called sample covariances matrices (SCM) and expressed as follow:

$$\mathbf{C} = \langle \mathbf{x}\mathbf{x}^H \rangle_N = \frac{1}{N} \sum_{n=1}^{N} \mathbf{x}_n \mathbf{x}_n^H \text{ and } \mathbf{T} = \langle \mathbf{y}\mathbf{y}^H \rangle_N = \frac{1}{N} \sum_{n=1}^{N} \mathbf{y}_n \mathbf{y}_n^H \tag{1.13}$$

$\mathbf{C}$ and $\mathbf{T}$ are of size p × p with p the number of polarisation acquistions.

The use of the Pauli basis aims to link the measured signal with the following canonical contributions: the double bounce from a perfectly electrical conducting dihedral orientated toward the sensor (related to $|s^{HH} - s^{VV}|$), a direct scattering by a metallic trihedral ($|s^{HH} + s^{VV}|$) and the pure contribution from a rotated metallic dihedral ( related to $|s^{HV}|$ or $|s^{VH}|$. This contribution is often associated to volume scattering. With these assumptions, a color composition is performed to obtain polarimetric images that aim to highlight the properties of objects within the scene as shown in Figure 1.5. Therefore the red channel is usually associated with the double bounce mechanism, the blue channel with single bounce and the green channel with the cross polarisation channel. Using this color composition, it gives a "comprehensive" image that shows the vegetation in green (volume scattering), the buildings and infrastructures usually in purple (mix of blue and red) and the surface area like sea in dark blue color as shown in Figure 1.5. Framed in red, we can also observe an interesting phenomenon due to the orientation of buildings that reflect a more complex reality. The green areas are actually orientated buildings (tilted according to the radar path) that shows a behaviour similar to vegetation.

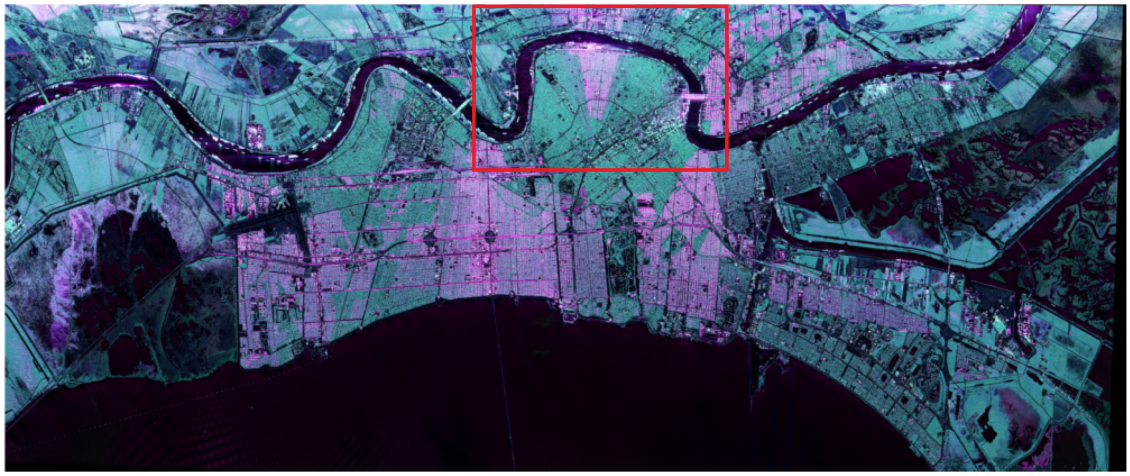

Figure 1.5: Example of a SAR image represented in the Pauli basis (double bounce in red, single scattering in blue and cross-polarisation in green) from [8]. Acquired by UAVSAR over New Orleans, Louisiana, US. The trajectory of the sensor is parallel to the top of the figure.

This is a recurrent problem in SAR polarimetric decomposition that produces wrong interpretation on the polarimetric SAR images. It is still one field of research where solutions are developed to describe in a more representative way the observed scene using electromagnetical properties of the object within the scene. In [8, 38] is presented studies highlighting this effect and recalling the importance of dielectric properties when signals from dihedral structures are collected by the sensor.

Several polarimetric decomposition has been developed such as Krogager decomposition using dif-

ferent canonical scattering mechanisms basis : a sphere, a dihedral and an helix [39]. Cameron decomposition exploits the symmetry and reciprocity of the scattering matrix **S** [40]. Finally, eigenvector-based decomposition have been introduced firstly in [41] and lead to the well known $H/A/\bar{\alpha}$ decomposition [29] that evaluate the dominance of mechanisms by using entropy information of coherence matrix eigenvalues. In [29] and [42] is presented thorough studies and developments on polarimetric decomposition for SAR acquisitions.

## 1.4 Statistical aspects

An intrinsic phenomenon resulting from all coherent measurement systems is called speckle noise. SAR imaging systems, being coherent measurement devices, are subject to this phenomenon rendering more challenging the processing and the interpretation of SAR images. Each pixel's value corresponds to the coherent combination of $N$ elementary scatterers within the resolution cell. The resulting signal $s$ within a pixel can then be expressed in a complex form as follows:

$$s = \sum_{n=1}^{N} a_n e^{j\phi_n} = \alpha e^{j\Phi} \tag{1.14}$$

$a_n$ corresponds to the elementary amplitude of objects present within the resolution cell, and $\phi_n$ their phases. The resulting complex measurable information of the pixel is an amplitude $\alpha$ and a phase $\Phi$. The consequence of coherent combinations of scatterers of different amplitudes and phases leads to a random behavior of both amplitude $\alpha$ and phase $\Phi$ of the pixel values. The use of statistics is then required to describe the pixels' behavior by their probability density function.

### 1.4.1 Intensity, amplitude and phase distributions of SAR images

The statistical distributions presented in this section for SAR pixel values from equation 1.14 are considered true under the following conditions recalled in [29] which are:

1. the number of scatterers is large, and the medium in the resolution cell is homogeneous;
2. the range distance is much larger than the radar wavelength;
3. the surface is much rougher compared to the scale of the wavelength.

The condition (2) is, in practice, always satisfied with SAR systems. In contrast, the conditions (1) and (3) are not always satisfied considering, on the one hand, the diversity of configurations, sizes, electromagnetic properties, and shapes of scatterers within the observed scene and on the other hand, the SAR parameters such as operating frequency, polarisation, and spatial resolution.

Considering these assumptions and invoking the Central Limit theorem, the coherent sum of the real and imaginary parts of the monitored signal for each resolution cell (pixel) follows a zero-mean Gaussian complex distribution[2]. The following statistical considerations on the amplitudes, intensities, and phases of SAR monitored signals result from this Gaussian assumption.

**The amplitude** In general, we represent SAR images by their intensity denoted $\sigma$ that are related to the amplitude of the SAR signal as follows:

$$\sigma = |s|^2 = \alpha^2 \tag{1.15}$$

An incoherent mean of amplitudes $\alpha$ or intensities $\sigma$ can be performed spatially or temporally in order to decrease the effect of the speckle noise. By denoting $E[\sigma] = \mu_\sigma$ and $E[\alpha] = \mu_\alpha$ respectively the esperance of $\sigma$ and $\alpha$, it is usually admitted that the amplitude of the speckle without texture in SAR images follows a Rayleigh-Nagakami law $\mathcal{RN}[\mu_\alpha, L](\alpha)$ [43]:

$$\mathcal{RN}[\mu_\alpha, L](\alpha) = \frac{2\sqrt{L}}{\mu_\alpha \Gamma(L)} \left( \frac{\sqrt{L}\alpha}{\mu_\alpha} \right)^{2L-1} e^{-\left(\frac{\sqrt{L}}{\mu_\alpha}\alpha\right)^2} \tag{1.16}$$

with L the number of looks (samples taken into account to calculate the incoherent mean) and $\Gamma$ the Gamma distribution. If L=1 ( we call it Single Look Complex: SLC), the distribution of amplitude becomes a Rayleigh law $\mathcal{R}$ [44, 43]:

$$\mathcal{R}[\mu_\alpha](\alpha) = \frac{2\alpha}{\mu_\alpha^2} e^{-\left(\frac{\alpha}{\mu_\alpha}\right)^2} \tag{1.17}$$

**The intensity** For the intensity of SAR images, the texture-free speckle noise can be expressed with a generalized Gamma distribution $\mathcal{G}$ [43]:

$$\mathcal{G}[\mu_\sigma, L](\sigma) = \frac{L}{\mu_\sigma \Gamma(L)} \left( \frac{L\sigma}{\mu_\sigma} \right)^{L-1} e^{-\frac{L\sigma}{\mu_\sigma}} \tag{1.18}$$

Following the same principle, when L=1, the distribution of L looked intensity images becomes an exponential distribution $\mathcal{E}$:

$$\mathcal{E}[\mu_\sigma](\sigma) = \frac{1}{\mu_\sigma} e^{-\left(\frac{\sigma}{\mu_\sigma}\right)} \tag{1.19}$$

[2]the real and imaginary parts are two zero-mean independently and identically distributed Gaussian distributions

**The phase** Regarding the phase distribution, the derivation from the Gaussian assumption of the SAR signals results in a uniform distribution $\Pi$ of support $[-\pi, \pi]$:

$$\Pi(\Phi) = \frac{1}{2\pi} \text{ with } \Phi \in [-\pi, \pi] \tag{1.20}$$

The phase distribution of multilooked SAR images is not studied because the multilook is an incoherent process where each sampled phase does not intervene. Besides, the distribution of the phase of SAR signals under the precedent assumption shows that the phase cannot be interpreted with only one image. This result is one characteristic of SAR images. For smaller resolution systems, the assumptions (1) and (3) may fail when heterogeneous media occurred within the resolution cell and their surroundings. A parameter of texture can be taken into account, and the families of distribution to represent the pixels values are then extended to non-Gaussian distributions such as K-distribution, log-normal distribution, or, for example, Weibull distributions. As presented in [43], the consequence of non-Gaussian distribution assumptions implies using distributions with at least three parameters. As a result, the estimation of parameters to describe SAR images' pixel values becomes more challenging.

### 1.4.2 Polarimetric case

In the case of a polarimetric acquisition, we wrote the measurement vector in lexicographic basis $\mathbf{x} = [s^{HH} \quad s^{HV} \quad s^{VH} \quad s^{VV}]^T$. In that case, the signal $\mathbf{x}$ is said to follow a zero mean multivariate complex Gaussian distribution with $p \leq 4$ dimension $\mathcal{CN}[0, \mathbf{C}]$ with $\mathbf{C}$ its covariance matrix. Its probability density function is expressed as:

$$\mathcal{CN}[0, \mathbf{C}](\mathbf{x}) = \frac{1}{\pi^p |\mathbf{C}|} e^{-\mathbf{x^H C^{-1} x}} = \frac{1}{\pi^p |\mathbf{C}|} e^{-tr[\mathbf{C^{-1} x x^H}]} \tag{1.21}$$

Since the measurement vector in Pauli basis $\mathbf{y}$ is a linear combination of the element of $\mathbf{x}$, the same statistical properties stand for $\mathbf{T}$.

For multilooked polarimetric SAR signals, we denote the covariance matrix by $\mathbf{W} = L\mathbf{C}$, with $L$ the number of looks. The $p \times p$ matrix $\mathbf{W}$ is Hermitian, positive semi-definite; it follows a complex Wishart distribution $\mathcal{W}(p, L, C)$ [45]:

$$\mathcal{W}[p, L, \mathbf{C}](\mathbf{W}) = \frac{1}{\Gamma_p(L) |\mathbf{C}|^L} |\mathbf{W}|^{L-p} e^{-tr[\mathbf{C^{-1} W}]} \tag{1.22}$$

where $\Gamma_p(L) = \pi^{\frac{L(L-1)}{2}} \prod_{k=1}^{p} \Gamma(L - k + 1)$.

The remarks done for monopolarized signals stand regarding the validity of the Gaussian model

in coarse resolution polarimetric SAR images. Several works tackled this question [11, 46] and investigated possible satistical representations of polarimetric SAR images by enlarging the classical case of Gaussian assumption. For representing statistical heterogeneity, the texture of the speckle is usually represented as an independent multiplicative random variable, and the monitored polarimetric signal is modeled as $\mathbf{x}_{tex}$ [47]:

$$\mathbf{x}_{tex} = \sqrt{\tau}\mathbf{x} \tag{1.23}$$

$\tau$ represents a positive random variable for the texture and $\mathbf{x}$ is a usual Gaussian multivariate complex vector. Then, several assumptions can be made on the statistical distribution that follows the texture parameter $\tau$ leading to different distributions to represent the PolSAR data, that may vary depending on the applications (complex multivariate K-distribution, complex t-distribution, Generalized Gaussian distribution, or deterministic compound-Gaussian model) [43, 47, 11]. However, the choice of more complex distributions brings as well the problem of additional parameters determination that sometimes requires complex optimization problems.

**Overview of the chapter**: This chapter aimed to present some basic knowledge and understanding of SAR images required for our study. The diversity in terms of sensors and applications has been introduced, and the main advantages and drawbacks of SAR compared to optical imaging systems have been briefly discussed. The acquisition parameters have been presented to understand and analyze SAR images. Finally, the statistical representation of SAR images has been introduced for monopolarisation and polarimetric acquisitions. As presented in the chapter, the exploitation of SAR images represents a challenging problem that relies on both physical and statistical modelization of the observed environment.

# Chapter 2

# Preparation and presentation of the dataset used for the thesis

**Objectives**: This chapter introduces datasets used on several occasions during the thesis for simple illustration or SAR time-series analysis. To do so, we will present the general preprocessing steps necessary to consider the use of several SAR images. In a second time, these will be presented with their specificities.

The studies of SAR time-series imply that the images have to be preprocessed to exploit their values consistently. In some cases, the images are ready to use and in the form of coregistered products, as we will see from the UAVSAR (Uninhabited Aerial Vehicle Synthetic Aperture Radar) dataset analyzed in this study. On the contrary, for continuous monitoring SAR systems such as Sentinel 1, the data are available singularly with a given level of preprocessing. Different softwares have been developed to guide SAR images users for the preprocessing of the data. We will first present the main ideas briefly behind a preprocessing framework for SAR time-series exploitation. In a second time, datasets will be presented above Singapore from Sentinel 1 and San Francisco for UAVSAR.

## 2.1 Preprocessing steps for a stack of SAR images

We introduce the preliminary steps to be considered when analyzing and performing operations on a stack of SAR images. Some processes must be performed even when using only one SAR image. However, we aim to present a general preprocessing workflow when dealing with a stack of SAR images for which the content of the blocks will mainly depend on the application. SAR images

are generally presented as «products» with a given pre-processing level that may vary from a SAR sensor to another. It is not the purpose of giving a detailed description of all possible SAR formats and products available but presenting the main ideas that enable the constructing an exploitable stack of SAR images. Whatever the SAR sensor, the initial product from which the others will derive is called SLC (Single Look Complex), the pixels values are represented in the geometry of the radar (left column of images in Figure 2.1).

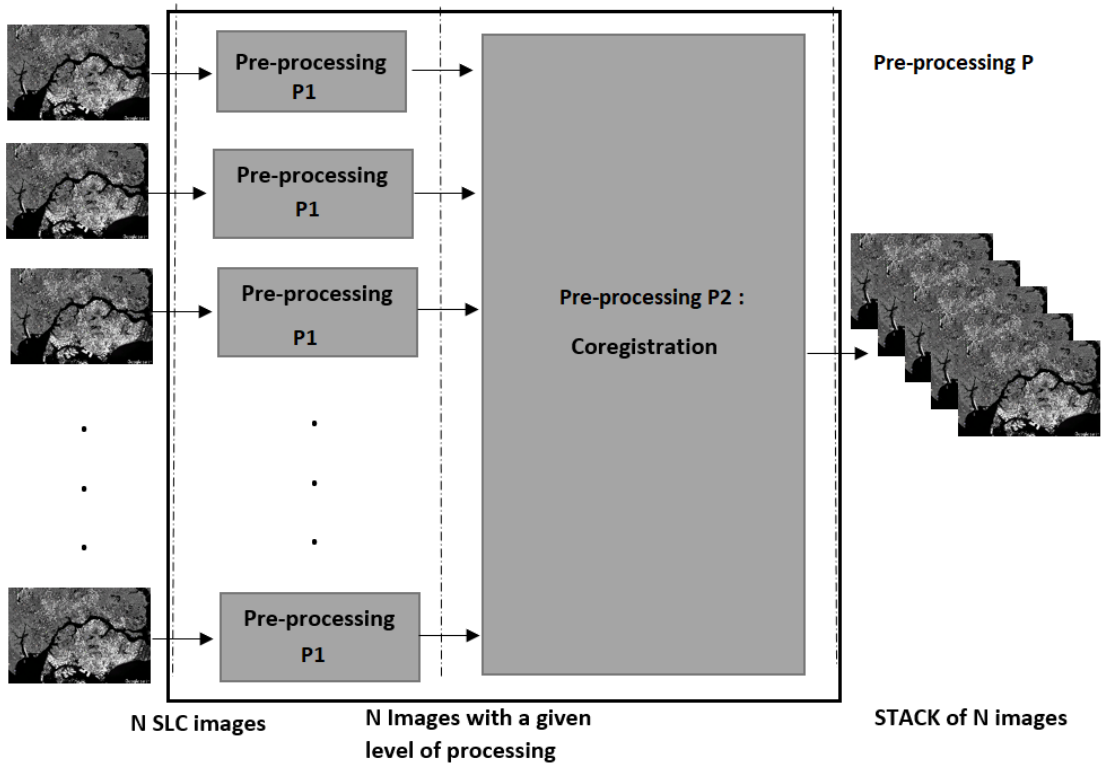


Figure 2.1: General workflow for the processing of $N$ SAR images to generate an exploitable stack.

"Preprocessing" is a generic term defining prior actions performed to the data; therefore, we specify in the Figure 2.1 a preprocessing P1 that can be performed individually per images and a preprocessing P2 that needs all the images. These preprocessing steps can be performed with the platforms SNAP (Sentinel Application Software) or PolSARPro that provide essential functions also adapted for specific sensors [48, 49]. When long SAR time-series have to be pre-processed, python API such as snappy[1] or pyroSAR[2] enables to interact easily with SNAP features and functions to process data automatically [3].

We can define two main parts of the workflow:

1. A preprocessing block P1 that can be performed independently for each image. Then two

[1] `https://senbox.atlassian.net/wiki/spaces/SNAP/pages/8847381/Developer+Guide`
[2] `https://pypi.org/project/pyroSAR/`
[3] A simple and complete tutorial to approach the SNAP Graph Processing Tool (gpt) that applies operations automatically on a stack of images from a terminal is available in the RUS Copernicus tutorial N°10

possibilities are met:

(a) Amplitude only: in that case, the usual procedure is to convert the image from the radar geometry to a ground geometry (usually called Ground Range Detected (GRD) product: projection to ground range using an Earth ellipsoid model and multilooking to obtain square pixels).

(b) The phase is required[4]: it is recommended to keep the data as raw as possible (calibration and orbit file for geolocalisation may be sufficient); multilooking can be performed for polarimetric processing but is not preferred for interferometry and permanent scatterer analysis since it implies resolution loss [50]).

These steps aim to calibrate the data radiometrically and perhaps use a precise orbit file to improve geo-localization of the images [5]. This step converts the input data into measurable information that depends on the desired application.

2. A preprocessing block P2 that will superpose (or align) the images of the time-series. The goal is then that for each image of the stack, the range and azimuth pixels represent the same geographic point so that a comparison between images is possible. It is a critical step in the process that can impact the results for posterior operations. This step can be done with a coarse coregistration based on each image's geographic coordinates and a fine coregistration based on the correlation between strong scatterers. We can then estimate a shift in pixels in range or azimuth and correct it. Other methods based on 2D-FFT of the image enable us to perform sub-pixel coregistration by estimated the shift between the two images in the frequency domain [51]. In general, when the resolution of the SAR images is high, it is becoming more challenging to obtain a satisfactory coregistration.

The framework that we presented consists of two main processing steps, one that can involve the images independently, and the second one that performs the coregistration between each of the images. For the rest of the thesis, we will introduce another framework that will include the steps we already presented. Therefore, these two pre-processing blocks will be defined as a general pre-processing named $P$.

[4] as for interferometry or polarimetric processing

[5] This step also includes possible burst processing if the images have particular acquisition modes such as Sentinel 1

## 2.2 Datasets exploited during the thesis

We present here some datasets exploited during the thesis that will be used in different chapters for illustrations or SAR time-series study. Other datasets may be used in the thesis for specific applications; their presentation and introduction will be done before their exploitation, in dedicated chapters.

### 2.2.1 Sentinel 1 (GRD) dataset above Singapore

Sentinel 1 is a constellation of two C-band satellites (Sentinel 1A and Sentinel 1B) developed by the European Space Agency and funded by the European Commission.

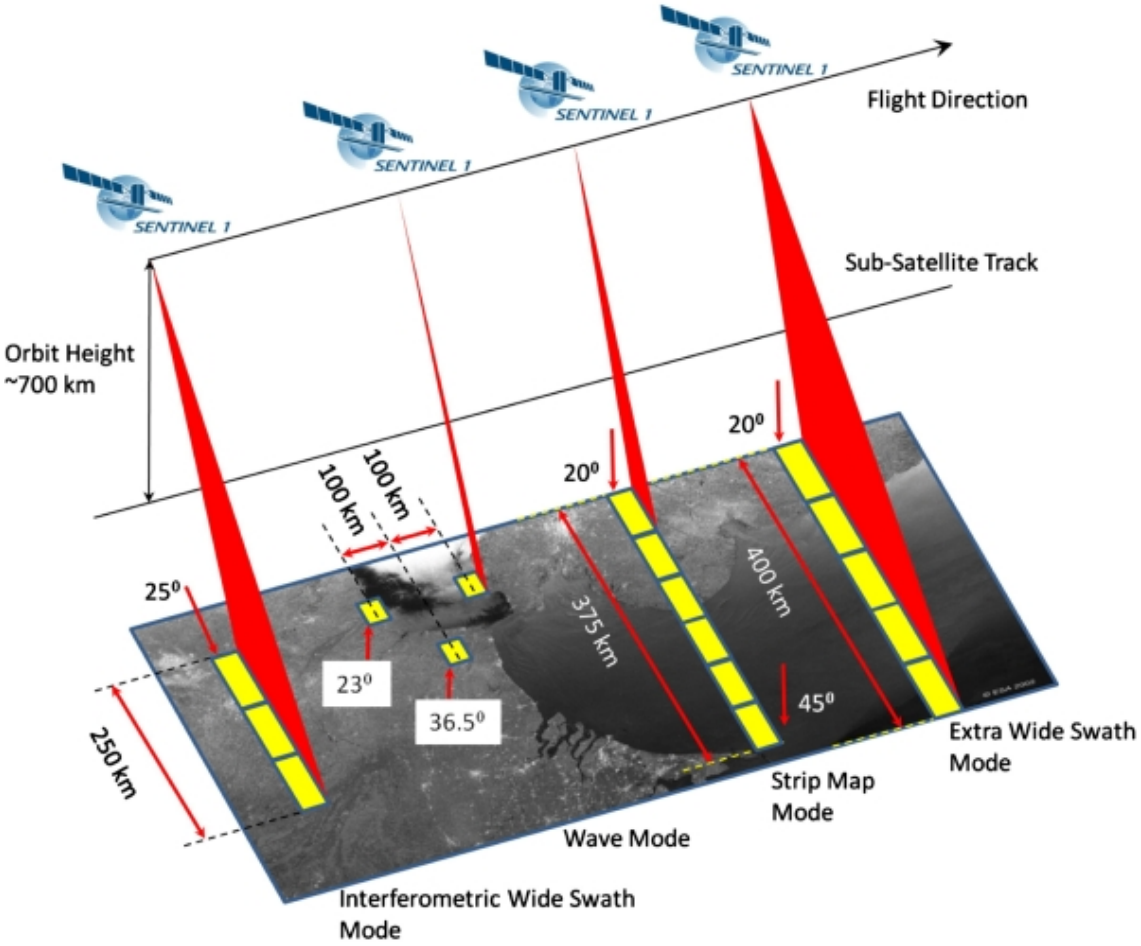


Figure 2.2: Sentinel Acquisition modes (from left to right): IW (Interferometric Wide Swath Mode), Wave Mode, Strip Map Mode and Extra Wide Swath Mode from [9].

It is for now, and since 2014, the only constellation of SAR satellites that guarantee continuously free data. This constellation of satellites enables us to obtain a 12 days revisit time or less if satellites and orbits are combined. Several acquisition modes can be used, as presented in Figure

2.2. Interferometric Wide Swath Mode (IW) is the mode of acquisition that is the most present within the Copernicus Access Hub data [52]. More information about the revisit time and the available acquisition mode depending on Earth's position is shown in Appendix A.

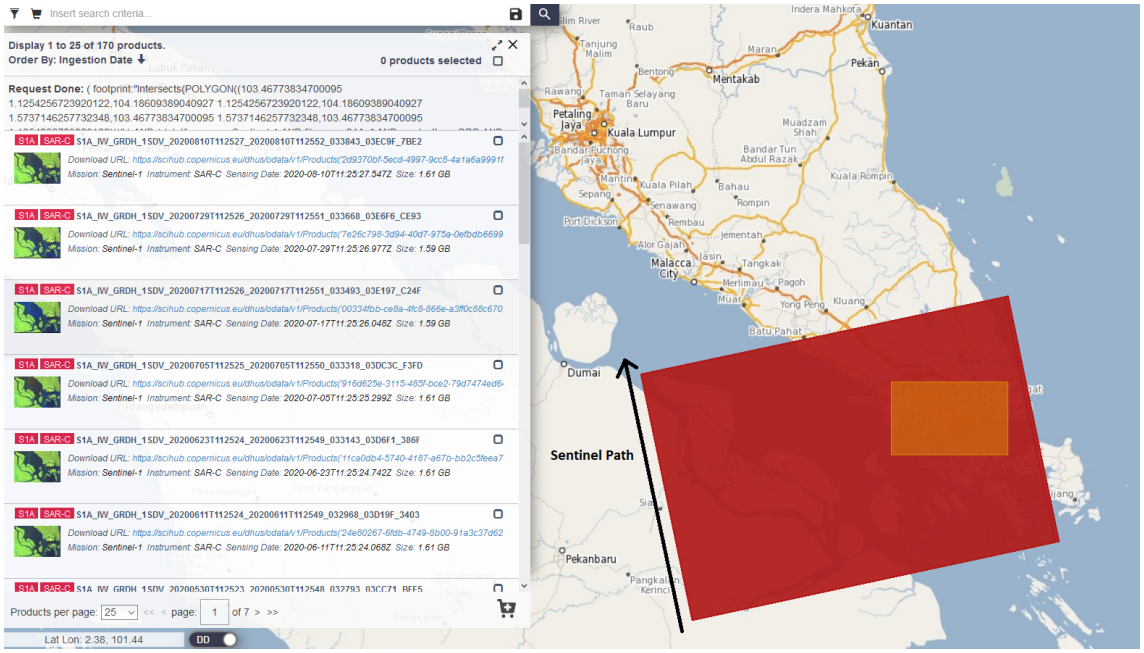


(a) Footprint of Sentinel 1A acquisition dataset above Singapore: relative orbit 171 (Ascending).

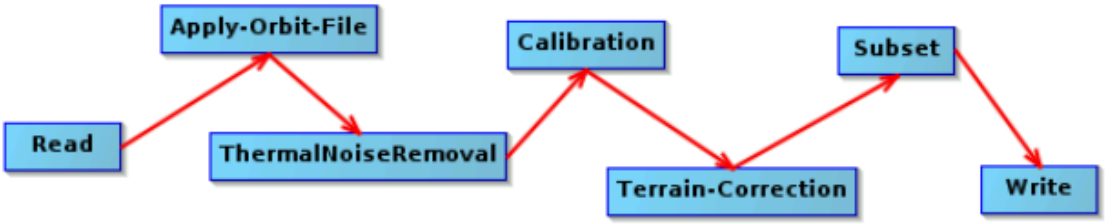


(b) Batch used to process each image of the stack in ESA SNAP (Sentinel Application Software).

Figure 2.3: Sentinel 1 GRD dataset presentation for the study of maritime surveillance in the region of Singapore.

The characteristics of the products used for our study are presented in the table 2.1. The footprint of the images monitored by the sensor is shown in Figure 2.3a. The orbit being ascending and antennas pointing to the right, we represented the satellite path with a black arrow in the Figure 2.3a. In that case, the data will be investigated in amplitude only, so we downloaded the GRD products, and we applied the associated pre-processing P1 graph, presented in Figure 2.3b.

We briefly define the purpose of each block between **Read** and **Write**:

- Apply orbit File: allow to get precise orbit information to improve geo-localization of the image;

- Thermal Noise Removal: suppress the thermal noise using a noise look-up table that depends on the acquisition;
- Calibration: convert the digital pixel values into radiometric information using as well a look-up table; calculate $\sigma_0$ for each pixel;
- Terrain Correction: correct the distortions introduced by the topography, as presented in Chapter 1 using a DEM (Digital Elevation Model). The image can be superposed on a map, as provided by Google Earth, for instance;
- Subset: perform a subset to obtain the area of interest.

Afterward, the images are coregistered between each other using the function «Coregistration» from SNAP software.

Table 2.1: Sentinel 1 data acquisition characteristics used for the study above Singapore

**Technical Characteristics of the Sentinel Images**

| | |
|---|---|
| **Acquisition mode** | Interferometric Wide (IW) swath |
| **Processing level** | Level-1 Ground Range Detected |
| **Polarisation** | VV+VH |
| **Pixel spacing** | 10×10 m |
| **Resolution range and azimuth** | 20×20 m |
| **Swath width** | 250 km |
| **Frequency band** | C-Band |
| **Relative orbit number** | 171 |
| **Near incidence angle** | 30° |
| **Far incidence angle** | 46° |
| **Acquisition dates** | From 3 Feb.2017 to 26 Dec. 2019 (83 images) |
| **Location** | `http://maps.google.com/maps?q=1.294152,103.733984` |

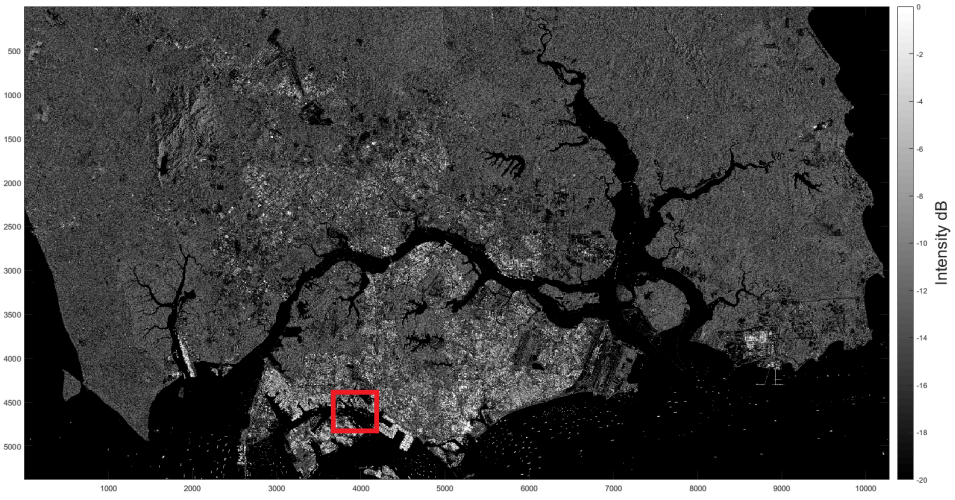


Figure 2.4: Sentinel 1 GRD VV product above Singapore acquired on the 11th of February 2018.

This dataset will be mainly exploited for maritime surveillance applications since Singapore has one of the world's biggest port (by cargo volume).

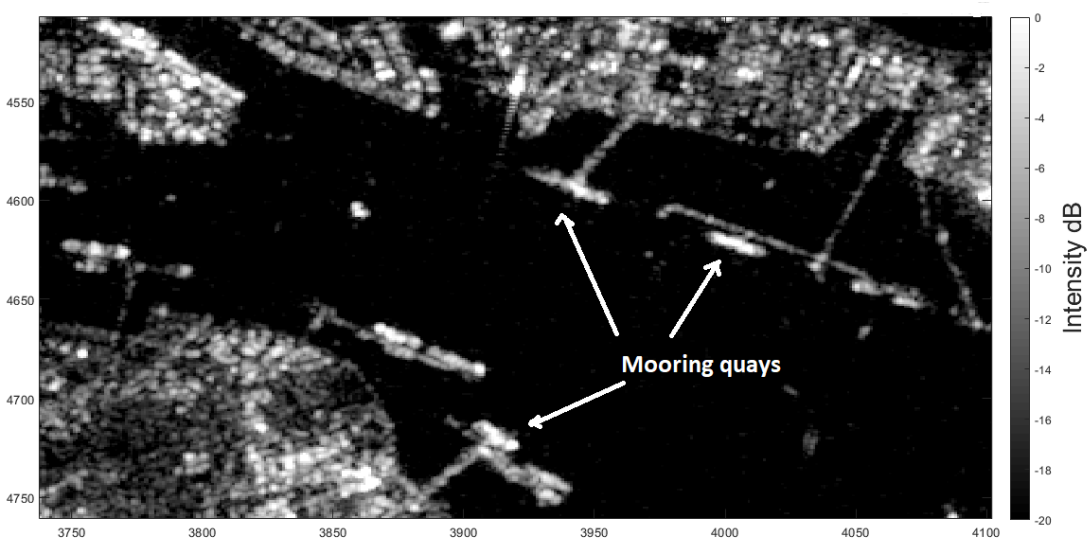


(a) Radiometric image acquired on the 11th February 2018 at VV polarization.


(b) Optical image acquired on the 10th February 2018.

Figure 2.5: Radiometric and optical images of the studied area: (**a**) Radiometric image acquired on the 11th February 2018 at VV polarization, (**b**) Optical image collected on the 10th February 2018.

This area provides a challenging configuration for the specific application of ship detection inside harbors. In Figure 2.4 is presented a radiometric image of the region of Singapore. The study area is framed in red and consists of an industrial harbor between central Singapore island and Jurong island, as presented in the optical image acquired on the 10th February 2018 by LANDSAT

in Figure 2.5. A radiometric image, monitored one day after the optical one, is represented for the polarisation VV. In industrial harbors, the configuration evolves fast regarding the number and position of the ships. As a consequence, the comparison with optical data cannot be used for validation. Therefore, we propose to use the AIS signals (Automatic Identification Systems) of the ships to obtain real-time information. This aspect will be discussed in chapter 7, dedicated to maritime surveillance.

### 2.2.2 UAVSAR (Uninhabited Aerial Vehicle Synthetic Aperture Radar)

The UAVSAR instrument [53] has been developed by the NASA JPL (Jet Propulsion Laboratory) to acquire remotely airborne repeat-track SAR data. This SAR platform is an airborne sensor, whereas Sentinel 1 is a spaceborne sensor. It implies several consequences on the image that can be taken into consideration, depending on the situation. Indeed, with spaceborne sensors, the incidence angle variation depending on the range is less broad than in the airborne sensor's case due to the distance between the plane and the illuminated area.

Figure 2.6: UAVSAR Airborne sensor developed by NASA JPL (Jet Propulsion Laboratory).

The side-looking UAVSAR instrument's main objective is to accurately map crustal deformations associated with natural hazards, such as volcanoes and earthquakes. This sensor operates at P-, L- and K-bands and can collect the radar signal in four polarisations (HH, HV, VH, and VV). Several calibrated and coregistered stacks of SLC images are available in open access from the data search website dedicated to UAVSAR [54].

#### San Francisco region

The characteristics of the SAR images collected above the San Francisco region can be found in table 2.2. The footprint of the monitored area is presented in Figure 2.7. This stack of SLC images can be processed directly for time-series analysis since it is calibrated and coregistered.

Table 2.2: UAVSAR data acquisition characteristics used for the study.

**Technical characteristics of the UAVSAR images above San Francisco region**

| | |
|---|---|
| **Acquisition Mode** | PolSAR |
| **Processing level** | Single Look Complex (SLC) |
| **Polarisation** | (HH+HV+VH+VV) |
| **Resolution** | 1.8x0.8m |
| **Frequency band** | L-Band |
| **Stack Name** | SDelta_23518_01 |
| **Acquisition dates** | July 2009 to November 2017 (68 Images) |
| **Location** | `https://www.google.com/maps/search/?api=1&query=38.052500001,-121.83250000` |

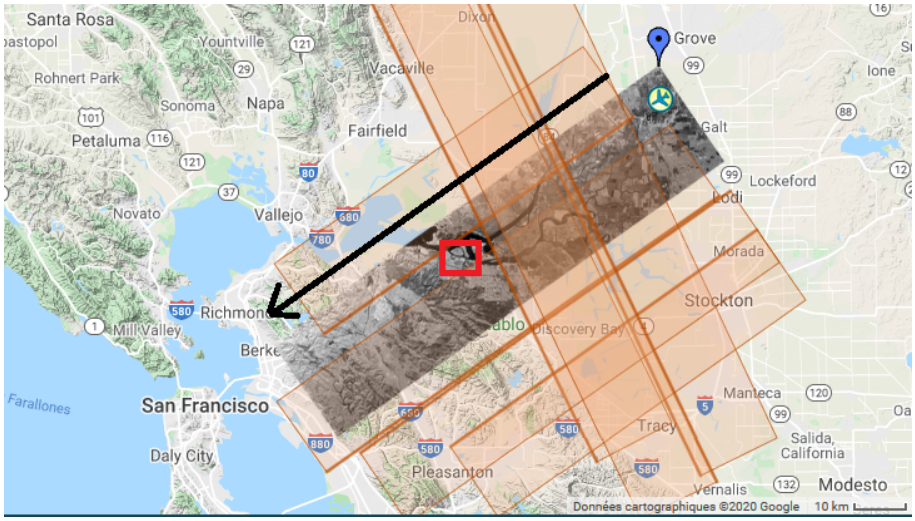


Figure 2.7: The footprint of the UAVSAR sensor above the San Francisco region: product SDelta_23518. The area squared in red is the region of interest in Pittsburg's industrial area (California, USA).

The sensor's path is represented by a black arrow in Figure 2.7, and the region of interest used for the study of SAR time-series is framed in red. This dataset is interesting because it contains 68 SAR images in full polarisation. We chose an area of interest with a small industrial harbor; we show a radiometric SAR image in figure 2.8a acquired the 18th July 2009, and an optical image acquired the 23rd July 2009 from LANDSAT optical sensor in Figure 2.8b. This harbor is part of Pittsburg's industrial area (California, USA), which is in the region of the Sacramento-San Joaquin River Delta (San Francisco Bay). This dataset will be exploited for SAR time-series with interest in harbor monitoring.

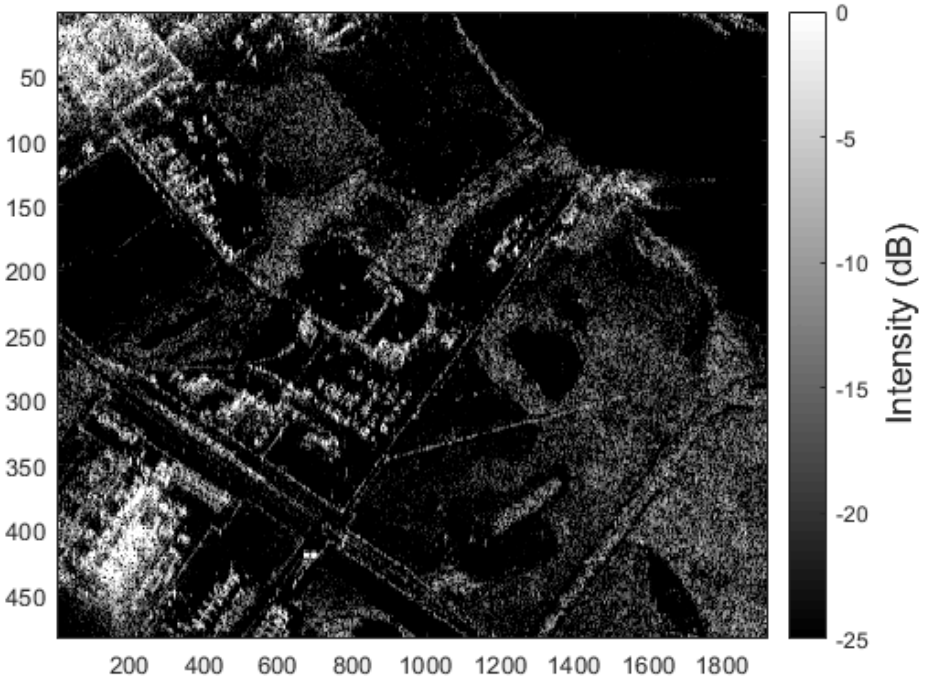


(a) Radiometric image acquired on the 18th of July 2009 at HH polarization (UAVSAR).


(b) Optical image acquired on the 23rd of July 2009 (LANDSAT).

Figure 2.8: Radiometric (**a**) and optical (**b**) images of the studied area (Pittsburg, California, USA).

## 2.3 Discussion

The preprocessing of SAR images is a crucial step when the goal is to perform time-series analysis. Knowing the preprocessing operations performed on SAR time-series is essential because it improves our understanding and interpretation of the time-series' content. The data sets that we will analyze in this manuscript are then constituted of a first set of 83 C-band SAR images above the region of Singapore acquired by Sentinel 1 (VV and VH) and a set of 68 L-band full polarimetric SAR images acquired by UAVSAR above the city of Pittsburgh in the region of the Sacramento-San Joaquin River Delta. As expressed before, the strength of Sentinel 1 relies on the capacity to continuously monitor the Earth, making possible quasi fully automatic framework. Thanks to this satellite constellation, the effort made to develop different platforms (SNAP, PolSARpro), and users' contributions via forums or python programs, it is possible to obtain free information on most of the globe's surface with a good revisit time. While the resolution of Sentinel 1 is not suitable for some applications (e.g., detection of vehicles in cities), we will see that it gives interesting results when time-series are exploited for ship detection in harbor environments.

**Summary** :

This chapter introduced data sets that will be used on several occasions during the thesis for simple illustration or more in-depth SAR time-series analysis. The preprocessing of data is mandatory to ensure accurate exploitation and avoid misinterpretations due to wrong calibration or coregistration. A general but not an exhaustive framework of preprocessing has been introduced, as it is highly dependent on the sensor's acquisition modes and the domain of applications.

# Chapter 3

# Introduction to change detection in SAR time-series: applications to target detection

**Objectives** :

This chapter presents an overview of change detection techniques applied to SAR time-series. Depending on the application, the available data, and the purposes, different strategies can be carried out. The classification of change detection methods can be done through different criteria: applications, types of data, or algorithm nature. We propose to classify the current methods in two fundamental methodologies. The first one is driven by bi-date (or bi-temporal) similarity testing. It represents a classical way to carry out change detection in SAR time-series. A second approach considers the homogeneity of the whole time-series to look eventually for ruptures. In this chapter, The first part consists of presenting the key aspects when designing a change detection framework applied to SAR time-series. The second part investigates and describes different change detection approaches according to the two methodologies mentioned above. Finally, ephemeral target detection is introduced in the context of SAR time-series, and the main challenges are presented.

Remote sensing became more and more attractive for the scientific community and governmental institutions in different domains. Several SAR times series are currently available, and even

more will be in open access in the future [55, 56, 20]. Therefore, it is essential to develop methodologies and concepts to deal with this critical amount of data and extract the information in our interest. For a few years, the access to SAR open data acquired periodically has been made easier. SAR time-series exploitation has been thoroughly studied, and statistical tests have been derived in different forms to obtain the information of change within the time-series and the change points. Figure 3.1 presents a historical tree of change detection methods applied to remote sensing data. As we can see, three important families are shown: Classification, Transformation, and Algebra. According to this classification tree, the change detection methods we will investigate and present in this manuscript are mostly part of the Algebra family.

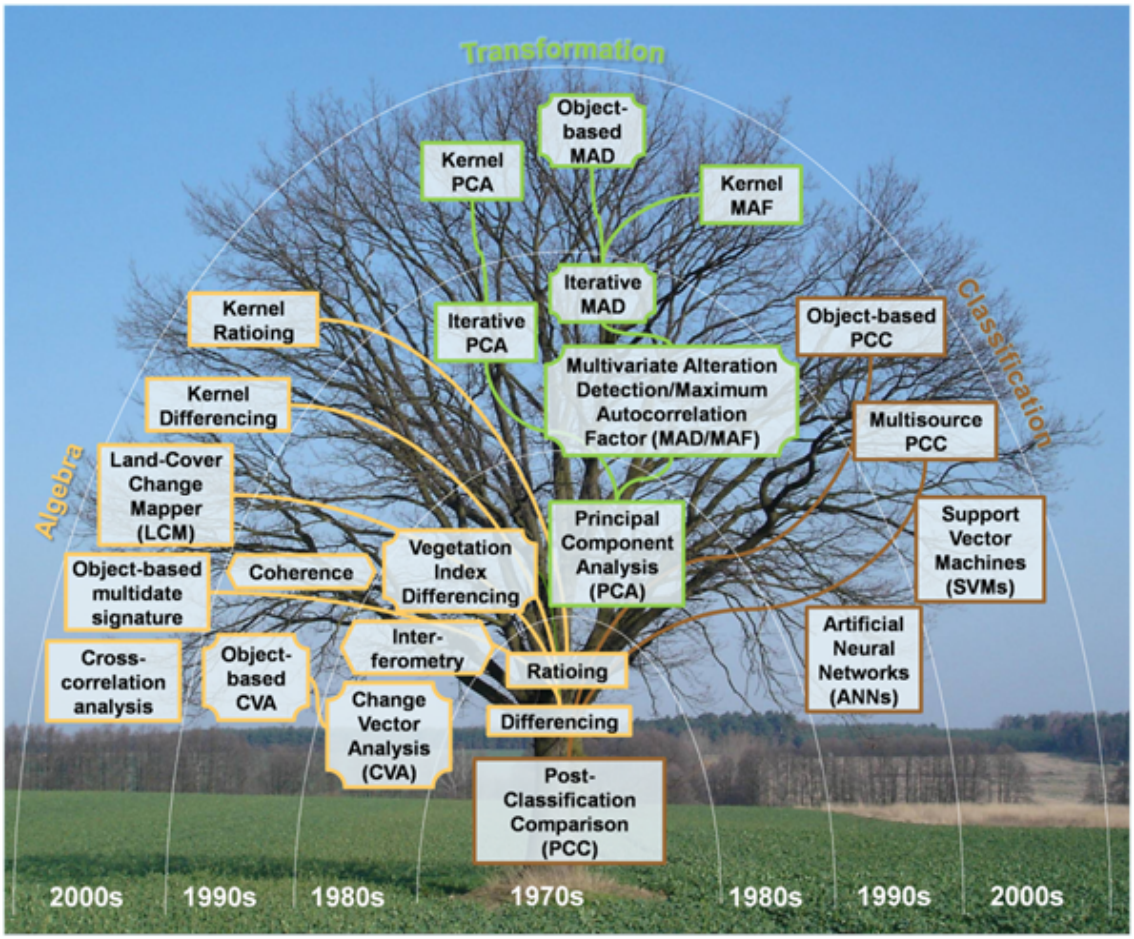


Figure 3.1: Historical tree of change detection methods for remote sensing.

## 3.1 Design a change detection framework in the context of SAR time-series

Without considering the remote sensing technology, the purpose of change detection is to quantify and decide whether the attributes (measurable information) of a particular area have changed between two or more acquisitions. One variable of interest in SAR images is the backscattering signal used in its complex or magnitude form, monovariate (one polarisation), or multivariate (polarimetric acquisitions or multi-scale coming from subspectral exploitation). Change detection strategies are numerous, and extensive literature is available in the Earth observation community. Since the diversity of changes is broad, it is essential to design a framework that will maximize the opportunity to observe the changes that characterize the application of interest. Designing change detection algorithms requires to define the problem as precisely as possible to use prior knowledge and improve the outcome of the detection. These different aspects can drive change detection strategies and frameworks. **Firstly the application domains will fix constraints on the choice of data** (polarimetric data, spatial resolution, revisit time). The type of data will then impact detection strategies and require specific processes or assumptions about the temporal behavior of the objects seen under a given operating frequency. This temporal behavior will impact the underlying hypotheses and strategies for change detection. **Secondly, the way to represent changes will impact the type of information we will have to measure**: binary change maps, multiclass change maps, continuous change maps, maximum change dates, or classification of change types. **Thirdly, we have to consider the computation time and the preprocessing complexity** associated with SAR time-series exploitation. For instance, the accuracy required for SAR data's coregistration may be critical or not depending on the type of changes.

### 3.1.1 A general framework of change detection for SAR time-series

In this part, we present in figure 3.2 a general framework of change detection for SAR time-series and briefly introduce the specificity and the role of each block.

**1) Data Collection**:

This step represents data collection considered in a problem of change detection, taking into account the possible geometries of acquisition (satellite orbit, incidence angle), temporal resolutions, type of sensors (multi-sensors, or only one sensor). In general, the input data consists of a set of images acquired at a different time (with possible diversity for each image, such as polarimetric, angle, or frequency of acquisitions).

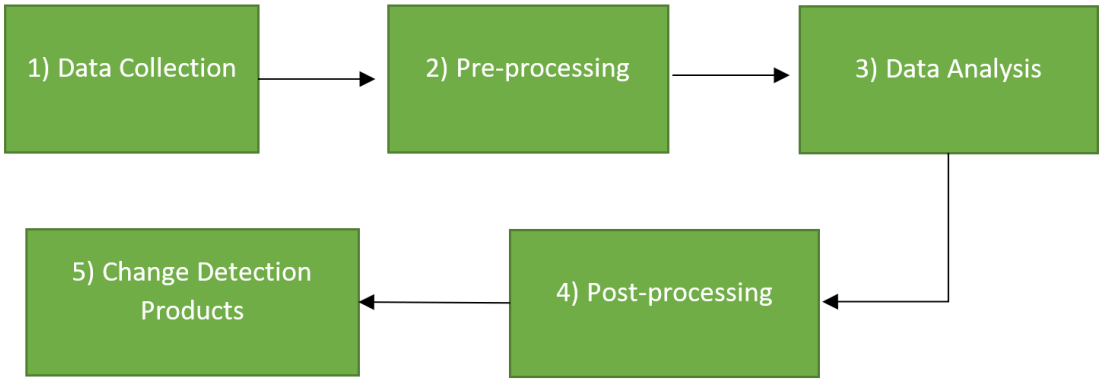


Figure 3.2: A general framework of change detection for SAR time-series, adapted from [10] and [11]

**2) Preprocessing**:

The preprocessing step is essential and significantly influences the quality of change detection results. It includes the preprocessing P1 and P2 introduced in chapter 2 to obtain a stack of images for which the measurable information is comparable between images. Addionnaly, if the change detection considers changes in features space, it can also be gathered in a preprocessing step. For instance, if a prior polarimetric classification is performed or sub-bands of the images in spatial Fourier space are exploited, the change detection algorithm will be carried out on those features and not anymore on the backscattering signal itself.

**3) Data analysis**:

Data analysis or data comparison is the heart of the change detection framework. The measurable quantities of the preprocessed input data are computed into a measure of similarity that aims to represent whether it is likely that a change occurred. Different approaches and structures of algorithms will be described and developed in the following sections of this chapter.

**4) Postprocessing**:

Postprocessing includes thresholding or classification of changes. In general cases, the similarity measure will be thresholded to obtain a change map or a set of change maps that can be combined to generate change detection products.

**5) Change detection products**:

Change detection products represent the final visualization format of the change detection processes. The results can be presented differently depending on the application and the user purpose:

- Binary change map
- Frequency of changes

- Most significant change
- First change or last change
- Classification in the type of changes
- Raw output (no thresholding)

### 3.1.2 SAR time-series analysis: different types of changes

The observation of Earth from space leads to the study of complex temporal phenomenons. It is then essential to define the information of interest to optimize the framework of change detection. We can divide the changes into natural changes and man-made changes. For these two categories, the following temporal features can be considered:

- **Periodic changes**: when a seasonal variation is observed (tidal effect, vegetation changes through seasons, rise and recede of water in river and lake, agricultural activity).
- **Ephemeral changes:** flooding, vehicles or ships appearance/disappearance.
- **Permanent change:** an event established in time, such as building construction. In this case, the temporal signal corresponds to a rising or falling edge.
- **Continuous change:** as for ice melting in polar regions or building construction.
- **Chaotic evolution**: as for crop fields sensitive to meteorological variation condition.

## 3.2 Change detection techniques overview

This section does not give an exhaustive presentation of all techniques, but we propose to present several SAR time-series change detection approaches that have inspired the present study. The first one is based on bi-temporal approaches. A sequential or exhaustive (all possible combinations) testing between bi-temporal combinations of the time-series is performed. In a second time, we present other strategies that aim to investigate the overall homogeneity of the time-series to decide either a change occurred or not. If the purpose is to date the ruptures, different strategies are carried out to extract them.

### 3.2.1 Bi-date approaches (Similarity)

The most natural change detection frameworks for remote sensing consider binary tests between image pairs sequentially or in an exhaustive way (all possible combinations). The terms bi-date or bi-temporal may be employed in the literature when considering such frameworks. Different measures of change (or similarity) can be employed. We will describe here the most significant and

relevant for our research in SAR imaging applications. Performing bi-date-based change detection implies using a spatial window to obtain local statistics for each pair's images. Therefore, the similarity is evaluated (generally complex value, amplitude, intensity, or covariance matrix) [1] between a pixel and its neighborhood at a date m and at a date k. A threshold is used to decide between one of these two hypotheses:

$$\begin{cases} H_0: & \text{No change between date m and date k} \\ H_1: & \text{A change occurred between date m and date k} \end{cases} \tag{3.1}$$

**Coherence as a measure of change**

Considering a complex measurements pixel $s_m$ at a date m and $s_k$ at a date k, it is possible to express their interferometric coherence by the following function:

$$\gamma_I = \frac{< s_m s_k^* >}{\sqrt{< s_m s_m^* >< s_k s_k^* >}} = \rho e^{j\Delta\phi} \tag{3.2}$$

"<>" denoting a spatial averaging operator of N spatial samples, $\rho$ is the interferometric coherence or more generally coherence and the interferometric phase $\Delta\phi = \Phi_m - \Phi_k$ with $\Phi_m$ and $\Phi_k$ the measured phases at dates m and k. The phase difference is exploited in SAR interferometry to highlight subtle changes that may have occurred, for instance, subsidence or earthquake monitoring [57]. The use of coherence may lead to misinterpretation because of the Clutter-to-Noise ratio (CNR)[2]:

$$\rho = \frac{CNR}{1 + CNR} \tag{3.3}$$

This expression shows that if the signal amplitude is low (signal amplitude near the NESZ), the expected coherence tends to 0 even though no significant change occurs. It is one of the main drawbacks of coherent change detection.

**Generalized Likelihood Ratio Test (GLRT) for covariance matrices equality**

The GLRT for covariance matrices equality has been introduced by [45], [58] and [59]. It is the most popular form of change detection based on whether the intensity $\sigma$ (that follows a Gamma law) of a monopolarised signal or the covariance matrix $\mathbf{C}$ (that follows a Wishart distribution) of a polarimetric signal. The GLRT is an LRT (Likelihood Ratio Test) that replaces the unknown parameters in the likelihood functions (for $H_0$ and $H_1$) by their maximum likelihood estimator

[1] It can also be classes from a decomposition; however, we will not consider this case in the manuscript

[2] Clutter is defined as a signal that does not correspond to a target nor pure noise. It will be discussed more in detail afterward

(MLE). When dealing with covariance matrices, the test $\gamma_G$ can be therefore expressed by denoting $\mathbf{C_m}$ and $\mathbf{C_k}$ of size p × p with p the number of polarisations, the sample covariance matrices for a given pixel at a date $m$ and date $k$ estimated using a spatial window containing $N$ elements:

$$\gamma_G = \frac{|\mathbf{C_m}|^N |\mathbf{C_k}|^N}{|\frac{1}{2}(\mathbf{C_m} + \mathbf{C_k})|^{2N}} \tag{3.4}$$

When $p = 1$, for the monopolarisation case, the test becomes:

$$\gamma_G = \frac{\bar{\sigma}_m^N \bar{\sigma}_k^N}{\left(\frac{1}{2}\left(\bar{\sigma}_m + \bar{\sigma}_k\right)\right)^{2N}} \tag{3.5}$$

where $\bar{\sigma}_k =< \sigma_k >$ and $\bar{\sigma}_m =< \sigma_m >$ are the intensity averaged over $N$ spatial pixels of a monopolarized acquisition respectively for a given pixel at date $m$ and date $k$. It is shown in [59] that the test 3.5 can be rewritten as the usual ratio test between averaged intensities of images. It has to be noted that the statistics underlying these tests in monopolarisation and polarimetric derives from a Gaussian assumption of the monitored signal's real and imaginary part.

#### Other similarity measures

Other similarity measures can be exploited for SAR images such as Kullback-Leiber (KL) distance [60] that is regarded as an information theory measure between the modeled distribution of the local data at two different dates. As discussed in section 3.1.1, the backscattering coefficient can be expressed through a wavelet transformation giving multi-scale information of the pixel that can be exploited as multivariate information. This strategy has been exploited in [61, 62, 11].
Finally, a pre-classification, such as H/A/$\alpha$, Van-Zyl, Yamaguchi, or any polarimetric existent classification, can be performed, and the change information will therefore rely on a change of class as in [63].

#### Time-series analyses with frameworks using bi-date approach

Bi-date frameworks have been considered in several studies to describe the behavior of changes in SAR time-series. In [64, 62], the CDM (Change Detection Matrix) has been introduced to represent the exhaustive bi-temporal behavior of the time-series for each spatial position. Similarity cross tests are performed and the outcome is gathered in the CDM containing all the information of changed and unchanged pixels. This method has interesting insight and enables to obtain some temporal patterns since it is scanning each combination of dates extensively. If we consider a similarity measure $\mathcal{D}(\vartheta m, \vartheta_k)$ between two measurables $\vartheta m$ and $\vartheta k$ at date $m$ and $k$. The binary outcome $b_{m \to k}$ of the test after thresholding is expressed for each spatial position in the Change

Detection Matrix as follows:

$$CDM = \begin{pmatrix} b_{1\to 2} & b_{1\to 3} & \cdots & b_{1\to D} \\ b_{1\to 3} & b_{2\to 3} & \cdots & b_{2\to D} \\ \vdots & \vdots & \ddots & \vdots \\ b_{1\to D} & b_{2\to D} & \cdots & b_{D-1\to D} \end{pmatrix}$$

Most of the bi-temporal frameworks can be derived from this CDM; for example, taking the CDM matrix's diagonal would give a sequential (chronological) bi-temporal test. It is classical in change detection to consider sequential frameworks. For instance, it has been exploited in [65] for oil spill detection and used more recently with only coherent change detection as a similarity measure to monitor building constructions in Iran [66]. Besides, the complete information of the CDM may be exploited, as in [64] using matrix clustering to derive temporal patterns such as periodic, step changes, or chaotic changes. However, the use of the Change Detection Matrix is computationally heavy as it requires calculating a $D \times D$ matrix for each spatial position for a temporal stack of $D$ images.

Another method [67, 68] recently developed initially for image denoising purpose and called RABASAR (RAtio-Based multitemporal SAR despeckling), is based on a temporal multi-looking of time-series; it is also used for CD applications in time-series from these denoised SAR images.

Bi-temporal strategies have been historically introduced when few temporal images where available. Since the launch of Sentinel 1 in 2014, access to long time-series became widespread. Extensive testing in bi-temporal frameworks becomes challenging to put into practice due to the high computational cost that it may generate. Alternatively, using only sequential consideration leads to different problems that we will introduce at the end of this chapter.

### 3.2.2 Overall temporal statistics (Homogeneity)

More recently, several approaches consider studying the overall behavior of time-series, without dating the change as a first goal. Therefore, we will first introduce some homogeneity measures that consider the whole time-series and not bi-temporal testings. In that case, the homogeneity test's binary outcome is expressed only temporally or taking into account a neighbouring window as done precedently for bi-date testings. A threshold is used to decide between one of these two hypotheses:

$$\begin{cases} H_0 : & \text{No Change in whole time-series} \\ H_1 : & \text{At least one change occurred} \end{cases} \tag{3.6}$$

Different strategies are carried out afterward to find the ruptures in the time-series, it can also involve some methods from bi-temporal schemes.

**GLRT for the equality of several covariance matrices (or Intensities)**

The term «Omnibus» in statistical analyses refers to an overall test that aims to decide if at least one of the population's estimated statistical parameters is different from the others. This test compares within the whole time-series intensities values in the case of monopolarisation data or covariances matrices in the case of polarimetric data. In particular, in [45, 69, 58] the binary outcome of such test provides the information of a change within the time-series without considering firstly when the change occurred. The GLRT test in Gaussian context $\gamma_{GM}$ for an overall test on the time-series can be expressed as follows for D covariance matrices $\mathbf{C_d}$ $(d = 1, .., D)$ and given N spatial samples pixels for the estimation of the covariance matrix:

$$\gamma_{GM} = \frac{\prod_{d=1}^{D} |\mathbf{C_d}|^N}{|\frac{1}{D}\sum_{d=1}^{D} \mathbf{C_d}|^{DN}} \tag{3.7}$$

In the case of monopolarisation data, the test become :

$$\gamma_{GM} = \frac{\prod_{d=1}^{D} \bar{\sigma}_d^N}{(\frac{1}{D}\sum_{d=1}^{D} \bar{\sigma}_d)^{DN}} \tag{3.8}$$

where $\bar{\sigma_d} =< \sigma_d >$ is the intensity averaged over N spatial pixels of a monopolarized acquisition at date d. We can notice that setting D=2 brings back the tests introduced before for a bi-temporal approach in section 3.2.1 for the polarimetric case and for the monopolarized case. For non-Gaussian assumptions, GLRT statistics have been derived in [11, 70].

**Temporal Variation coefficient**

The variation coefficient (CV), also known as relative standard deviation, is mathematically defined in probability theory and statistics by $std(\alpha)/\mu_\alpha$, where $std(\alpha)$ is the standard deviation of the variable $\alpha$ and $\mu_\alpha$ its mean value. It can be considered as a normalized measurement of the dispersion of a probability distribution. It has been introduced firstly for application in SAR imaging for spatial detection of abrupt changes in [71, 72]. The most general way to represent the variation coefficient derives from the first two statistical moments $m_1$ (mean) and $m_2$ (variance)

of any distribution :

$$CV = \frac{\sqrt{m_2 - m_1^2}}{m_1} \tag{3.9}$$

A thorough study can be found in [73] for temporal CV analysis and related statistical properties. As presented in chapter 1, it is commonly accepted that the amplitude of a speckle without texture follows a Rayleigh Nagakami distribution:

$$RN[\mu_\alpha, L](\alpha) = \frac{2\sqrt{L}}{\mu_\alpha \Gamma(L)} \left( \frac{\sqrt{L}\alpha}{\mu_\alpha} \right)^{2L-1} e^{-\left(\frac{\sqrt{L}}{\mu_\alpha}\alpha\right)^2} \tag{3.10}$$

where $\alpha$ is the amplitude, $\mu_\alpha = E[\alpha]$ is the esperance of $\alpha$, $\Gamma$ is the gamma function and $L$ is called looks number of the product. In this approach, the temporal statistics only is exploited, so no spatial neighborhood window is used. According to [73], the theoretical variation coefficient can be derived then as follows:

$$CV_{theo} = \sqrt{\frac{\Gamma(L)\Gamma(L+1)}{\Gamma(L+\frac{1}{2})^2} - 1} \tag{3.11}$$

This expression shows that the variation coefficient has the same value for all stable speckle zones, whatever the average amplitude of this speckle. It is also shown in [73, 43] that the standard deviation of the variation coefficient decreases in $\sqrt{D}$, D being the number of dates of the time-series. Interestingly, in [74], the variation coefficient is used as a preliminary test to select candidate permanent scatterers in a series of interferometric SAR images. Indeed, in the article, the theoretical link between the variation coefficient, the SNR, and the phase deviation is established[3]. The results of this study show that, when the SNR is sufficiently high, so when a deterministic scatterer with a high contribution is temporally stable, the phase deviation of the interferometric signal is equal to the variation coefficient itself [74]. In practice, a value inferior to 0.25 is chosen for the selection of permanent scatterers[4] (considering that for interferometry, the products used are SLC so L=1). For distributions that would model deterministic structures, whatever the value of this permanent scatterer, the variation coefficient's theoretical value decreases and tends to zero when the permanent scatterer's contributions tend to infinity (for a given number of looks). This variation coefficient has interesting properties and will be studied more deeply in chapters 4 and 5.

[3]For permanent scatterers, a Rice law is more appropriate to model the signal. Actually, the SNR can be used as a parameter of the Rice Law. For L=1, when the SNR is low, the distribution of the amplitude becomes simply a Rayleigh distribution (normal speckle), whereas, for high SNR (Permanent Scatterer), a Rice distribution seems to be a better model according to [74, 73]

[4]StaMPS (Stanford Method for Permanent Scatterers) uses the coefficient variation as prior permanent scatterers selection

**Time-series analyses with frameworks using overall temporal (or spatio-temporal) statistics**

In recent years, the bi-temporal approaches have been replaced gradually by overall statistics. Two possibilities are met with these approaches: first, the information that at least one change occurred within the time-series might be enough, and no interest is brought to the rupture date. Alternatively, some approaches will investigate when the ruptures occurred. In [75], the overall statistics in MIMOSA (Method for generalIzed Means Ordered Series Analysis) gives the information that a change occurred in the time-series. In that case, the position (range-azimuth) of the change is known, but when the rupture occurred remain unknown. In [76] REACTIV (Rapid and EAsy Change detection in radar TIme-series by Variation coefficient), the overall test is performed using the variation coefficient described in this section by displaying the date of the most significant change in the time-series (maximum of the amplitude if a change occurred). In [73], the variation coefficient is used to find profiles of changes such as Dirac form or step forms. Finally, in [58], step-change is investigated using GLRT time-series of SAR images. More recently, one change detection framework proposed by [77] is based first on the GLRT (omnibus test) on the covariance matrices estimated along the time-series (or Intensities) and second estimates change points by scanning the time-series sequentially using marginal tests.

Exploiting time-series' overall temporal statistics decreases the computational cost since we do not scan all the time-series' bi-temporal combinations exhaustively. If no change has been detected within the time-series, there is no need to look for a change point for this geographic position. However, currently, the frameworks seeking for change points consider "steps" changes or "Dirac" changes in the series so that sequential (chronological) tests are in general enough. From the literature, we can notice that the characterization of the type of changes seemed to have been successfully performed only using exhaustive bi-temporal frameworks.

### 3.2.3 Threshold determination

For each similarity or homogeneity measure presented before, one has to use a threshold to decide between one of the two hypotheses $H_0$ unchanged or $H_1$ changed. For some similarity measures presented before, a threshold can be directly related analytically to a given false alarm probability. It is the case for the GLRTs presented for a bi-temporal case or overall case where a threshold can be chosen according to a given significance level using an asymptotic expansion of the test distribution [45]). It is challenging to obtain a decision threshold automatically because it might

depend on the data collected and the type of changes. A global threshold can be applied to the whole image to choose between changed and unchanged areas using the Otsu method [78] or Kittler-Illingworth (KI) threshold [79].

### 3.2.4 Performance metrics for change detection

In the thesis, we will use a common approach for change detection performance evaluation. We consider a ground truth obtained with a dataset or manually constructed that corresponds to a pixel map where known changed and unchanged areas are represented. We will then compute a ROC (Receiver Operating Characteristics) curve that represents the PD (probability of detection) versus the PFA (probability of false alarm).

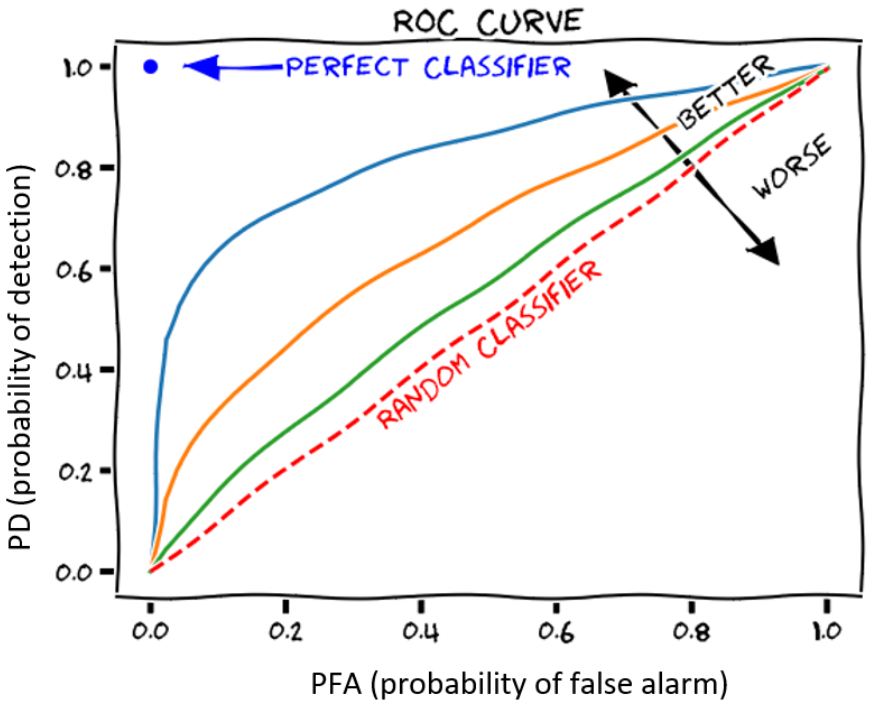


Figure 3.3: representation of a ROC (Receiver Operating Characteristics) adapted from [12]

In practice, a set of thresholds is used to generate binary change maps from a similarity test. Comparing each of the binary change maps with the ground truth, it is possible to calculate the PD and PFA empirically for each threshold as follows to construct the ROC curve:

$$PD = \frac{TP}{NT} \tag{3.12}$$

TP corresponds to the number of true positive detection and NT the number of pixels defined as

target pixels (changed pixels).

$$PFA = \frac{FP}{NB} \tag{3.13}$$

FP corresponds to the number of false positive detection (false alarm), and NB the number of pixels defined as background pixels (unchanged pixels).

As presented in figure 3.3, a straight line with PD=PFA is the characteristic of a random detector (worst possible). On the contrary, for a given probability of false alarm, if the probability of detection is higher, we can consider that this algorithm's detection performance is better. For instance, the blue curve represents better detection than the orange and green curves. The main advantage of this representation is that it is possible to compare different algorithms, even though their statistics and computation are different.

## 3.3 Challenges to highlight ephemeral targets with Change Detection

We introduce first some vocabulary frequently used for target detection:

- Noise: random signal inherent to the measurement
- Target: object of interest
- Clutter: signal part of the background that is not target and not noise

Target, in the thesis, refers to an ephemeral object that possesses the ability to move (be present or be absent) in acquisitions of SAR images. More specifically, our interest is focused on vehicles or vessels. Therefore, these objects can remain for several acquisitions at the same position, leave, come back or another object can take its place. It has not to be mistaken with GMTI (Ground moving target indication) applications, where the goal is to detect objects that possess the ability to move during the acquisition of SAR images. The targets in our interest can be moving during the acquisition or can be stationary during the acquisition. In this section, we present the concept of target detection using change detection. First, we recall some challenges related to target detection using only one SAR image. In the second part, we present the difficulties encountered when considering change detection for target detection using two or more SAR images.

### 3.3.1 Challenges of target detection with one SAR image

ATR (Automatic Target Recognition) aims to gather information with a sensor (usually radar) and decide whether the signal contains a target part of a dictionary. The detection (usually

called prescreening) is a preliminary step to extract possible target candidates according to their statistical and/or physical attributes. For SAR imaging, when the target can be defined only as a bright point in a homogeneous lower amplitude background (ships in the open sea), CFAR (Constant false alarm rate) [5] detectors are usually considered.

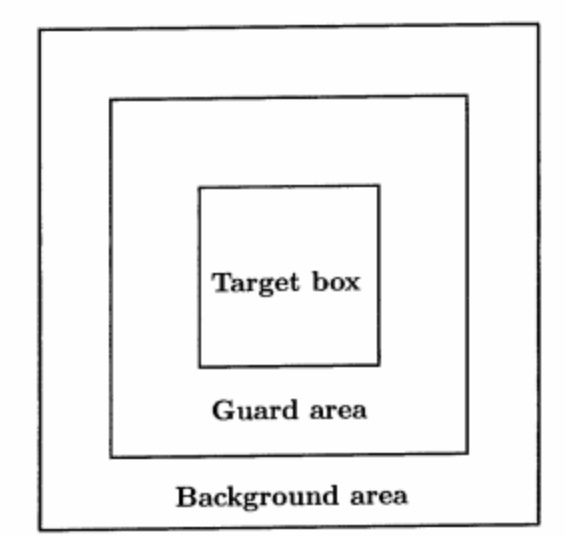


Figure 3.4: Classical spatial CFAR detectors representation

[4] presents a review of CFAR filters based detection method for SAR images. In a few words, the statistical characteristics of the background frame (or ring) are compared with the one from the target box using a sliding window, as presented in figure 3.4. A guard area is used to ensure that the background doesn't contain possible pixels from the target itself and from other targets. The detection threshold is computed according to a given model of the background statistics and satisfies a theoretical constant probability of false alarm; this is why it is called a CFAR detector. When the background is made of bright pixels (urban areas, a forest at low frequency, rough sea), the CFAR filters become more complicated to use. According to the environment, some methods are generally defined where physical and statistical models of both targets and clutter are necessary. In chapters 7 and 8, several considerations will be presented for target detection. In particular, we will focus in this thesis on two difficult environments for target detection: the first one is the detection of ships in the harbor environment; the second is the detection of vehicles concealed under foliage. When the target is not known a priori, it is difficult to evaluate with only one image if the object of interest belongs to the environment or if it is supposed to be present a the moment of the SAR acquisition. When two or more SAR images of the same scene are available,

[5] The name CFAR has been given because they possess the CFAR property, meaning that the choice of an adaptative threshold that depends on the background satisfy a constant false alarm rate

it is possible to introduce temporal information to decide whether an object seems to be part of the static background or not.

### 3.3.2 Target Detection with two or more SAR images

When two or more images of the same scene are available, change detection (CD) is a good candidate to detect a target in a high clutter environment. Indeed, if the clutter remain temporally stable (between acquisitions), the change information will consist only of ephemeral events. They include the targets of interest that were present at a given day. Suppose a scene is without ephemeral targets, for instance acquired during dedicated measurement campaigns. In that case, this SAR image can be used as a reference to produce a change map when compared with a mission image containing possibly targets. In the context of open data (Sentinel 1, UAVSAR or any continuous monitoring system), the image content is unknown and the precedent strategy becomes more ambiguous because the result is a relative change between unknown scenes.

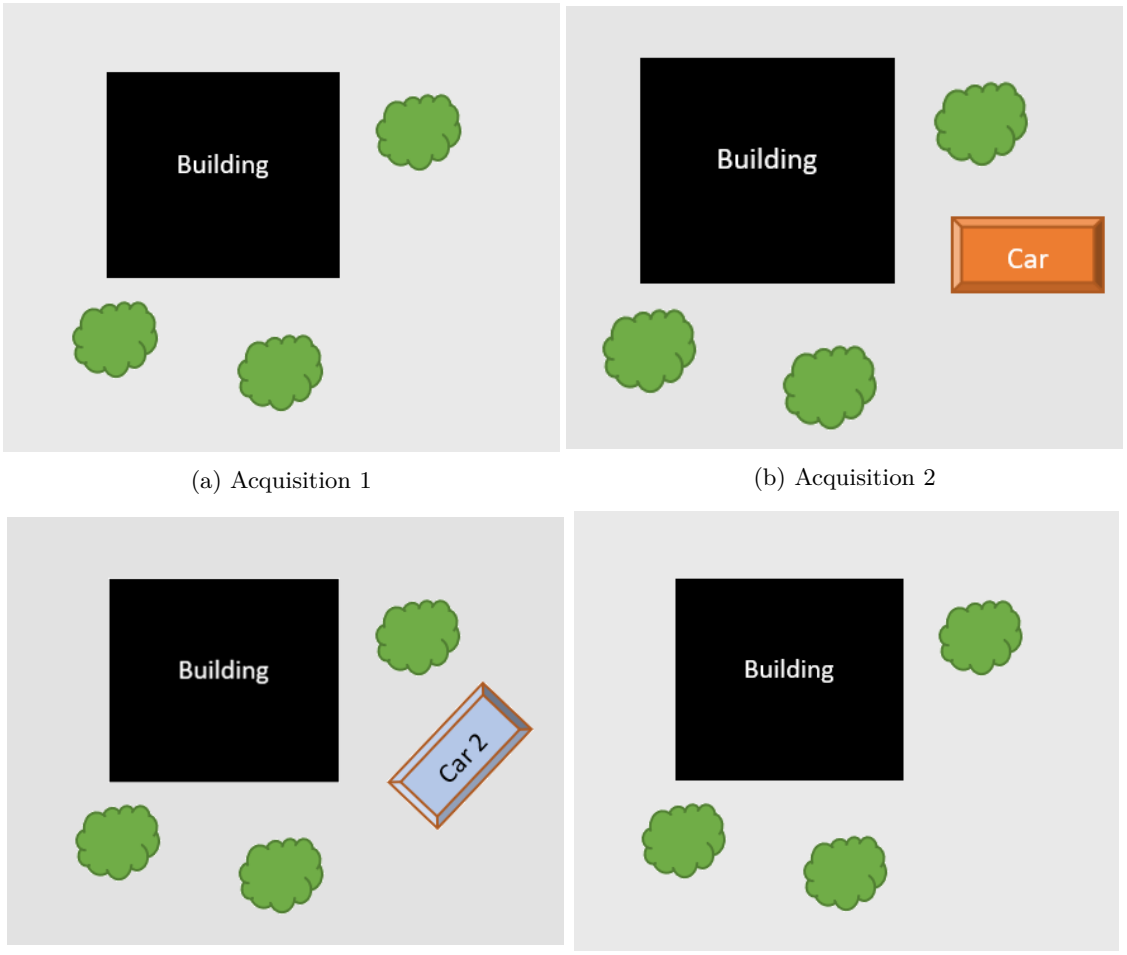


(a) Acquisition 1

(b) Acquisition 2

(c) Acquisition 3

(d) Acquisition 4

Figure 3.5: Illustration of temporally overlapping targets situation

Notably, we call "temporal target overlapping" a phenomenon when a target is present at the two dates of change detection. It can typically happen in dense areas such as industrial harbors near mooring quays or parking areas. The result is a relative change between two targets, which may or not have different sizes, shapes, and orientations. It generates some misinterpretations on the change map; the outcome cannot be interpreted as a target's presence or absence. We use a simplified illustration in figure 3.5 to highlight this phenomenon. We consider a background scene of temporally stable structures at acquisition 1 (a building and trees). A car appears at acquisition 2, and another one takes its place at acquisition 3, acquisition 4 is again the background scene. In the context of a chronological bi-temporal framework, acquisition 2 and acquisition 3 would produce a change detection result shown in figure 3.6. The result is the relative signatures between the two cars. It can produce therefore parasitic signatures if the targets are of different shapes, or no change if the same target remains at the same position. The best reference image that we would take if we wanted to obtain the signature of the targets present in acquisition 2 and 3 is obviously acquisition 1 or acquisition 4. However, in practice, SAR images' content is unknown, and it is not possible to define a reference scene without ephemeral targets.

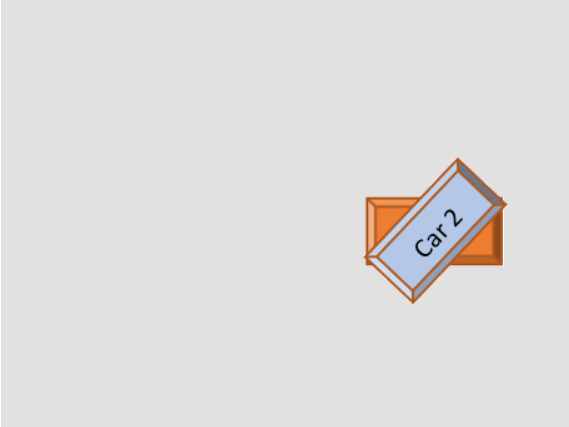


Figure 3.6: Outcome of a change detection between acquisition 2 and acquisition 3: the spatio-temporal overlapping of target generates a undeterminated outcome that depends on the relative signature of each target

This simplified configuration raises the concept of a temporally stable background scene and ephemeral object detection that we aim to investigate during the thesis. Firstly, we aim to generate a background reference image representative of the stable structures within the time-series called FBR (Frozen Background Reference) image. Secondly, a change detection between this FBR image and another image would finally lead to detecting the ephemeral objects at each acquisition.

## 3.4 Discussion

Target detection in SAR time-series seems at first sight trivial to solve because we can associate their temporal behavior with step changes or impulsive changes. However, the detection of vehicles or vessels becomes more ambiguous because, in high attendance areas, their space-time overlapping implies relative comparison, leading to misinterpretation of detection. It seems, therefore, more comfortable to have a target-free scene with only an immobile background that can be used for comparison and thus improve the visualization, the interpretation and detection of a possible ephemeral objects for a given acquisition.

On the one hand, we can encounter some difficulties detecting target using only one SAR image because this target might have the same or close properties to the surrounding objects in the background. On the other hand, using time-series of SAR images might lead to misinterpretation due to temporally overlapping ephemeral objects.

We propose to benefit from pixels' intrinsic temporal characteristics to build a reference image called Frozen Background Reference (FBR) image that will consist only in temporally stable structures in the time-series. From this FBR image, change detection can be performed with any other SAR images to highlight ephemeral targets at a specific date.

**Conclusion** :

In this chapter, we presented an overview of change detection techniques for SAR time-series. We highlighted two main philosophies: the first one relies on bi-temporal frameworks that perform cross-tests exhaustively or sequentially between SAR time-series images, whereas the second one considers overall temporal homogeneity test and looks for ruptures within the time-series. In this context, we presented the benefit of change detection methods in the case of target detection in a high clutter environment compared to a target detection method based on a single SAR image. As a drawback, when SAR time-series are considered, targets might overlap in time and generate misinterpretation issues in high attendance environment. The target-free scene concept has to be introduced to solve those issues and enable proper target detection.

# Part II

# A NEW STRATEGY FOR CHANGE DETECTION IN SAR IMAGERY

**The Frozen Background concept**

As presented in the previous chapters, the CD is an interesting strategy for the detection and study of targets within a high clutter scene. In multitemporal SAR images, the detection of ephemeral objects becomes challenging because targets-free scenes are in practice not available. In SAR time-series analyses, most of the developed algorithms are designed to detect relative changes. They can lead to misinterpretation when the purpose is to detect the amount of ephemeral (non stationnary) scatterers at a given date in high attendance areas where the overlapping temporal probability of target is high. The main advantage of current and future continuous SAR remote sensing platforms (Sentinel 1 for instance) is the short revisit time between acquisitions (12 days or 6 days with a combination of platforms acquisitions). We can notice that, in the optical remote sensing community, continuous monitoring is common, whereas it is less present in SAR remote sensing. Considering SAR systems that are constantly and repetitively monitoring the earth, we aim to introduce a concept of temporally stable background image that we will call Frozen Background Reference (FBR) image.

The application of this FBR image is mostly dedicated to CD in this thesis. Considering in the future that revisits time for SAR sensors will be smaller, it might be interesting to adapt the strategies of detection. We aim to consider the problem of ephemeral object detection more as a background removal/foreground detection problem as it would be done in surveillance camera applications. For CD applications and especially target detection, the ground truth of an observed scene is usually unknown, and reference target-free SAR image is not available. In this part, the chapter 4 will introduce the concept of FBR image from a stack of SAR time-series. Its concept and computation through a selection of temporally stable pixel strategy will be presented. In the Chapter 5, we present illustrations of FBR images with simulations and real SAR images cases at C-Band (spaceborne) and L-Band (airborne). Finally in the Chapter 6, we introduce the strategies of change detection in the frame of FBR images.

**Content of the part II** :

- Chapter 4 : Frozen Background Reference Image from SAR time-series
- Chapter 5 : Simulation and illustrations of FBR images
- Chapter 6: Change Detection strategies in the context of FBR images

# Chapter 4

# Frozen Background Reference Image from SAR time-series

**Objectives** : This chapter aims to introduce the concept of Frozen Background Reference (FBR) image in SAR time-series. With this FBR image, we seek to illustrate a temporally stable behavior of an observed scene representing the permanent scatterer and the temporally stable clutter noise within a series of SAR images. The concept of SAR time-series homogeneity will be approached and the process developed to compute this FBR image. Its computation will be performed with simulated SAR data, real spaceborne and airborne datasets at C-Band and L-Band.

We propose introducing a new concept called Frozen Background Reference (FBR) image that aims to compute a radiometric image consisting only of the contribution of the temporal pixels that are electromagnetically or statistically stable within SAR time series. It corresponds to the signature of immobile objects and clutter noise that remain without temporal ruptures. The resulting image is said to be a "reference" image because it aims to represent an ephemeral target-free scene in our context of target detection, whereas a "mission" image is defined as an image where possibly ephemeral targets are present. In this chapter, we investigate and illustrate the feasibility of such a method by addressing the following aspects. First, the FBR concept and the possible approaches to generate a scene representative of a temporally static background are described. To do so, we will exploit the temporal variation coefficient introduced in chapter 3. We will illustrate its behavior in time-series of SAR images with three specific points like PS (Permanent Scatterer), unchanged low backscattering areas, and high attendance areas to illustrate experimentally its

properties. Finally, the stable pixels selection strategy and the computation of FBR image will be described.

## 4.1 Introduction to FBR concept

The concept of such a method can be seen as an analog version of background removal/foreground detection in video surveillance applications with different physical and statistical considerations due to the evident different acquisition principles. In the SAR community, few studies tackled the problem of stable background representation and computation. We found one research study that considers this problem [80] in the frame of CD where the amplitude time-series of SAR images are represented as AR (autoregressive) models that aims to predict the most probable state of the pixels for each range and azimuth. Afterward, the difference is performed between the estimated image and the mission SAR images.

### 4.1.1 FBR concept and link with other fields

The background removal in video surveillance is a wide field of research where different strategies have been developed through the last 30 years [81, 82, 83].

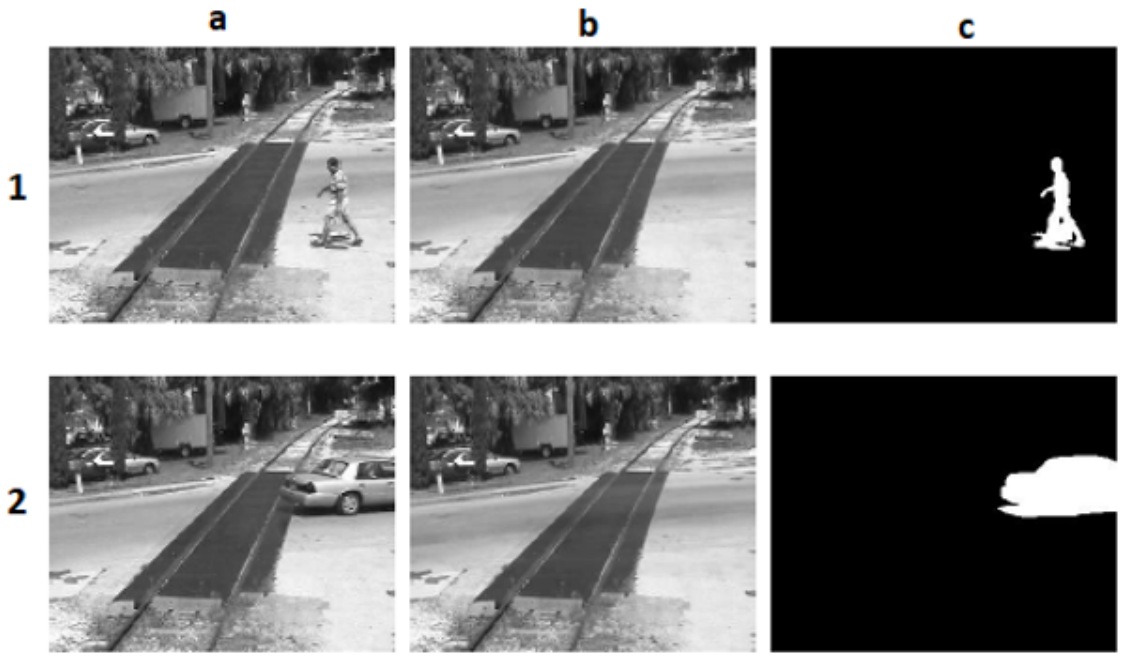


Figure 4.1: Background removal and Foreground detection in video-surveillance applications from [13]. (a.1) Man walking, (a.2) Car passing, (b.1) Background image, (b.2) Background image, (c.1) Change detection between images a.1 and b.1 and (c.2) Change detection between images a.2 and b.2

Usually, for video-surveillance applications, the background image can be set by recording images without foreground object (ephemeral object), and then a change detection can be performed with an incoming image with the background image to obtain the foreground objects in the scene. As we can see in figure 4.1, the images denoted a.1 and a.2 contains a foreground objects that appeared (respectively a man and a car). The images b.1 and b.2 are the same background image that correspond to a usual state of the scene. The change detection from the background image of the images a.1 and a.2 therefore produces the images c.1 and c.2. In that case, if we consider that the background image has been set manually when no object where present, the detection of foreground objects is directly possible. In the Chapter 1 of the survey on video-surveillance applications proposed in [13], the problem under background removal and foreground detection in video-surveillance applications appear to be similar with the purpose of our study. Indeed, it is sometimes impossible in practice to obtain such background image so that strategies have to be implemented to generate a scene without ephemeral objects. However, we can only observe that the problematics are similar. As the sensor and the data collection are significantly different, we have to propose a methodology that is adapted to SAR time-series to solve this problem.

### 4.1.2 FBR framework for SAR time-series

We introduce here the concept of FBR framework and its possible applications for SAR time-series. The purpose of the FBR image processing is to generate an image that represents a temporally stable behaviour of a scene for a given period of acquisition. We will then select in the time-series at each range and azimuth, a set of pixels that represent a temporally stable behavior of the scene and gather them into an image called FBR image. We want to compute an ephemeral target-free image representing an electromagnetically (permanent scatterers) and statistically (clutter noise and speckle) stable state of the scene. The general framework is presented in figure 4.2. The framework takes as input a temporal serie of SAR images, select pixel that are temporally homogeneous and compute the FBR image. Then for any SAR image, we can perform a change detection to obtain the ephemeral objects at a given date. Other strategies may be based on the change detection between FBR images computed over different seasons to obtain an overall change at a different time scale (that would be related more to changes established in time). We can consider as well to update the FBR image taking into account the outcome of the change detection.

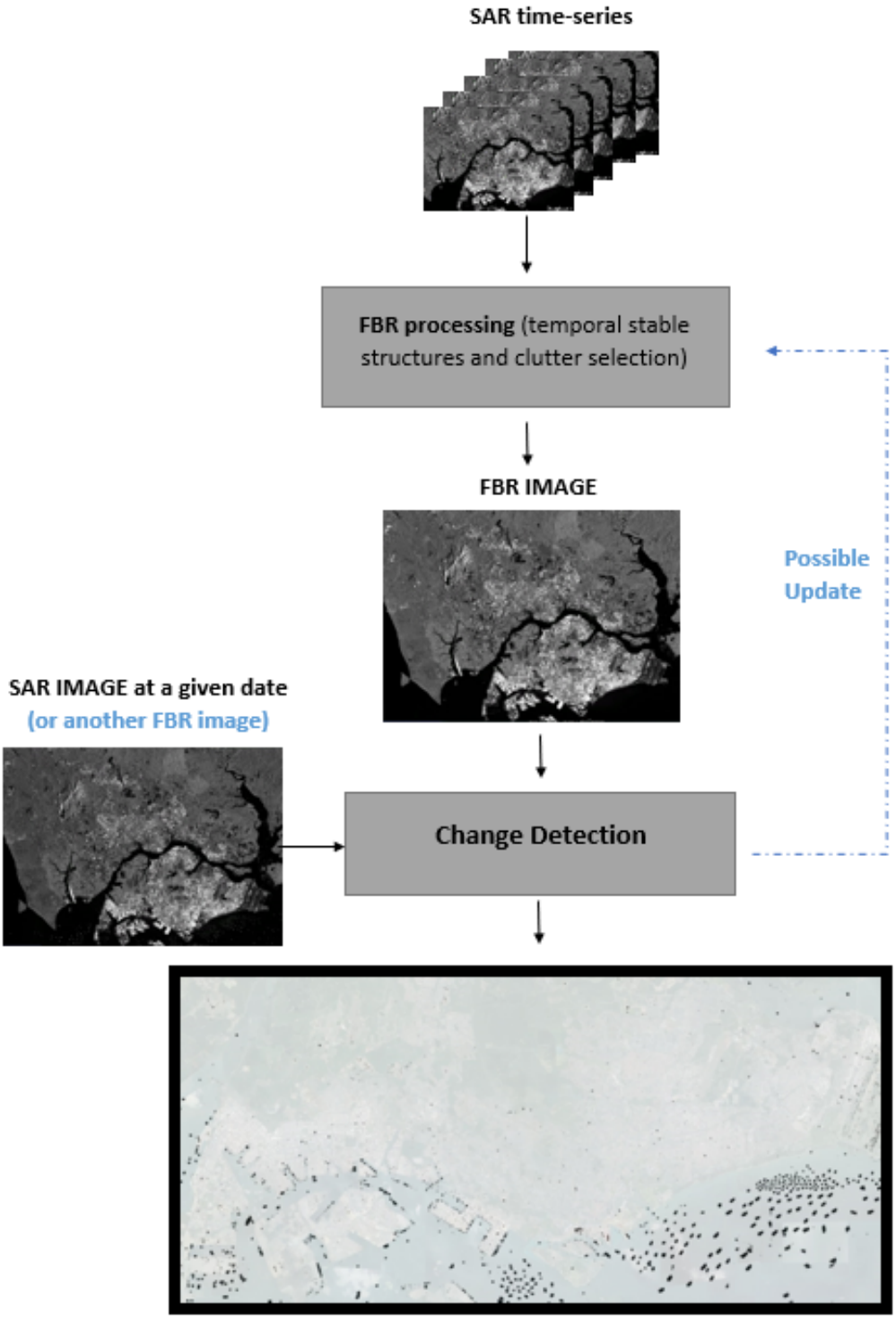


Figure 4.2: Illustration of FBR framework and example of objects detected the 02 March 2019 in the region of Singapore projected on Google Earth optical image in background: black points represents where the most significant changes occurred compared to the FBR image

In this thesis, change detection with another FBR image and the update of the FBR image has not been studied but can be investigated for future works.

For this study, we focused on the detection of ephemeral objects. The illustration in figure 4.2 corresponds to a example of a change detection between a FBR image computed over three years (2017 to 2019) and a Sentinel 1 acquisition from the 2 March 2019. The most significant ephemeral events detected at this date are indeed the ships due to their metallic structures and sizes compared to the 20 by 20 m resolution of Sentinel 1 GRD images. This image serve as a visual illustration of the results, the specific aspect of maritime surveillance applications using FBR framework will be presented in the chapter 7.

In the following section we will approach the temporal behavior of pixels using the time-series presented in chapter 2: a set of 83 GRD images acquired in Singapore by Sentinel 1 above the industrial harbor of Jurong Island and the UAVSAR dataset of 68 acquisitions acquired above the industrial area of Pittsburgh in the region of San Francisco.

## 4.2 Pixels temporal behavior study using CV

In SAR time-series analyses, the radiometric temporal stability is usually addressed through permanent scatterer study using interferometric coherence. However, as we discussed in the chapter 3, the use of interferometric coherence is not suitable in our case because the information of change is lost in low backscattering areas.

In the specific application of ephemeral objects detection such as vehicles or vessels, a pragmatic point of view is to consider that if an object can appear in the scene at a given pixel, this pixel should represent a physical structure that allows it to be present: the surface of a road, the sea, a parking area or a place adjacent to mooring quays. We notice that these locations are in general low backscattering areas because only a small part of the signal is backscattered toward the radar. In addition, for the selection of the pixels, we do not want to mix spatially possible targets with the background by using spatial estimation windows. We will then use the variation coefficient (CV) introduced in chapter 3 that possesses interesting properties.

We recall here the theoretical variation coefficient for a Rayleigh-Nagakami law, representing the statistical amplitude behavior of an untextured speckle area image with L number of looks:

$$CV_{theo} = \sqrt{\frac{\Gamma(L)\Gamma(L+1)}{\Gamma(L+\frac{1}{2})^2} - 1} \tag{4.1}$$

In addition, we illustrate in the figure 4.3 the expected CVs from specific temporal behaviors in SAR time-series. Permanent scatterer and pure speckle are supposed without temporal ruptures and the inhomogeneous temporal behavior symbolizes possible ruptures in the time-series.

$CV^1_{theo}$ and $CV^{4.9}_{theo}$ represent respectively the theoretical CV for a SLC SAR products (L=1)

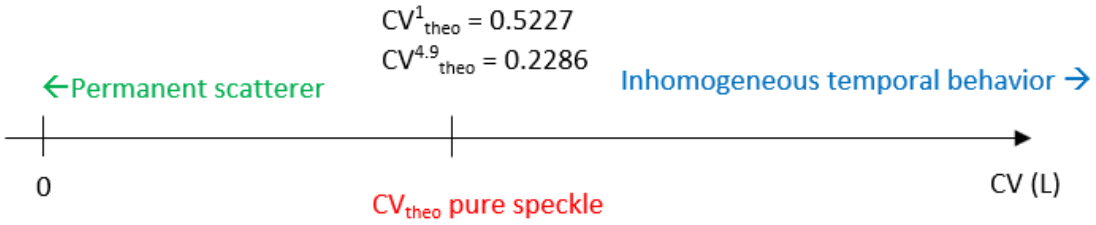


Figure 4.3: Theoretical schematic representation of temporal specific points CV

and a Sentinel 1 GRD products (L=4.9). We will then illustrate the behaviour of the CVs with examples of specific points from SAR time-series (permanent scatterer, sea surface not affected by the presence of ships and high attendance area near a mooring quay) in comparable environments at C-Band and L-Band.

### 4.2.1 Harbor environment Singapore (C-Band)

For this study, we choose three specific points of the image figure 4.4a : a permanent scatterer (green), a pixel subject to the appearance of ships (blue) and a sea pixel non affected temporally by the presence of a ship (red). We will denote therefore $CV_{PS}^{VV}$, $CV_{PS}^{VH}$, $CV_{Quay}^{VV}$, $CV_{Quay}^{VH}$, $CV_{Sea}^{VV}$ and $CV_{Sea}^{VH}$ the associated CV for a permanent scatterer, the pixel adjacent to the quay and the unchanged sea pixel for VV and VH. The temporal behavior of these pixels is plotted 4.4b over the 83 dates with the corresponding colors defined above; the plain line is for VV polarisation and plain line with stars for VH polarisation. The CV results, gathered in the table 4.1, shows that $CV_{PS}^{VV} = 0.046$ and $CV_{PS}^{VH} = 0.048$ are low compared to the two other pixel configurations CVs due to the large mean value and low variance of PS. From the theoretical value calculated from equation 4.1 with L=4.9 (in this case for the Sentinel GRD dataset) we obtain $CV_{theo}^{4.9}$=0.2286. The sea pixel statistical behavior can be considered as a stable speckle for calm sea and the results are consistent with the theoretical calculation of $CV_{theo}^{4.9}$ comparing $CV_{Sea}^{VV} = 0.1807$ and $CV_{Sea}^{VH}$=0.2281.

| Temporal CV computed for PS, Quay and Sea pixels | | | |
|---|---|---|---|
| Polarisation | PS | Quay | Sea |
| VV | 0.046 | 1.096 | 0.190 |
| VH | 0.048 | 0.893 | 0.228 |

Table 4.1: CV (Variation coefficient) calculated for 3 specific points Singapore

Finally, for the pixel near the quay, $CV_{Quay}^{VV} = 1.096$ and $CV_{Quay}^{VH} = 0.8932$ showing a high CV

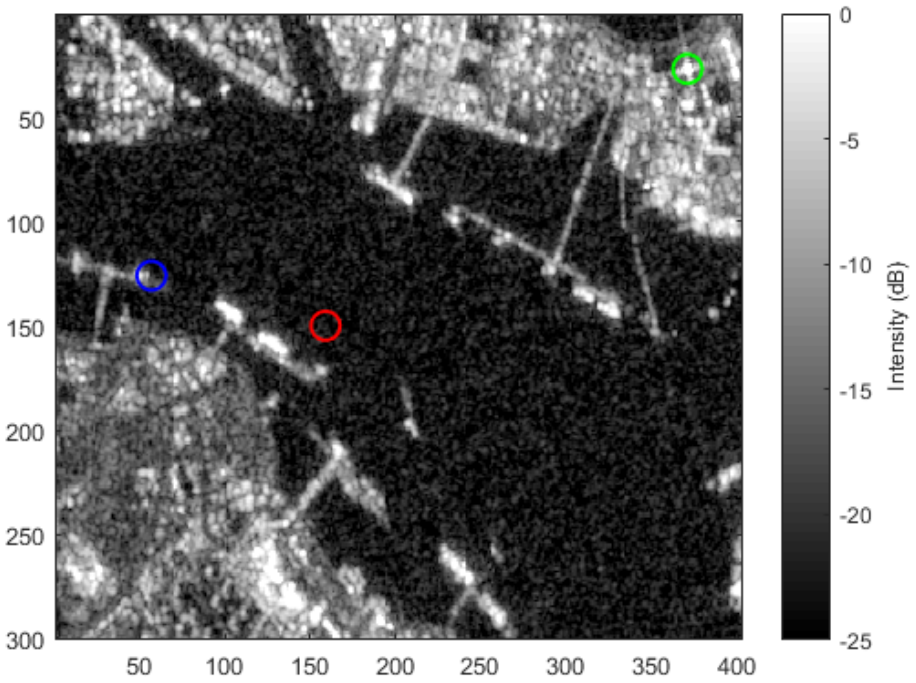


(a)

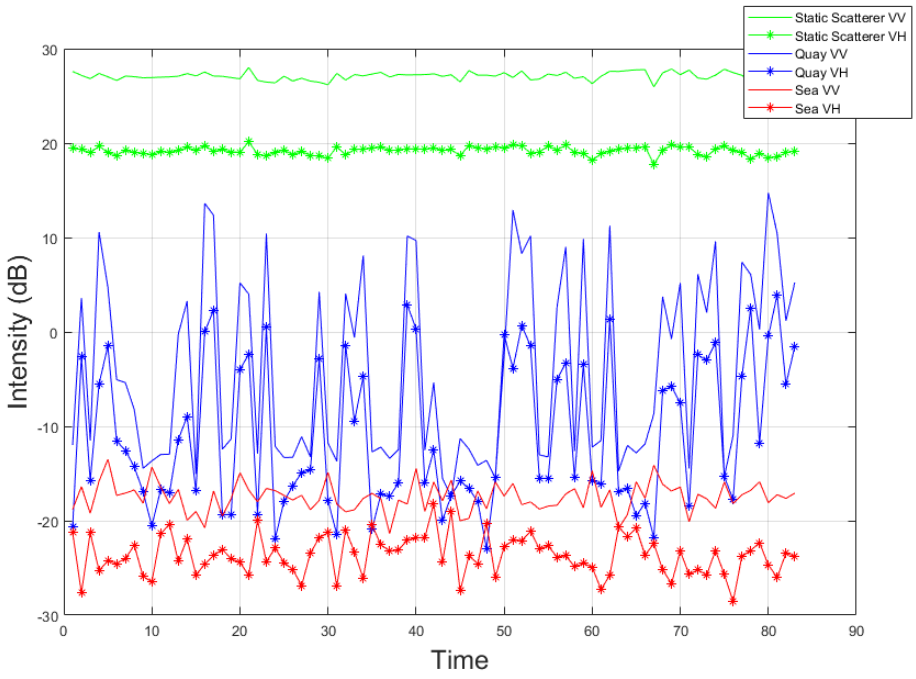


(b)

Figure 4.4: (a) Radiometric Image Singapore 5 Feb 2017 Sentinel 1 GRD VH and associated specific study points : Permanent scatterer (green), mooring quay (blue) and sea surface (red). (b) Temporal VV and VH Intensities for Singapore Sentinel 1 GRD: permanent scatterer in green, sea surface in red and changed area near mooring quay in blue

compared to the other specific pixels. As we can observe from these results, the variation coefficient of the permanent scatterer seems independent of the polarisation and inferior to $CV_{theo}^{4.9}$=0.2286. The polarisation plays a slight role for the temporal CVs of the sea pixel and its contribution is more important for the configuration where ships were present during the acquisitions (several ruptures during the time-series). For the sea pixel and the PS pixel (red and green curve in figure 4.4b), we can observe that the temporal behavior between the two polarisations can be seen as a shift in dB whereas for the pixels near the quay where ships where present at several acquisitions, it seems more complex. An explanation might be due to the asymmetric shape of ships that generates possible strong variations between VV and VH for a given acquisition, therefore the variation coefficient is high however they do not systematically produce the same patterns of rupture in time. Experimentally we can observe for these specific points that $CV_{PS} < CV_{Sea} \approx CV_{theo}^{4.9} < CV_{quay}$ which corroborate relatively well the theoretical expectations.

### 4.2.2 Harbour environment San Franscisco Region UAVSAR (L-Band)

We conducted the same study on the 68 UAVSAR images above the San Francisco region, this time using L-band to evaluate if the behavior and properties of CV can be verified experimentally on equivalent specific points. Specific points are chosen and presented in figure 4.5a. This is an SLC product so we consider that L=1 in this case and $CV_{theo}^{1} = 0.5227$. We can notice that $CV_{sea}$ is above the theoretical variation coefficient for the three polarisations, especially for VV and HV according to the table 4.2. It is not an expected result however we noticed that this SAR time-series suffers from strong interferences within five acquisitions that may perturbs the expected statistical behavior[1]. Computing the statistics without the images containing strong interferences lead to the results in the table 4.3. In that case, $CV_{sea}$ is still higher than the theoretical value for VV but is close to the theoretical values for HH and HV.

As it seems, the variation coefficient is extremely sensitive to outliers in pure speckle noise, we can observe more consistent results with the theory after removal of the images containing interferences. $CV_{quay}$ is high as expected for the three polarisations and the removal of the 5 images with interferences has a small effect since it has already a strong temporal inhomogeneous behavior.

The same remark can be made for $CV_{PS}$ for each polarisation regarding the impact on the removal of the 5 images with interferences. Indeed, the PS having already a strong backscattering signal, the interferences are relatively smaller and therefore impact very few the behavior of the

[1] images 44,45,55, 62 and 64, resp. 25 November 2013, 16 January 2015, 27 April 2015, 04 February 2017 and 1 April 2017

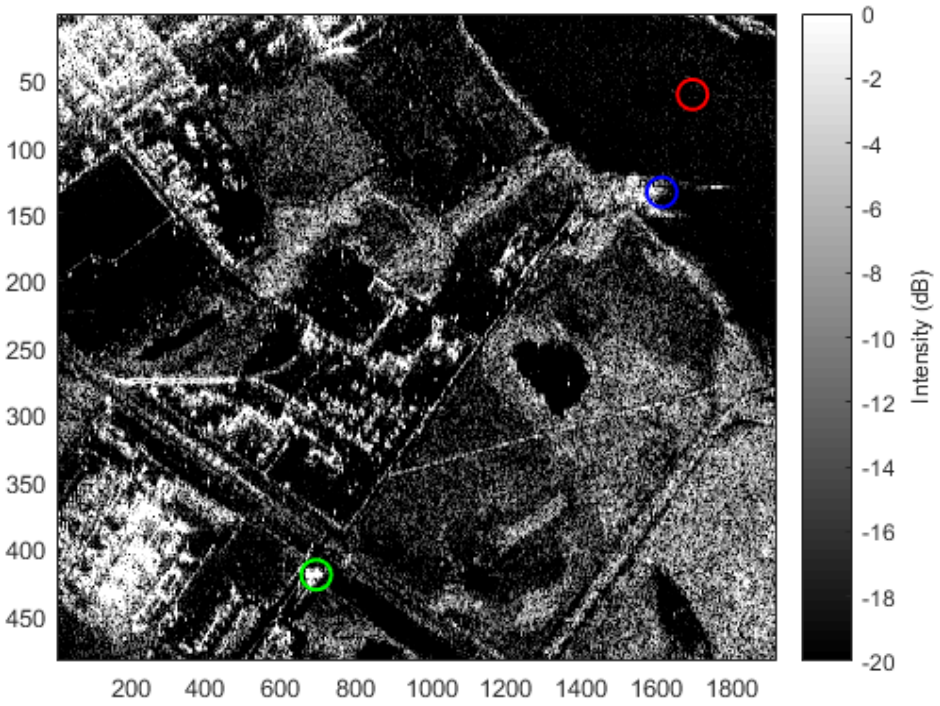


(a)

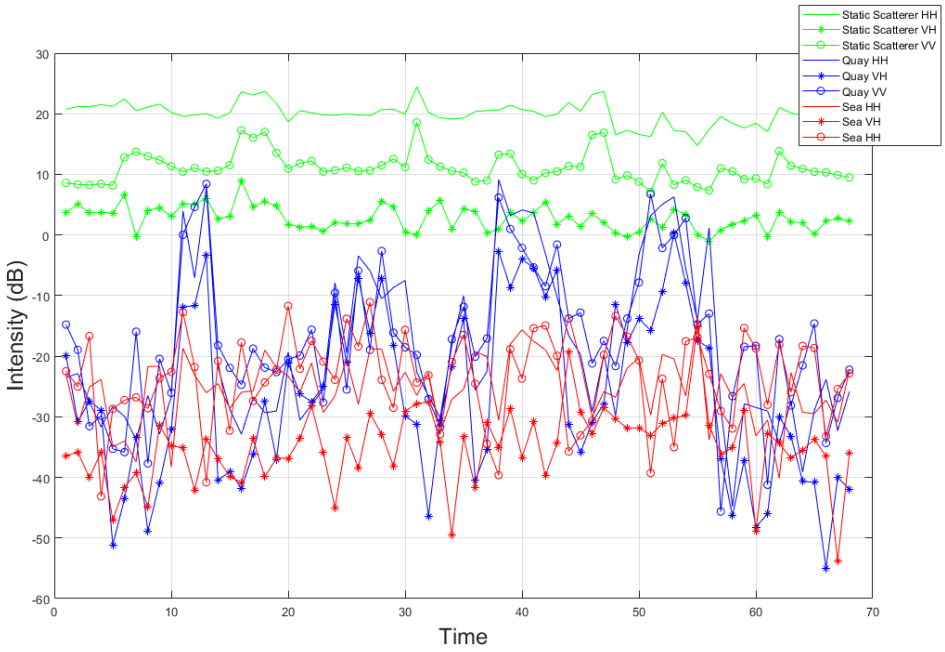


(b)

Figure 4.5: (a) UAVSAR Radometric image HH: permanent scatterer in green, sea surface in red and changed area near mooring quay in blue. (b) Time-series San Fransisco Region with 3 specific points: Permanent scatterers (green), mooring quay (blue) and surface of the sea (red)

.

| Temporal CV computed for PS, Quay and Sea pixels | | | |
|---|---|---|---|
| Polarisation | PS | Quay | Sea |
| VV | 0.310 | 1.564 | 0.825 |
| HV | 0.231 | 1.451 | 0.708 |
| HH | 0.214 | 1.671 | 0.610 |

Table 4.2: CV calculated for 3 specific configuratiosn San Francisco

| CV computed for PS, Quay and Sea pixels (5 Images with interferences taken away) | | | |
|---|---|---|---|
| Polarisation | PS | Quay | Sea |
| VV | 0.335 | 1.551 | 0.652 |
| HV | 0.240 | 1.425 | 0.516 |
| HH | 0.215 | 1.609 | 0.521 |

Table 4.3: CV calculated for 3 characteristics configuration San Francisco without the images containing interferences

PS.

The overall behavior seems to follow the underlying assumptions made for the CV, however some variations can be observed depending on the polarisation, especially for VV. As it is theoretically defined, the variation coefficient for SLC products (L=1) is higher than the variation coefficients for Sentinel 1 products (L=4.9). The behavior of CV depending on the specific points follows relatively well the theory that $CV_{PS} < CV_{Sea} \approx CV^1_{theo} < CV_{quay}$ for each polarisation.

### 4.2.3 Discussion

Through this experimental study, we could illustrates the properties of CV for specific pixels and note that the CV of PS is in general low, the temporally homogeneous speckle pixels give a higher CV relatively close to the theoretical value and finally the temporally inhomogeneous pixels give a much higher CV so that it will be possible to distinguish them by temporal analysis. The main advantage of the temporal CV is that pixels are kept spatially unmixed at this stage and only the intrinsic temporal behavior is taken into account. The theoretical standard deviation of the CV decreases by $\sqrt{(}D)$, D being the number of acquisition dates, as shown in equation 4.2 [73]:

$$std(CV_{theo}) = \sqrt{\frac{1}{4D}\frac{L\Gamma(L)^4[4L\Gamma(L)^2 - 4L\Gamma(L+\frac{1}{2})^2 - \Gamma(L+\frac{1}{2})^2]}{\Gamma(L+\frac{1}{2})^4[L\Gamma(L)^2 - \Gamma(L+\frac{1}{2})^2]}} = f(\frac{1}{\sqrt{D}}) \tag{4.2}$$

This simply highlights that, benefiting from longer time-series, enables to obtain a better es-

timation of the variation coefficient. In addition, since the CV depends theoretically only on L (number of looks) and is independent on the mean value of the speckle noise, we can consider the CV as a good tool to describe the homogeneity of time-series. From a theoretical point of view, the CV does not depend on the polarisation or the frequency which is a strong hypothesis and may have to be considered in future studies. Here, we want to benefit from the temporal variation coefficient to detect, for each range and azimuth, the pixels for which the temporal homogeneity is not respected. The first challenge of our process is to select for each range and azimuth, a set of pixels that form a temporally homogeneous group so that their coefficient variation satisfy a given theoretical threshold.

## 4.3 Pixels selection for the FBR image

In this section, we present the method of pixel selection developed for the computation of the FBR image in the monopolarisation case and the polarimetric case. We note $\boldsymbol{s} = [s_1..s_D]$, the temporal complex valued signal collected by the sensor for a given range and azimuth, we denote $\boldsymbol{\alpha} = [|s_1|..|s_D|] = [\alpha_1..\alpha_D]$ the amplitude (magnitude) corresponding time-series vector at a given range and azimuth where $|s_d|$ is the module of the complex value $s_d$ at a date d. Since we will consider only the pixel in the temporal domain and for any polarisation for the selection, the notation has to be understood as a simplified notation of $\boldsymbol{s}_{i,j}^{pq}$ and $\boldsymbol{\alpha}_{i,j}^{pq}$ where i and j represent the range and azimuth and p and q the polarisation. Then our goal is to find a set of pixels gathered in a new vector $\tilde{\boldsymbol{\alpha}}$ containing $D' \leq D$ so that $CV(\tilde{\boldsymbol{\alpha}}) < \psi$ with $\psi$ a given threshold and CV($\bullet$) the temporal variation coefficient of an amplitude time-series samples.

### 4.3.1 Monopolarisation acquisition

The idea under this process is to extract elements in the time-series that engender a temporal inhomogeneity, or reversely we want to keep a group of pixels that conserves a temporal homogeneity according to their variation coefficient. The variation coefficient CV($\boldsymbol{\alpha}$) is then computed iteratively and compared with a threshold $\psi$. At each iteration, we obtain a new output vector $\tilde{\boldsymbol{\alpha}}$ of length $D' \leq D$ where the the pixel presenting the most distant value relative from the mean have been extracted. The algorithm is repeated until the set of temporal remaining pixels satisfy the criterion. Figure 4.6a presents the diagram used to perform such a process.

Computing this selection for every range and the azimuth, we obtain a cube with different dimension in the time direction containing only the selected stable candidate pixels. It is important to note that the selection is performed on the amplitude of the pixels but they are also kept as

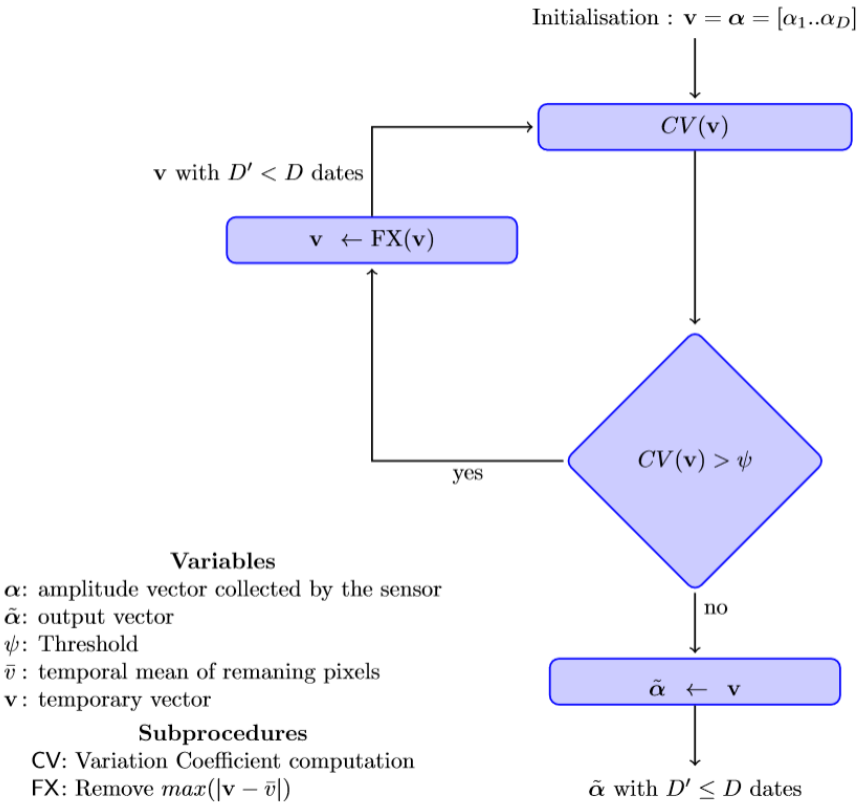


(a)

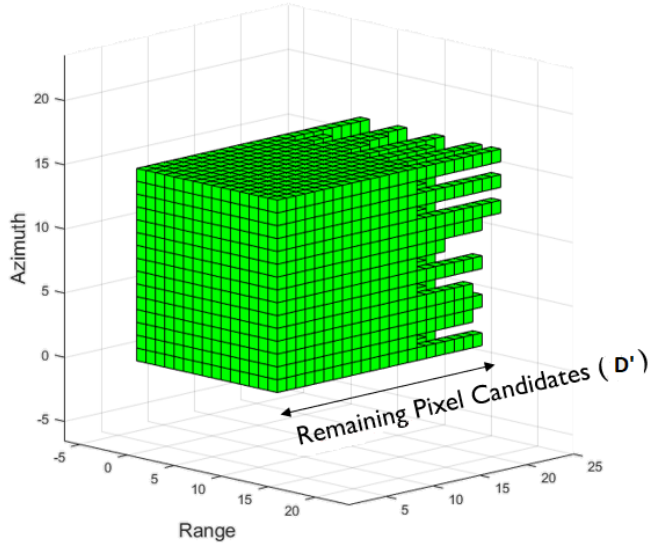


(b)

Figure 4.6: (a) Candidate pixels selection of an amplitude temporal vector $\boldsymbol{\alpha}$ for a given range and azimuth, (b) Cube containing the remanining pixels after selection

well in their complex form. We illustrate such results in figure 4.6b. Therefore we obtain for each range and azimuth a temporal vector $\tilde{\boldsymbol{s}} = [s_1..s_{D'}]$ and its corresponding amplitude (magnitude) vector $\tilde{\boldsymbol{\alpha}} = [\alpha_1..\alpha_{D'}]$.

### 4.3.2 Polarimetric acquisitions

We consider the selection for a polarimetric acquisition as an extension of the previous form with each polarimetric channel processed separately. As a result, only pixels that are remaining for each polarisation are considered . If at least one pixel have been removed in one of the polarisations, the whole polarimetric vector is removed. We obtain therefore a cube for each polarisation as shown in figure 4.7.

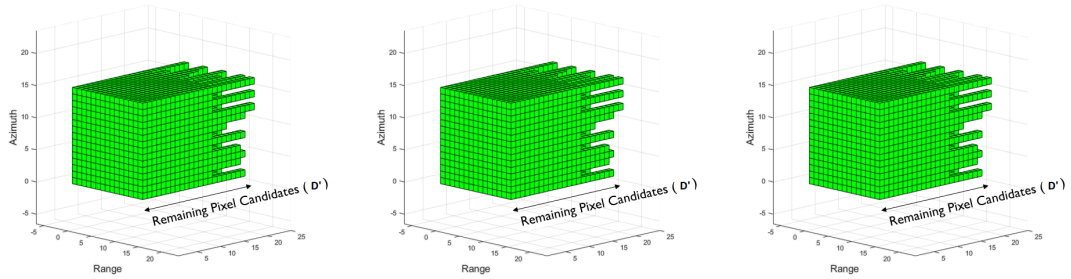


(a) HH (b) HV (c) VV

Figure 4.7: Visual representation of remaining pixels for each polarisation

This procedure can be questioned regarding the physical meaning of the candidate pixels. It has been performed only by the amplitudes and not taking into consideration the phase of the pixels. It is known that the phase itself on one acquisition does not carry useful information but relative phases between polarisation or acquisition does. This solution is a first implementation that have to be improved in the future.

### 4.3.3 CV Threshold

As presented in 3.11, the theoretical variation coefficient depends only on L (Number equivalent of looks) that can be estimated as proposed in [84]. It also has the interesting property to not to depend on the average amplitude of the speckle. Depending on the sensor and products available, L can be a parameter given in the characteristic of an image product. For classical SLC images we consider L=1 and for example for Sentinel 1 GRD product L=4.9. As discussed, the variance of the CV is a function of $\frac{1}{\sqrt{(D)}}$ D being the number of dates in the time series, the threshold is then defined using the theoretical variation coefficient in equation 3.11 :

$$\psi(i,j) = CV_{theo} + \frac{\eta}{\sqrt{D'(i,j)}} \tag{4.3}$$

$$\psi(i,j) = \sqrt{\frac{\Gamma(L)\Gamma(L+1)}{\Gamma(L+\frac{1}{2})^2} - 1} + \frac{\eta}{\sqrt{D'(i,j)}} \tag{4.4}$$

$\eta$ is a parameter to control the selectivity of the candidate pixels and $D^{'}(i,j)$ the remaining number of stable date for each range $i$ and azimuth $j$. The threshold can be set independent of the amount of the remaining images by choosing $\eta = 0$, in that case, we will use the term "natural" thresholding. In contrast, if we set a value of $\eta > 0$ we will use the term relaxed thresholding because we will enable the set of selected pixels to have a CV higher than the theoretical value. We will use in general a natural threshold unless it is mentioned specifically.

## 4.4 Representation of the FBR Image

Once the stable pixels have been determined in the SAR time-series, different solutions can be considered to represent the FBR image. We chose two different approaches: either to randomly choose a temporal pixel for each range and azimuth or to use the contribution of all remaining pixels for each range and azimuth. Each representation can have advantages and drawbacks that will be discussed in the following chapters depending on the purpose.

### 4.4.1 The random choice of the pixels (RP)

We can consider that, since the remaining candidate pixels are statistically representative of a temporally stable behavior, the random selection of one pixel within the list of pixels is reasonable to represent the background. In that case, the visual quality of the SAR image is not expected to change. The resulting SAR image does not correspond to an actual acquisition and might not be physically interpretable but it represents a stable state of the scene for each range and azimuth. The main advantage of this representation is that the statistical properties of the image are supposed to be conserved according to the images of the SAR time-series.

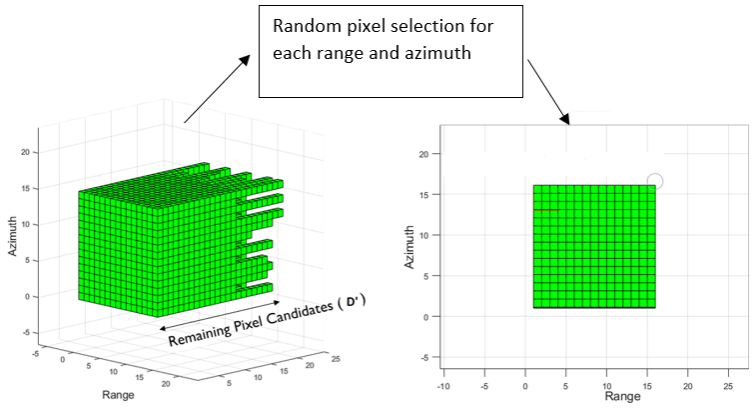


Figure 4.8: Random selection for each range and azimuth from the cube of remaining pixels

### 4.4.2 The use of multitemporal pixels (MP)

We can choose alternatively to represent the FBR image in terms of temporal incoherent mean of the remaining pixels for each range and azimuth. In that case, the visual quality of the image is supposed to be improved since the variance of the speckle noise will be decreased with a factor D' that represent the number of temporal remaining dates in the time-series.

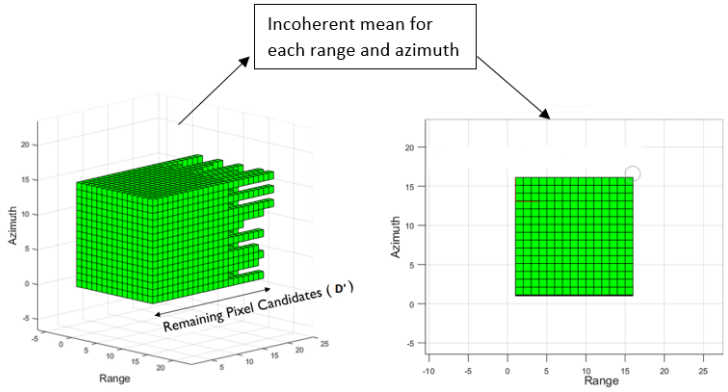


Figure 4.9: Incoherent mean for each range and azimuth from the cube of remaining pixels

## 4.5 Discussion

The main advantage of this selection method relies in the fact that the pixels are considered only temporally so that no spatial mixing is performed between heterogeneous scatterers.
With such pixel selection, we can already highlight some limitations that may be disadvantageous when using time-series over a long period (several years over urban areas for example) because a permanent change such as building construction/deconstruction will not be well interpreted depending on the time when the event occurred. Such event can be however considered as a long term change and a solutions may be addressed by updating the FBR image. The assumption of an underlying background is indeed more relevant considering forthcoming constellation missions with a temporal revisit time of several hours or days for urban monitoring. This remark may be also considered regarding different environments of the observed scene. In the case of forest or natural environments, the acquisition time span to compute the FBR image may also be considered differently depending on the operating frequency. At low frequencies, below L-band, we can intuitively make the hypothesis that an underlying stable background may exist over a longer period compared to acquisitions at higher frequencies. These considerations will have to be thoroughly investigated over future studies.

**Summary** : We presented in this chapter the concept of FBR image and proposed a procedure to obtain within SAR time-series the pixels that are representative of a temporally stable behavior of the scene. We considered for the design of the procedure that the background is only affected by ephemeral objects that sporadically appears in the SAR time-series. Through this procedure, we presented two possible representation of the FBR image : one considering a random pixel (or polarimetric vector) selected from the remaining temporally stable pixels for each range and azimuth and another taking into consideration the whole remaining pixels (or polarimetric vectors) for each range and azimuth.

# Chapter 5

# Illustrations of FBR images computation

**Objectives** : This chapter presents the computation of the FBR image firstly with a set of simulated images and afterward using real SAR images from the same sets presented before (L-Band UAVSAR and Sentinel 1 GRD). With these examples, we investigate the question of number of required acquisitions to generate a representative FBR image.

In this chapter, we investigate the behavior of the FBR image with different configurations of acquisitions. The datasets of real SAR acquisitions used in the precedent chapter to illustrate the behavior of the CV will be exploited this time to present the computation of a FBR image. In a second section we will analyze the impact of the number of acquisitions to generate the FBR image. Finally some illustrations and results will be presented in different configurations.

## 5.1 Simulations

A simulated time series of SAR images is computed with a static object corresponding to a building on the whole time series (big red square in Figure 5.1). The settings for this simulation are presented in Table 5.1. At a given date, five targets appear, as shown in Figure 5.1b with a target Signal-to-Noise ratio SNR = 6 dB.

Table 5.1: Simulation settings

| **Simulation Parameters** | FBR simulation |
|---|---|
| Number of images | 10 |
| Images size | 200 × 200 pixels |
| Building size | 20 × 20 pixels |
| Targets size | 10 × 10 pixels |
| SNR building | 13 dB |
| SNR targets | 6 dB |

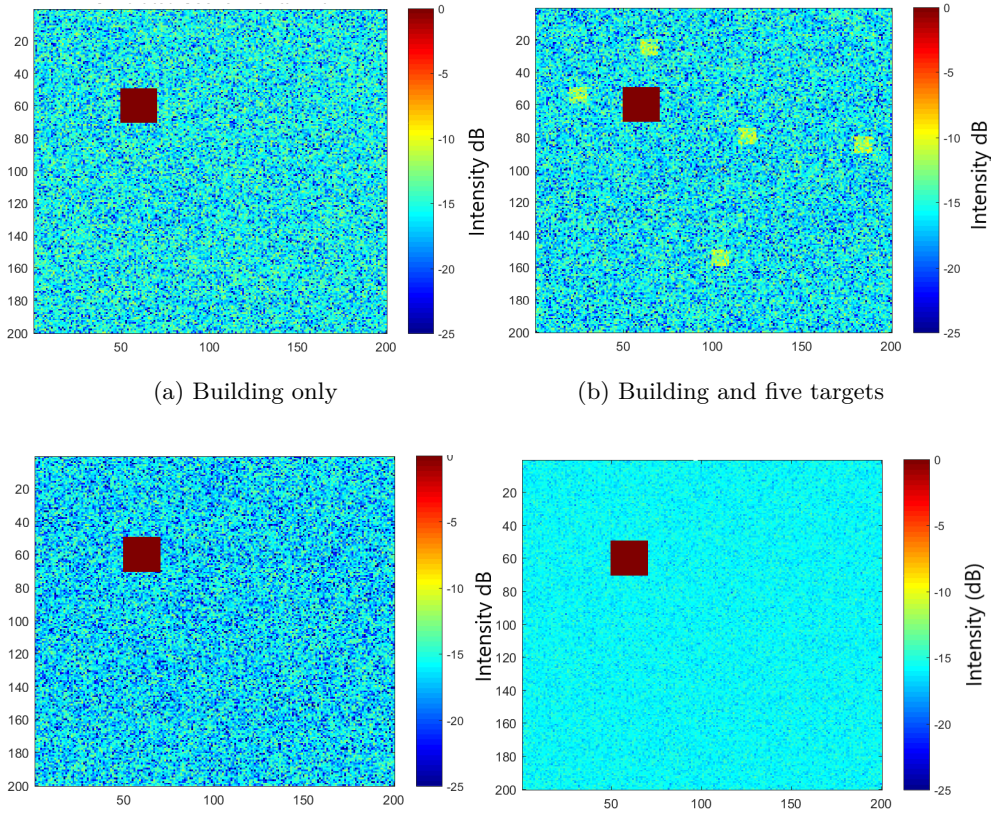


(a) Building only

(b) Building and five targets

(c) FBR Scene (RP)

(d) FBR Scene (MP)

Figure 5.1: Simulated scenes and associated reference images : (a) Building Only, (b) Building and five targets, (c) FBR scene computed with RP method, (d) FBR scene generated using the MP algorithm.

Several target-free scenes with only the static object were generated. An example is shown in Figure 5.1a. The noise is generated as a zero-mean complex Gaussian distribution. From this time series of 10 simulated images, FBR scenes are computed both in RP (Random pixel) and MP (Multi-temporal pixels) modes. Figures 5.1c and 5.1d present the two resulting FBR images.

To estimate the impact of the process on the histogram of FBR images, we computed the

histograms of both FBR images and a target-free image. As we can see in Figure 5.2, histograms of the FBR-RP images and one random target-free scene of the stack have comparable behavior. On the contrary, as expected, the histogram of the FBR-MP image is squeezed because the standard deviation of the noise decreases with a factor $\sqrt{D'}$, with $D'$ being the number of remaining dates. This difference of statistics will have to be taken into account while designing the change detection strategy. Since the FBR-RP and a given radiometric image of the time-series follows the same a priori statistic, a change detection can be applicable directly. Considering the change detection between a radiometric image and the FBR-MP image, it is less intuitive at first sight so some solutions will have to be implemented.

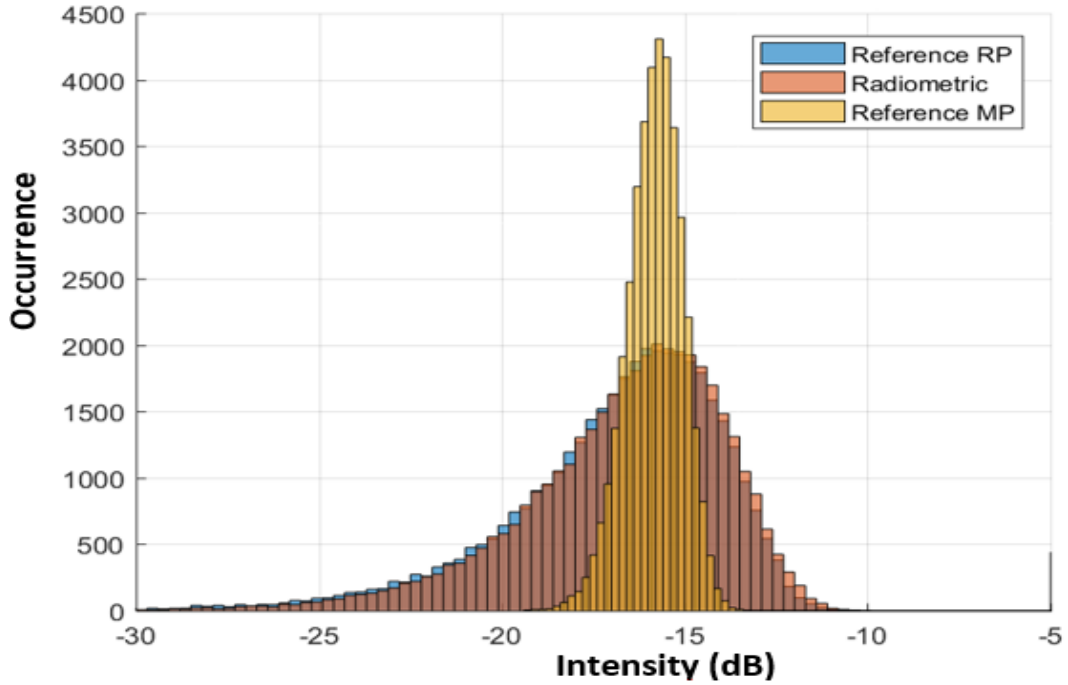


Figure 5.2: Histogram of the intensity for a single image (red), FBR-MP image (yellow) and FBR-RP images (blue).

## 5.2 Illustration of the algorithm

In this section, we illustrate in high attendance areas such as mooring quays in industrial harbors the outcome of the algorithm of stable pixels selection using the same specific pixel as in the previous study. We will use the examples presented in section 4.2.1 with first the study of the Sentinel 1 GRD dataset above Singapore and secondly the UAVSAR dataset above San Francisco region.

### 5.2.1 Singapore Sentinel 1 GRD acquisitions

As we can observe figure 5.3, for the static scatterer and the sea surface, the whole time-series has been kept, whereas for the pixel adjacent to the mooring quay 40 iterations were necessary to reach the criterion due to the high number of ships appearance. The selection is performed as presented only in the temporal domain for a given range and azimuth.

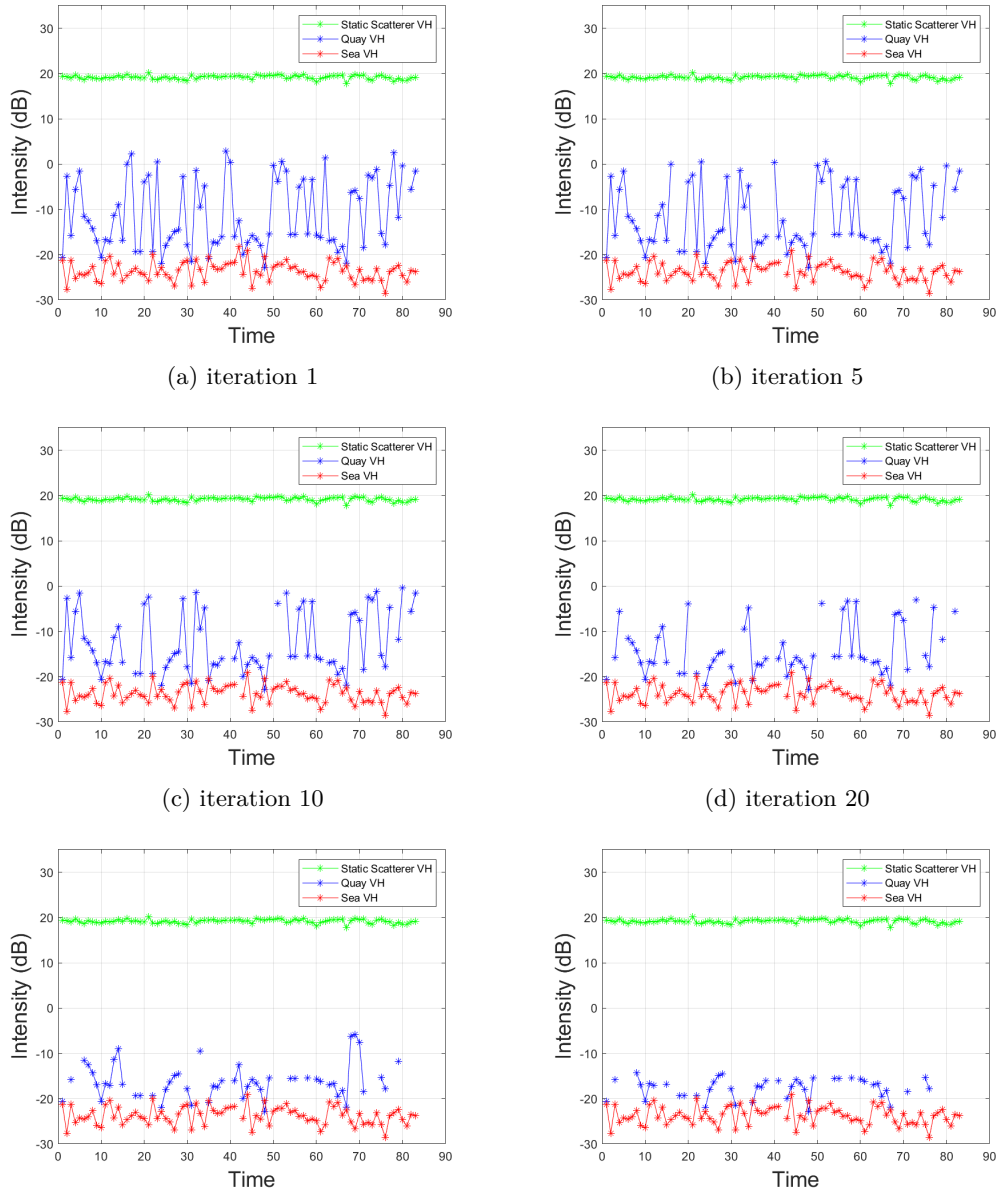


(a) iteration 1

(b) iteration 5

(c) iteration 10

(d) iteration 20

(e) iteration 30

(f) iteration 40

Figure 5.3: Illustration of the selection of candidate pixels for the situation presented in 4.2.1 (Singapore Industrial Harbour with Sentinel 1 GRD data) for iteration 1, 5, 10, 20, 30 and 40 (respectively a, b, c, d, e and f)

### 5.2.2 San Francisco Region UAVSAR

Following the same principle, we show the iterative process to select the candidate pixels for the San Francisco case. Results are presented in figure 5.4 For the static scatterer, the whole time-series have been kept, but for the see surface, some pixels have been extracted as we could see from the CV experimental study, indeed the calculated CV for the sea pixels were above the theoretical threshold.

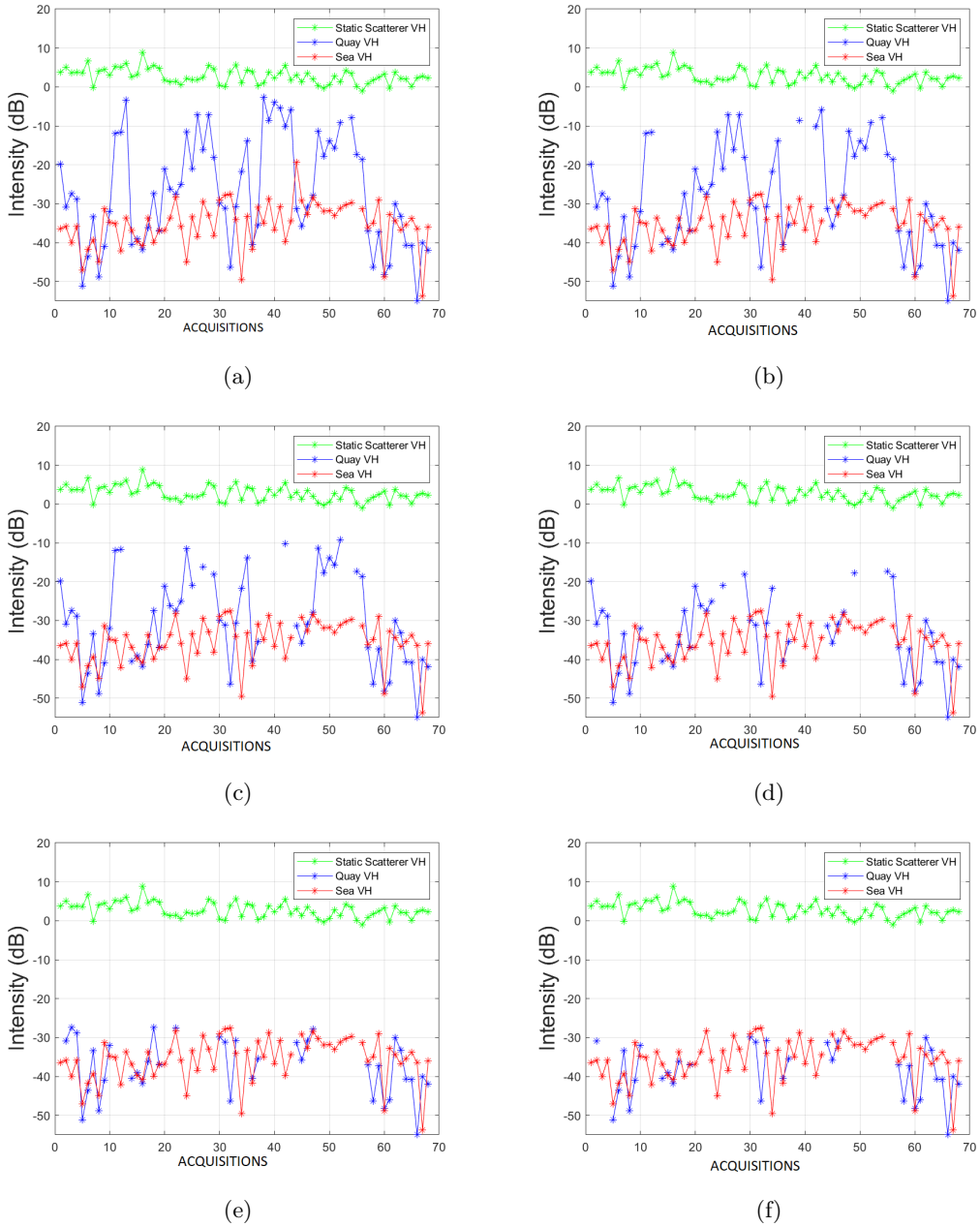


Figure 5.4: Illustration of the selection of the candidate pixels for the situation presented in 4.2.2 (San Francisco region Industrial Harbour with UAVSAR data) for iteration 1, 5, 10, 20, 30, 35 (respectively a,b,c,d,e and f)

### 5.2.3 Discussion

This experimental study on the outcome of the algorithm for different specific points shows some interesting insight on the properties of the CV. It enables to generate a set of pixels corresponding to an homogeneous background both for high backscattering signals as well as region with week backscattering signal. The contributions from the ships have been successfully removed and a temporal homogeneous behavior is obtained for each specific pixel of interests in the two configurations of acquisition. We will then investigate the behavior of the FBR image computed using all the remaining pixels (MP) by considering different number of acquisitionss to compute it.

## 5.3 How many acquisitions are required to produce an "acceptable" FBR image ?

It is theoretically challenging to give a formal answer to this question because it depends mainly on the activity of the area and the SAR acquisition parameters such as revisit time and frequency. Experimentally, we propose to study the same scenes that have been presented in the previous section to evaluate after how many acquisitions the outcome of the FBR image remains unchanged. We will then focus on the activity zones near moorings quays and evaluate the impact of the number of acquisitions considered to compute the FBR image.

### 5.3.1 Singapore Sentinel C-Band

We propose here to understand in the specific case of Singapore dataset study how many dates would be required to obtain a stable FBR scene.

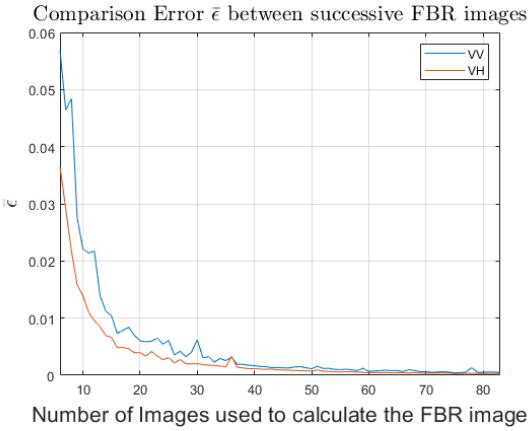


Figure 5.5: Mean error $\bar{\epsilon}$ depending on the number of images used to compute the FBR image.

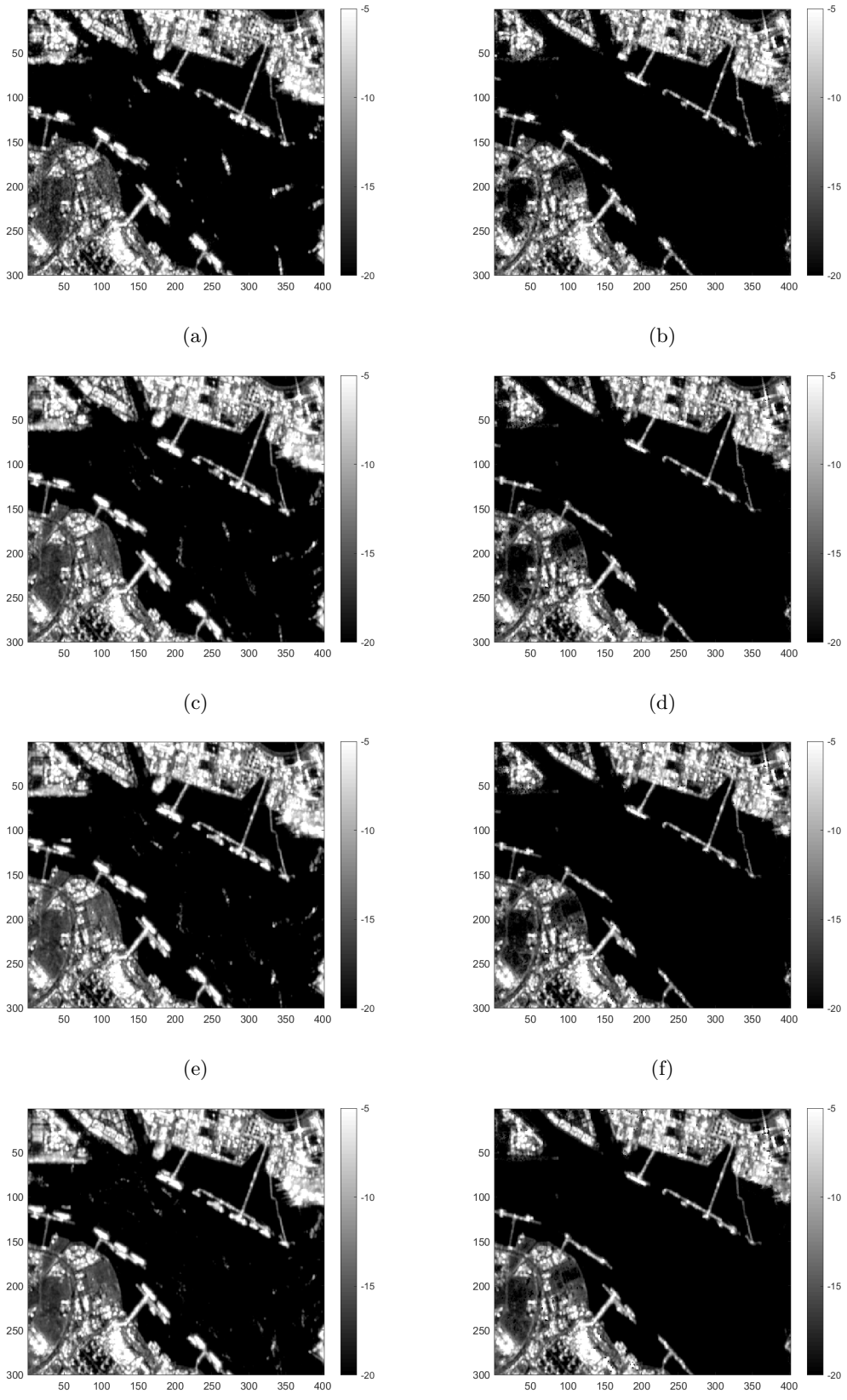


Figure 5.6: Temporal mean Sentinel 1 GRD VH for 5, 20, 30 and 75 images (left column respectively a, c, e, g) and corresponding FBR scene computed with 5, 20, 30 and 75 images (right column respectively b, d, f, h). The representation is for all images the Intensity in dB.

To study the number of images needed in this particular case to consider a stable background, we proposed the generation of 79 FBR images by successively incrementing the number of images on which the FBR image was calculated from 4 to 83. We then proposed to calculate $\gamma_{FBR}$ for the CD (log ratio) between each successive generated FBR image and defined the mean error as $\bar{\epsilon} = \frac{1}{N_{range}N_{az}} \sum_{i=1}^{N_{range}} \sum_{j=1}^{N_{az}} \gamma_{FBR}(i,j)$ with $\bar{\epsilon}$ as the mean error, $N_{range}$ and $N_{az}$ as the number of pixels in range and azimuth, respectively. As we can see from Figure 5.5, after 30 dates used to generate the FBR image, any new image added to compute the FBR image only slightly impacted the resulting FBR image. We compare a temporal mean with the FBR images previously computed considering different numbers of images to illustrate that the activity in the harbor as been well cancelled in high attendance areas such as mooring quays. The figure 5.6 shows on the left column the temporal mean of the SAR images in VH polarisation for 5, 20, 30 and 75 dates of the time series and the right column shows the FBR images computed with the corresponding number of images. As we can observe in figure 5.6a, 5.6c, 5.6e and 5.6g, the temporal mean gives a mixed answer between situation where boat were presents and vacant near mooring quays. On the contrary and as expected from the previous results shown 5.5, with five images, residual signals from boats are still present but vanish after 20 images and become stable and unchanged after 30 acquisitions.

### 5.3.2 San Francisco UAVSAR

We conducted the same study for the UAVSAR dataset presented earlier, in that case, we look as well at the outcome of the FBR images from 5 to 68 computed images. As we can observe the activity near the harbour has been well suppressed for the representation of the FBR image with HH channel as we can see figure 5.4 and remain unchanged after 20 acquisitions.

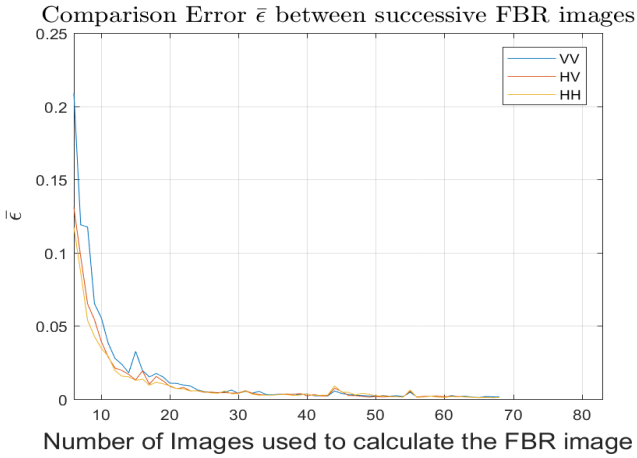


Figure 5.7: Mean error $\bar{\epsilon}$ depending on the number of images used to compute the FBR image.

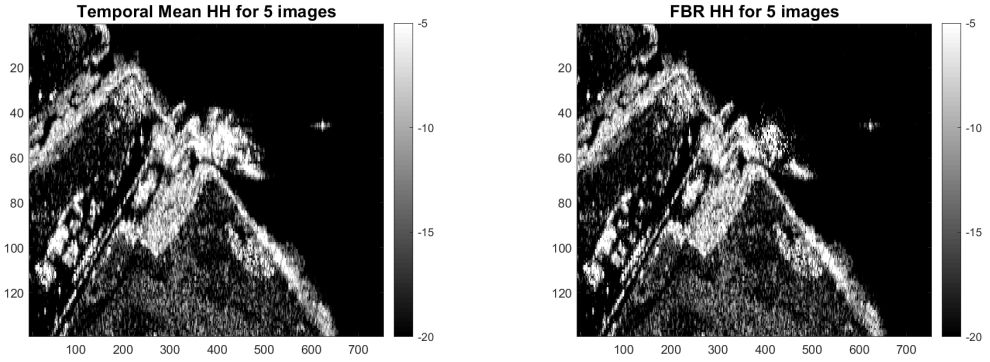


(a) (b)

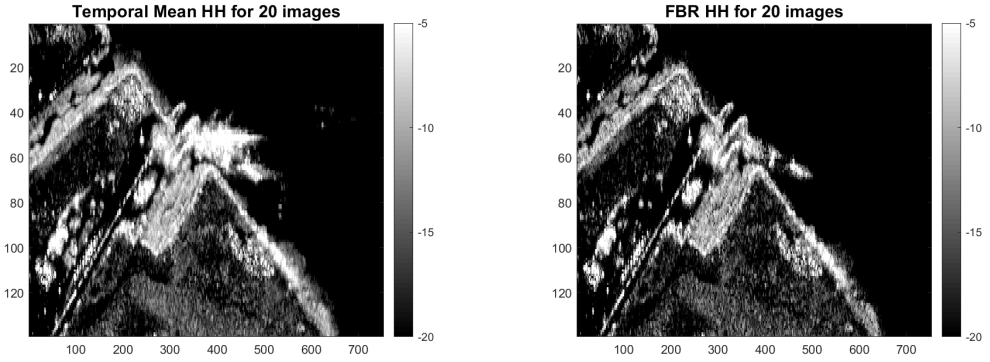


(c) (d)

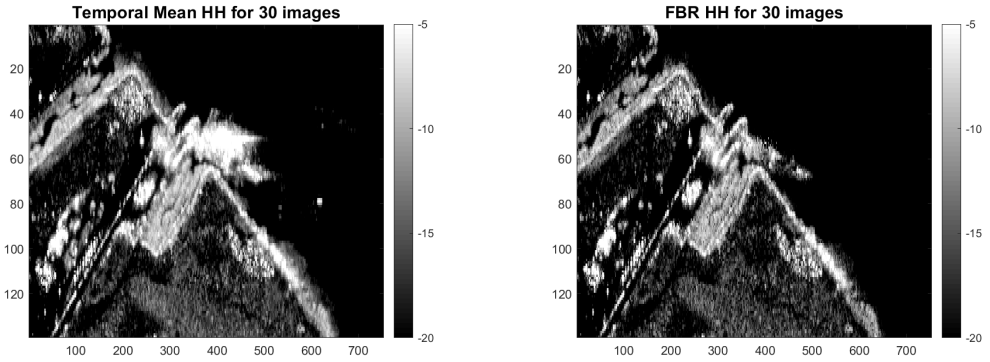


(e) (f)

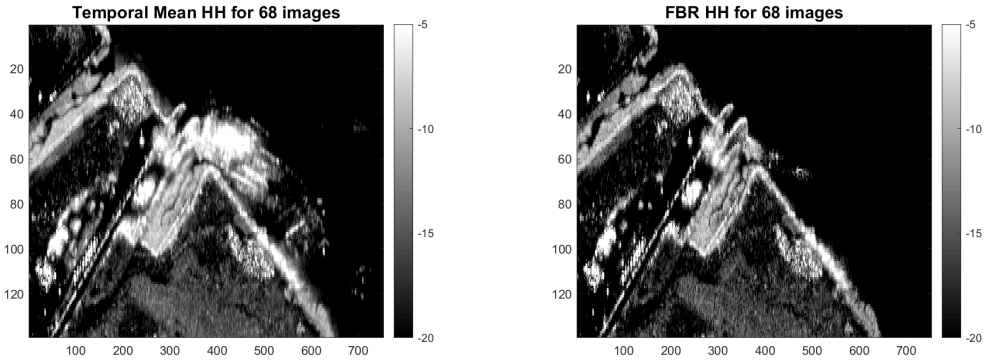


(g) (h)

Figure 5.8: Temporal mean HH for 5, 20, 30 and 68 images UAVSAR (left column respectively a,c,e,g) and corresponding FBR scene HH computed with 5, 20, 30 and 68 images (right column respectively b,d,f,h). Zoom on the harbor activity.

The outcome seems similar for each polarisation as shown in figure 5.7 and reach a stable state of the FBR image with a bit less acquisitions (20 acquisitions) than for the case of Singapore Harbor with Sentinel 1 GRD data. We can notice the same trend in this configuration for each polarisation, the result is interesting, however it is not possible to conclude on a specific number of acquisitions required to perform such FBR image in the general case or for a specific environment.

In practice, as shown here, we might need a lot of acquisitions in regions were the attendance is high such as harbours in industrial environment. In the present case for Sentinel 1 GRD data, it represents around 30 dates so one year of acquisitions. For UAVSAR, the data are not monitored in a periodical way but sporadically over 8 years and represent around 20 acquisitions (2 years). In general, a trade-off has to be chosen between the number of acquisitions (depending on the revisit time of the sensor) and the type of activity we want to observe, indeed the longer the acquisitions time, the higher the probability that a permanent change occurs. In addition, the time at which the satellite is passing is also an important factor that might be taken into account (night, day) because the activity might be also completely different. In this preliminary study, we assumed a stable background and therefore we did not implement an update in case of building construction/destruction. This limit has to be taken into account for the next studies.

## 5.4 Illustration and example of Polarimetric FBR image

The selection process has been presented and illustrated with a few experimental examples to approach the behaviour of the FBR images depending on the number of acquisitions and polarisation in industrial harbour environment. Considering a polarimetric acquisition, we can compute for each range and azimuth a temporal covariance matrix. Denoting $\mathbf{y}$ and $\tilde{\mathbf{y}}^{MP}$ a polarimetric vector at a given range and azimuth in the pauli basis respectively from the initial SAR time-series containing D acquisitions and from the cube of remaining pixels containing D' acquisitions, their temporal samples covariance matrices can be estimated over D and D' samples by computing:

$$\mathbf{T_{temp}} = \frac{1}{D}\sum_{d=1}^{D} \mathbf{y_d} \mathbf{y_d}^H \tag{5.1}$$

$$\mathbf{T_{FBR}^{MP}} = \frac{1}{D'}\sum_{d'=1}^{D'} \tilde{\mathbf{y}}_{d'}^{MP} \tilde{\mathbf{y}}_{d'}^{MP^H} \tag{5.2}$$

To generate the corresponding Pauli images, we take the 3 diagonal terms of $\mathbf{T_{temp}}$ and $\mathbf{T_{FBR}^{MP}}$ that are associated to single bounce, double bounce and volume scattering. We illustrates a result

of polarimetric FBR image computed on the UAVSAR dataset. In this example, the figure 5.9 presents different optical images of the scene from 2011 to 2015 showing the activity in the harbour with different kind of vessels and floating platforms. In comparison we plot the polarimetric temporal image and the FBR image in Pauli representation with R=double bounce, G=Cross polarisation contribution and B=single scattering mechanisms. As we can see and we observed in the previous part, the activity near the harbour has been canceled in the Pauli FBR image whereas for the temporal Pauli representation we obtain naturally the mean behaviour of all activities.

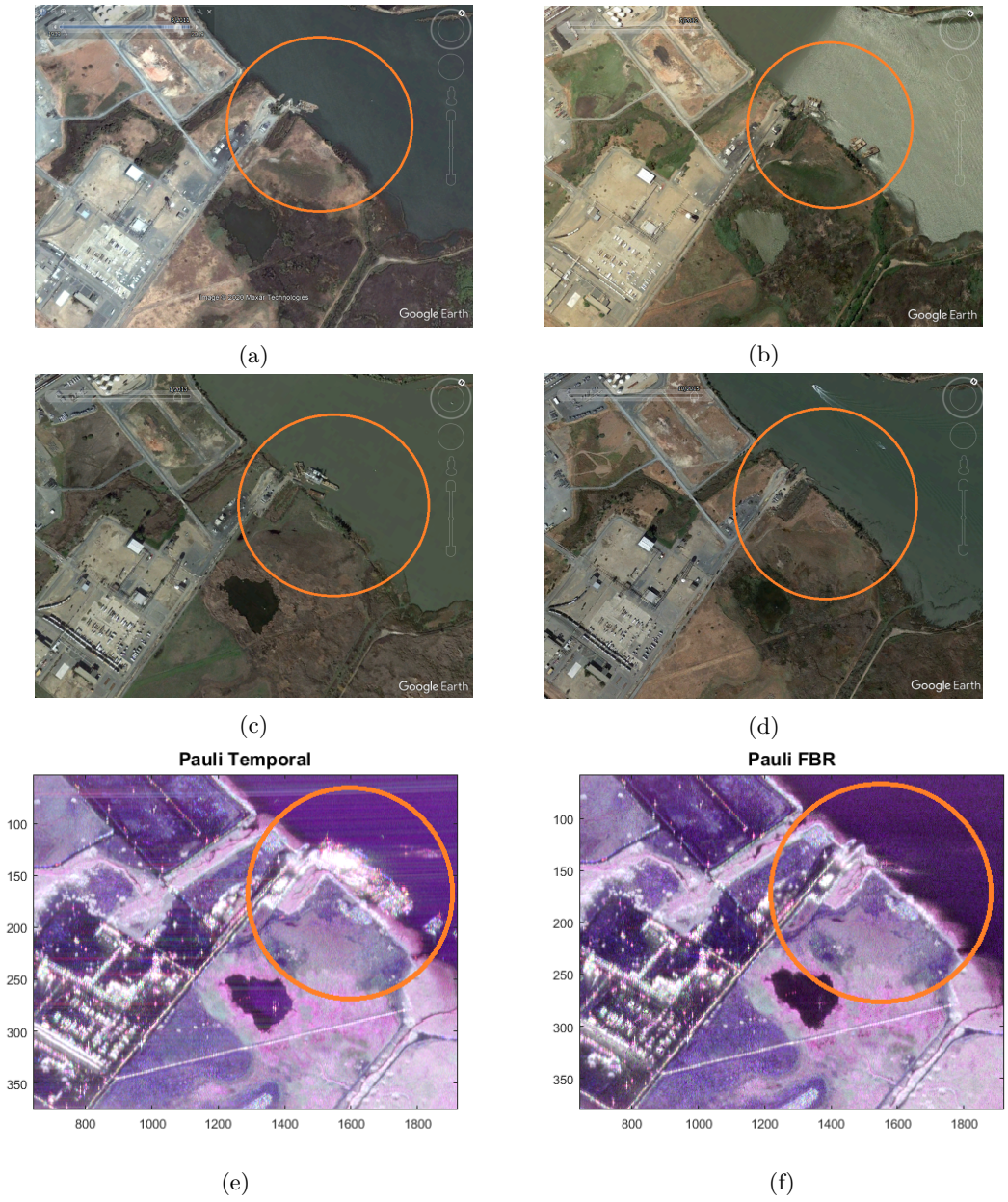


Figure 5.9: Example of Google Earth Images from the scene (a) 08 November 2011, (b) 05 November 2012, (c) 01 January 2013, (d) 10 November 2015, (e) UAVSAR Temporal Pauli 68 Dates and (f) UAVSAR FBR Pauli 68 dates (R:Double Bounce, G:Cross Polarisation, B: Single Bounce, scale of the image for each polarisation [-35 -5 dB])

We can as well observe that the interferences present in the temporal representation in Pauli basis are suppressed in the FBR polarimetric image. However, further studies need to be conducted to verify for instance the validity of the polarimetric phases, as the copolarisation phase difference and crosspol phase difference. This assumption has to be verified in the future to understand better the behaviour of the CV in a polarimetric dataset computed in parallel.

## 5.5 Discussion

According to these experimental studies, it seems possible to obtain a background image of the scene and discard ephemeral objects or events using SAR time-series. The chosen regions represent two industrial areas where we focused mainly on the harbor activity since it is much easier to monitor and verify the activity visually. However, it is not straightforward to measure the degree of validity of each computed FBR images since we cannot compare it with any real image. A dedicated long SAR time-series with a precise ground truth may be essential to consider to evaluate more properly the behavior of the proposed framework for the computation of a background scene.

**Summary** : In this chapter we have presented the concept of FBR image and its computation using an iterative temporal variation coefficient process. We aimed with this pragmatic approach to select within the time-series a set of pixels that are temporally homogeneous taking into account the intrinsic statistical characteristics of SAR images. Simulations and experimental results have been presented to illustrate our method. An experimental study has been performed on the impact of the number of acquisitions needed to obtain a FBR image so that additionnal images do not affect anymore the results in the context of industrial harbor areas.

# Chapter 6

# Change Detection Strategies

**Objectives** : In this chapter we propose to analyse and adapt the statistical tests under Gaussian assumption taking into account that a set of stable pixels has been collected for each range and azimuth from a monopolarisation or polarimetric SAR time-series. We consider that this set of stable pixels has been selected either using our method based on the variation coefficient or from any other method. We will therefore present the associated tests for the possible representations of the FBR image discussed in the previous chapter: a temporal random selection of the remaning pixels or the consideration of the whole remaining candidate pixels. We will consider the general case of polarimetric data that can be always brought back to the form of mono polarised data.

We have presented different representations of the FBR image, therefore different strategies of change detection are presented and the statistical tests adapted. For both strategies, RP and MP selection, we can consider that the interpretation will be improved because we will compare a scene a priori without ephemeral targets with an acquisition with possibly ephemeral targets. We can expect intuitively that the FBR image selected with the RP method will not affect the targets probability of detection compared to a usual case of bi-date change detection when one image is without target and another is with target. On the contrary, using several acquisitions improves the knowledge on the background so that we might expect better detection considering the whole set of temporally homogeneous pixels for the detection.

## 6.1 Random Pixels

We focus first on the case where we choose to select a random pixel from the list of temporal stable candidate pixels for each azimuth and range of the image. We obtained, therefore, one polarimetric FBR measurement vector $\tilde{\mathbf{x}}^{RP}$ of dimension p at a given range and azimuth. Assuming that the statistics of speckle remained unchanged, in the space domain (range, azimuth) as well as in the time domain, we can adapt the different tests introduced in [59]. For bi-temporal change detection, we assume that a polarimetric pixels vector $\tilde{\mathbf{x}}^{RP}$ of the FBR Image and a polarimetric pixels vector $\mathbf{y}$ from the Mission Image follow a multivariate zero-mean complex Gaussian distribution with $\boldsymbol{C}_{\boldsymbol{FBR}}^{\boldsymbol{RP}}$ and $\boldsymbol{C}_{\boldsymbol{mi}}$ as the sample covariance matrices associated to vectors $\tilde{\mathbf{x}}^{RP}$ and $\mathbf{y}$ [59]. The test to be computed and compared with a threshold and can be written using the following equation:

$$\gamma_{RP} = \frac{|\boldsymbol{C}_{\boldsymbol{FBR}}^{\boldsymbol{RP}}|^N |\boldsymbol{C}_{\boldsymbol{mi}}|^N}{|\frac{1}{2}(\boldsymbol{C}_{\boldsymbol{FBR}}^{\boldsymbol{RP}} + \boldsymbol{C}_{\boldsymbol{mi}})|^{2N}} \tag{6.1}$$

where $N = N_{FBR} = N_{mi}$ is the number of samples within the spatial averaging box to compute the covariance matrix, and $||$ represents the determinant of the matrix.

## 6.2 Multi-temporal pixels

If we consider a pixel at a given range and azimuth, we can gather $N_{FBR}$ homogeneous observations of the vector $\tilde{\mathbf{x}}^{MP}$ with $N_{FBR}$ the number of spatio-temporal pixels within the cube of remaining pixels as presented in Figure 6.1. For the mission image, we suppose $N$ spatial observations of the vector $\mathbf{y}$ within a spatial box of N elements. We suppose that the samples of these two vectors of dimension p follow a complex Gaussian distribution and are IID (idenpendant and identically distributed).

Testing the equality of their respective covariance matrices $\boldsymbol{C}_{\boldsymbol{FBR}}^{\boldsymbol{MP}}$ and $\boldsymbol{C}_{\boldsymbol{mi}}$ corresponds to the test derived in [45] by testing the equality of two p × p Wishart matrices $\mathbf{X}_{\mathbf{FBR}} = N_{FBR}\boldsymbol{C}_{\boldsymbol{FBR}}^{\boldsymbol{MP}}$ and $\mathbf{X}_{\mathbf{mi}} = N\boldsymbol{C}_{\boldsymbol{mi}}$.

$$\gamma_{MP} = \frac{(N_{FBR}+N)^{p(N_{FBR}+N)}}{N_{FBR}^{pN_{FBR}} N^{pN}} \frac{|\boldsymbol{X}_{\boldsymbol{FBR}}|^{N_{FBR}} |\mathbf{X}_{\mathbf{mi}}|^N}{|\boldsymbol{X}_{\boldsymbol{FBR}} + \boldsymbol{X}_{\boldsymbol{mi}})|^{(N_{FBR}+N)}}. \tag{6.2}$$

This test can be rearanged to make appear the sample covariance matrices :

$$\gamma_{MP} = \frac{|\boldsymbol{C}_{\boldsymbol{FBR}}^{\boldsymbol{MP}}|^{N_{FBR}} |\boldsymbol{C}_{\boldsymbol{mi}}|^N}{\left|\frac{N_{FBR}}{N_{FBR}+N}\boldsymbol{C}_{\boldsymbol{FBR}}^{\boldsymbol{MP}} + \frac{N}{N_{FBR}+N}\boldsymbol{C}_{\boldsymbol{mi}})\right|^{(N_{FBR}+N)}}. \tag{6.3}$$

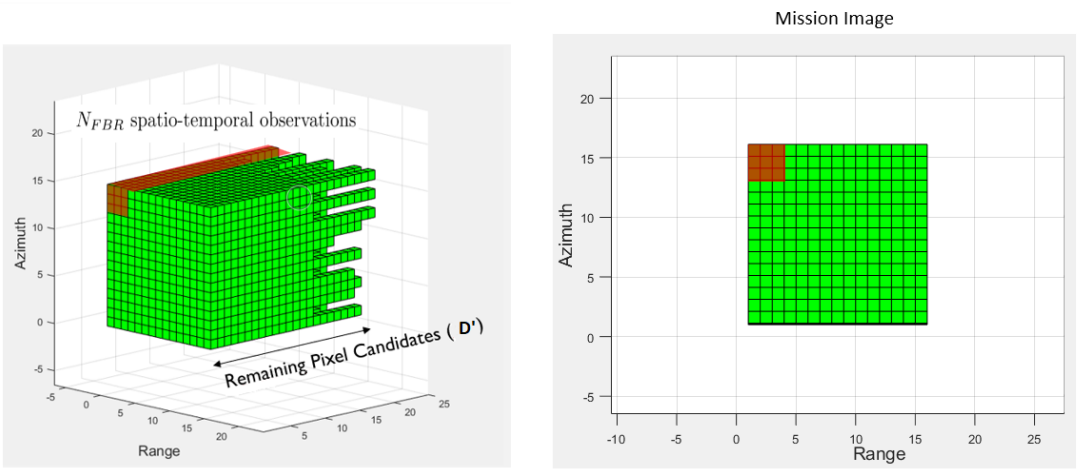


(a) (b)

Figure 6.1: Pixel representation for CD between FBR image (a) and Mission Image (b)

Taking advantage of several homogeneous acquisitions to perform change detection improves the probability of detection as it has been shown by simulation in [59]. In practice, it is difficult to know the optimum number of acquisitions and spatial averaging window necessary to achieve a good detection because it depends mainly on the context. Indeed, increasing spatially the averaging window of N elements would increase the possibility to mix pixels from heterogeneous areas and decrease as well the resolution of the detection. Using temporally stable pixels over a long period may have a different impact depending on the frequency of acquisition and the observed scene and may require a dedicated study.

## 6.3 Simulations

We will now present the behavior of the change detection in different mode of the FBR images compared with usual bi-date change detection as $\gamma_G$ from equation 3.5. The Table 6.1 presents the different settings used to evaluate the CD results in paragraph Sections 6.3.1 and 6.3.2.

### 6.3.1 Impact of target SNR

First, a set of 10 images was created. We aimed to evaluate the behavior of the detection approaches for different target SNRs. The raw output of change detection for the worst case of target SNR is presented in Figure 6.2, and the associated ROC (Receiver operating characteristic) curves for different configurations of the target SNR are plotted in Figure 6.3. The PD (detection probability) and PFA (probability of false alarm) are defined as follows: $PD = \frac{TP}{NT}$ and $PFA = \frac{FP}{NB}$ with TP as the number of pixels truly detected as a target, $NT$ as the number of ground truth pixels defined

Table 6.1: Simulation settings : with SNR (Signal-to-Noise ratio), RP (Random pixel), MP (Multi-temporal pxiels).

| **Simulation Parameters** | **Section** 6.3.1 | **Section** 6.3.2 |
|---|---|---|
| Image Number | 10 | 1, 3, 6, 9, 15, 20 |
| Images size | 200 × 200 pixels | 200 × 200 pixels |
| Building size | 20 × 20 pixels | 20 × 20 pixels |
| Targets size | 10 × 10 pixels | 10 × 10 pixels |
| SNR building | 13 dB | 13 dB |
| SNR targets | 3, 6, 13 dB | 6 dB |
| Algorithms | Bi-date, RP, MP | Bi-date, RP, MP |

as a target, $FP$ as the number of pixels falsely detected as a target, and $NB$ as the number of pixels defined as background pixels.

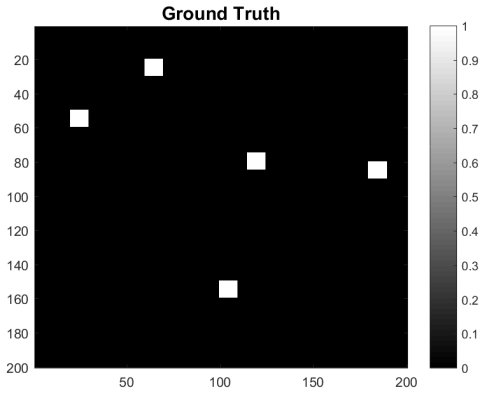


(a) Ground Truth

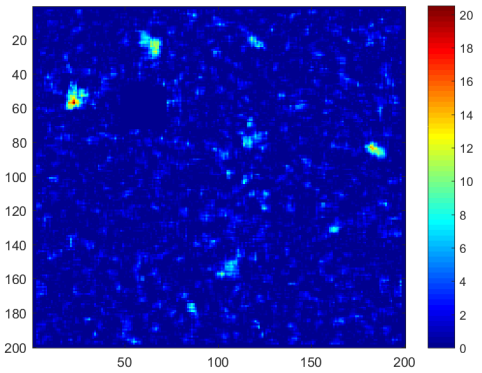

(b) CD bi-date $\gamma_G$

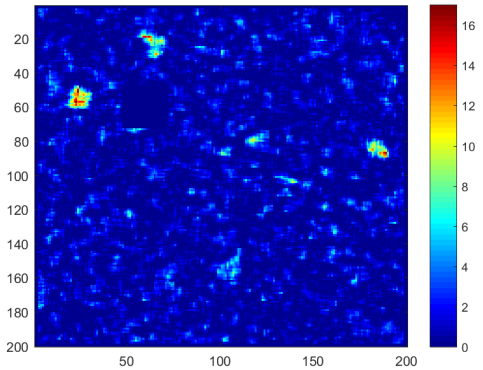

(c) CD RP $\gamma_{RP}$

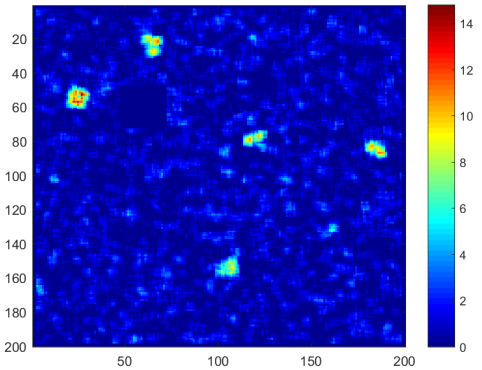

(d) CD MP $\gamma_{MP}$

Figure 6.2: Example of the CD ground truth and change map for SNR = 3 dB.

As we can see in figure 6.3, the CD from RP computation of the FBR image gives a similar

detection capability than the classical bi-date detection.

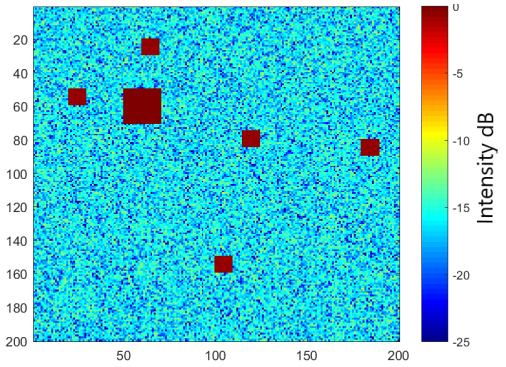


(a) Scene with SNR = 13 dB

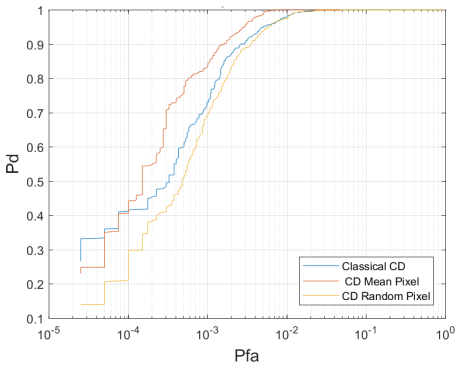


(b) ROC SNR = 13 dB

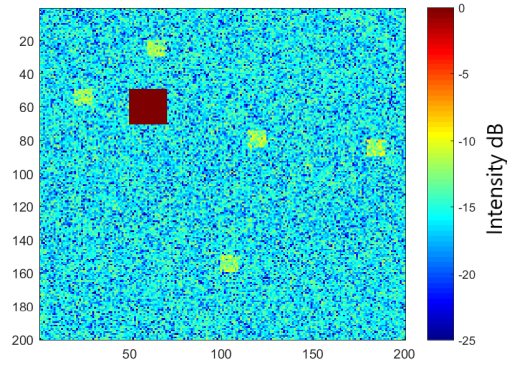


(c) Scene SNR = 6 dB

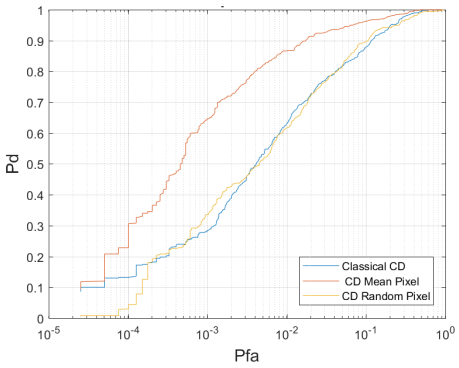


(d) ROC SNR = 6 dB

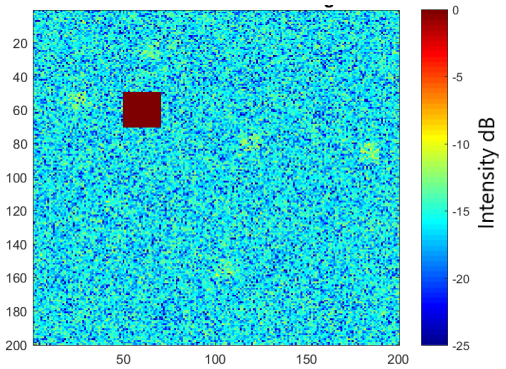


(e) Scene SNR = 3 dB

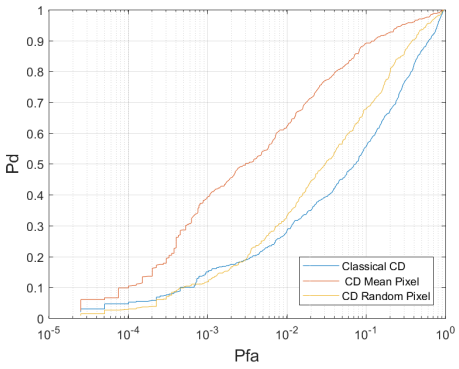


(f) ROC SNR = 3 dB

Figure 6.3: ROC (Receiver Operating Characteristic) curves representing PD (probality of detection) and PFA (probabiblity of false alarm) for different targets SNR (Singal to Noise Ratio)

Using the MP computation for the reference gives much more improvement on change detection, especially when target SNR is low, as we can see on graphics 6.3f and 6.3d. At a fixed PFA = $10^{-3}$, we can observe the associated probability of detection in different cases. When the SNR is sufficiently high (13 dB), results are in the same range of PD for the three different detectors: 0.75 for Bidate CD and $\gamma_{RP}$ and slightly higher for $\gamma_{MP}$ with 0.85. In the case of a lower SNR

of 6 dB, the detection performances of CD-bidate and $\gamma_{RP}$ decreased drastically to 0.3, on the contrary, $\gamma_{MP}$ still gave a good PD of 0.7. Finally, in the case of a low SNR = 3 dB, The PD of the CD-bidate and $\gamma_{RP}$ decreased to 0.15. The probability of detection of $\gamma_{MP}$ was still higher but remained a poor detection probability of 0.4. The result is particularly of interest for targets hidden in high clutter, for example, in FoPen applications or urban areas. In the following part, we simulated targets with a fixed SNR. The CD output will be investigated for different numbers of images within the time series using the MP method.

### 6.3.2 Impact of number of available dates

In order to evaluate the benefit of using several pixels to construct the FBR scenes and the impact on the change detection, several change maps have been produced using the simulated ground truth with different amounts of images randomly chosen from the simulated SAR stack. The results are shown in Figures 6.4a and 6.4b. We can observe that the detection is improved when increasing the number of dates taken as a reference.

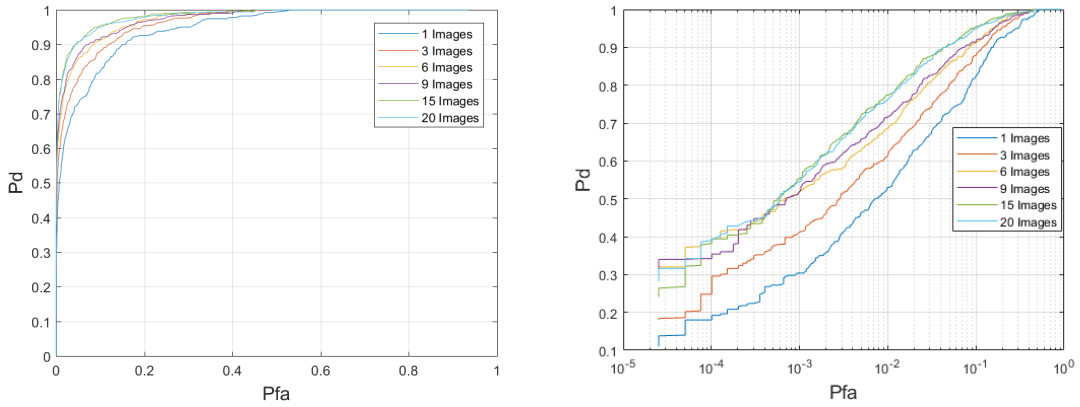


(a) ROC curve linear PFA

(b) ROC curve (semilog)

Figure 6.4: ROC (Receiver Operating Characteristic) curves representing PD (probality of detection) and PFA (probabiblity of false alarm) for different amounts of images used to create the FBR scene (SNR=6dB).

## 6.4 Discussion

From this simulation study, we can conclude on different aspects of the method. First, the choice of a random pixel RP within the candidate pixels from simulation gave comparable results to a typical bi-date detection. Considering the use of all remaining candidate pixels through the MP method, we can see that the detection capability is drastically better when the target SNR was decreasing. This property is a promising result for the detection of targets hidden in a high clutter environment.

In this example, we focused on the interest of using homogeneous temporal pixels to improve the change detection capabilities. However, in practice, it is difficult to know how much acquisitions are necessary to achieve a good detection since it depends both on the environment and the properties of the object to detect.

**Summary** :

In this chapter, we investigated some strategies of change detection, given the two possible configurations of selection: random selection of pixels within the list or the contribution of all remaining pixels. We could observe that using a random selection of the remaining pixels gives the same detection capabilities than with a usual bi-date case when a target-free scene is available, and one mission image is tested to highlight possible targets. With these simulations, we could observe the interesting detection capabilities improvement when using several acquisitions to compute the change detection test with the mission image containing targets.

**Summary of part II** :

In this part, we first investigated the possibility of computing a scene free of ephemeral objects using several acquisitions. We introduced its computation and some illustrations on harbor environments where it was easier to verify the result visually. We could see that it was possible to compute target-free scenes using several acquisitions in harbors environment at C-band with Sentinel 1 GRD dataset and L-band with UAVSAR sensor. This framework of FBR procedure can be used in different scenarios when the aim is to detect ephemeral objects in SAR time series. For the change detection, we showed using simulation that we can improve the capabilities of detection by using all the remaining selected pixels. However, this method supposes that it exists a stable behavior of the background (modulated with the noise) and ephemeral objects sporadically appear and disappear within the time. With the periodicity of sensors such as Sentinel (12 days for a single Satellite), it is an opportunity to have an estimation of the stable background of a scene and follow the possible variations according to this stable behavior. For this study, we considered a scene without a permanent change in the structural background (demolition of a building or construction of a building).

# Part III

# APPLICATION OF FBR CHANGE DETECTION IN SAR TIME-SERIES

# Chapter 7

# Maritime Surveillance

**Objectives** : In this chapter, we illustrate a possible application of the FBR procedure in maritime surveillance, particularly in harbor areas. The detection of ships in the open sea is usually performed with single SAR images because the contrast between the sea background and a possible vessel is quite strong in practice. In harbor areas, several scatterers such as mooring quays, permanent platforms, or more generally harbor infrastructures, might produce strong backscattering signals. It renders the detection of vessels with only one image more challenging and produces false alarms. The FBR framework might be an interesting alternative in harbor environments to detect moored ships in high attendance areas. First, we illustrate the FBR CD for maritime platforms with UAVSAR L-band dataset in a calm, open sea area. In a second time, we present the results of the FBR CD in harbor environment with Sentinel 1 GRD dataset previously introduced.

Maritime surveillance is a topic of interest for governments and institutions for safety and security concerns. Remote sensing is an asset to monitor and understand ship behaviors, potential illegal border crossing and illegal fishing activities. It is also an opportunity to optimize the use of the maritime space [14]. Traffic monitoring can besides offer indications on the activity in harbor areas and therefore clues about the economic health of a region.

Industrial harbors are a challenging environment for ship detection using SAR monitoring. Firstly because of the possibly high number of ships within the same area and secondly because of the harbor infrastructures that might generate several false alarms since they are, in general, strong scatterers (metallic structures or mooring quays). To avoid this issue, usual algorithms of ship detection consider a land masking with a buffer of several hundred of meters [85, 14]. Change

Detection is an interesting alternative to overcome this issue by canceling the contributions of infrastructures and highlighting the presence/departure of ships within harbor areas.
As discussed in chapter 3, the usual change detection framework in SAR time-series is designed to detect relative changes. The consecutive temporal occurrence of different ships within the same spatial pixel might cause detection misinterpretations when a sequential detection approach is carried out. It seems then more comfortable to compare an acquisition with an image without non-stationary targets (only immobile objects). Considering the proposed FBR framework, we aim to compute first the stable background of the harbor (infrastructures and sea clutter) and afterward perform change detection from this FBR image to highlight the presence of ships. This chapter will first introduce the maritime surveillance specificity and the challenging aspect of the harbor environment using SAR imaging systems. Afterward, a simple scene with boats (floating platforms) only on the open sea will be studied to illustrate the FBR CD. Finally, a more complex scenario will be investigated in high attendance harbor environment in Singapore using Sentinel 1 GRD dataset presented earlier.

## 7.1 Specificity of maritime surveillance using SAR imaging

SAR sensors showed great potential for maritime surveillance applications due to their capability to obtain images in any weather conditions (depending however on the frequency) and independently of the light condition (day or night). This consideration brings SAR sensors as the most used remote sensing technology to monitor maritime activity. A general framework for ship detection can be synthesized in three main blocks as presented in Figure 7.1.

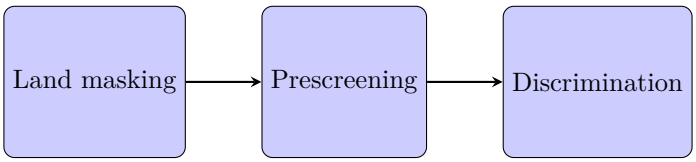


Figure 7.1: Framework for maritime surveillance using SAR imaging

Land masking consists of excluding the pixels that belong to the land. Prescreening is considered as a first detection step to select potential vessels within the scene. Finally, discrimination is the last decision rebutting or confirming if this potential target is indeed a ship. Therefore, a potential alternative is to use the FBR method in the prescreening step with a specific interest in the harbor environment. This section will introduce land masking and prescreening, and only briefly discussed discrimination.

- **Land Masking :**

  According to the literature on maritime surveillance, land masking is a critical step that is still thoroughly studied due to the inherent geolocalization uncertainties, shoreline database uncertainties, and need to be sometimes readjusted manually [85, 86, 87, 14]. In Figure 7.2, we can see a land mask generated on a Sentinel 1A image with two different methods, on the left using a geolocation grid and on the right with restituted orbit data.

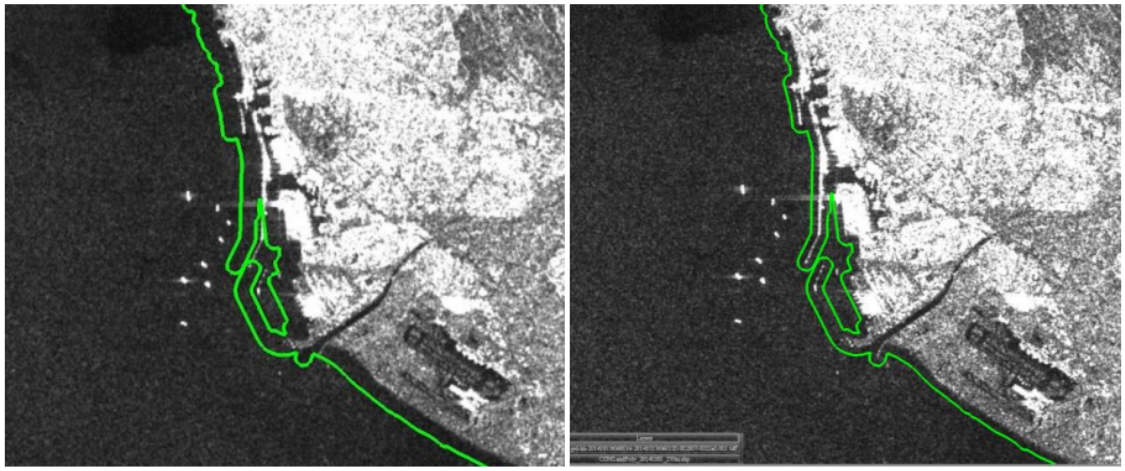

Figure 7.2: Example of land masking from [14], (left) using geolocation and (right) restituted orbit data

One drawback of geographic information based land masking is that small islands or rocks are not always registered so that these pixels will not be excluded from the studied SAR images. More recent approaches propose automatic segmentation based methods [88] to extract land masks. Therefore, land masking is essential to assess a low probability of false alarm coming from lands independently to the type of method for ship detection. From the literature, the buffer zone is usually chosen from 250m to several kilometers, considering the possible geolocation uncertainties. In [89], is presented a method of land masking considering a DEM (Digital Elevation Model) using SRTM (Shuttle Radar Topography Mission, resolution around 90m). The land masking step is, as we can understand, essential to exclude a priori all pixels that might represent non-maritime pixels. In most cases, harbors are excluded from the detection since they can be considered a mix between sea and land environments.

- **Prescreening and discrimination (detection):**

  Prescreening can be seen as a coarse detection and discrimination as a fine detection that will rebut or confirm the coarse detection. In general, CFAR detectors will be used by statistically modeling the background, and pixels with a low probability of belonging to the background will be detected as target pixels.

  Different statistical models of background (Gaussian, Gamma, exponential or K distributions) can be chosen depending on the frequency, resolution, and the zone of observations. Other detectors based on GLRT define a model both for background and the ships (mostly modelling the double bounce between a metallic parallelepiped structure and the sea) such as in [89].

  Detection based on spectral analysis of SAR images sublooks has been derived in [90, 91] using interferometry and cross-correlation, in [92] using entropy, and finally in [93] using GLRT for coherent targets. However, sub-look spectral analysis requires to have an initial SAR image with a sufficient spatial resolution to enable sub-looking without any resolution loss that would prevent to detect small ships.

  The discrimination step comes afterward with more contextual information to exclude possible false alarms coming from side-lobes of strong scatterers, sea wakes, or other perturbations present in a maritime environment. Geometrical information (for example, fractal dimension [94]) is at this stage extracted from the targets to decide whether or not it is indeed a target of interest.

Several phenomenons render the detection with usual methods complicated or not applicable in harbor environments. The role of harbor infrastructures has been discussed briefly as a substantial limitation of typical ship detectors. With harbor infrastructures come the phenomenon of azimuth ambiguities that present problems for maritime surveillance near coastal areas. It generates ghosts signature over the sea that can be as well interpreted as a ship. This phenomenon is an artifact due to the aliasing of the Doppler phase history, as described in [95]. These artifacts are more visible in low backscattering areas such as sea surface.

Using a FBR image would eliminate this problem since azimuth ambiguities are constant signature because coming from a permanent scatterer. The pragmatic approach that we propose could be a good alternative to overcome several issues encountered in harbor environments for ship detection using SAR images.

## 7.2 FBR procedure for maritime surveillance

In this section, we present two applications of FBR-CD on SAR time-series. First we illustrate the results on a calm lake in the area of San Francisco where floating platforms are present without any infrastructures. In a second time, we illustrate different aspects of FBR-CD in a complex environment such as harbour area in the region of Singapore.

### 7.2.1 Floating Platforms over a lake in the area of San Francisco

This example focuses on floating platforms over sea surfaces that can have different configurations, as shown in Figure 7.3. The characteristics of the images used for the study are presented in Table 2.2.

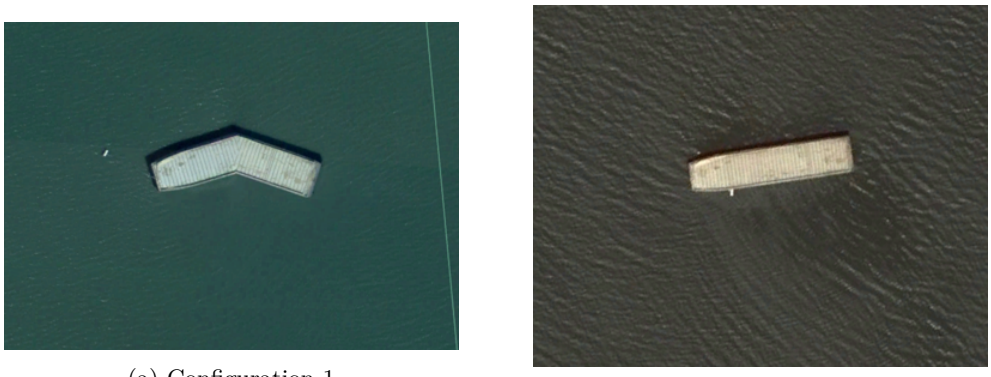

(a) Configuration 1

(b) Configuration 2

Figure 7.3: Example of floating platforms over this lake, seen on Google Earth images.

The scene under study comprises the 12 firsts L-band fully polarimetric UAVSAR (Uninhabited Aerial Vehicle Synthetic Aperture Radar) from the dataset presented in chapter 2 in the region of San Francisco. Figure 7.4a is the first radiometric HH image of the temporal stack, and Figures 7.7b and c are the FBR images obtained from our method using the RP and MP methods. The images are represented in gray levels from $-30$ to 0 dB.

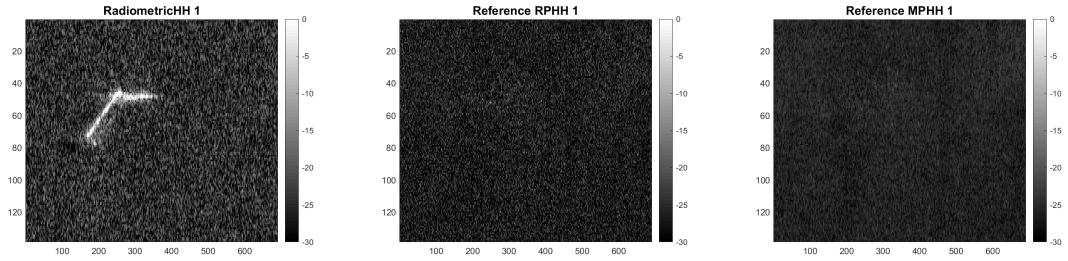


(a) Radiometric 1 HH (b) FBR-RP (c) FBR-MP

Figure 7.4: Radiometric UAVSAR image and MP and RP reference images.

As we can observe in the FBR images in Figure 7.4b and 7.4c, the targets were successfully removed. Figure 7.5a presents the results of the usual change detection between two dates of the stack. Red values on the image indicate that a significant amplitude change occurred, whereas blue areas reflect areas with no changes.

Floating platforms were present at both dates, but not precisely at the same position; thus, the resulting image was difficult to interpret. In Figure 7.5b–e, we plotted the results of change detection from the FBR images in RP and MP modes and the two dates that were used previously for the classical bi-date change detection. In both results, we can directly see a better quality for the image, and it is possible to identify the targets present at each date more accurately . In that case, the SNR (more precisely Target to clutter ratio) of the boat was high; therefore, the results in RP and MP modes were similar as they are presented in a high SNR target simulation. This example shows that it is possible to use this method in target detection, especially when it is necessary to know the number of targets present on one image without prior knowledge of the scene.

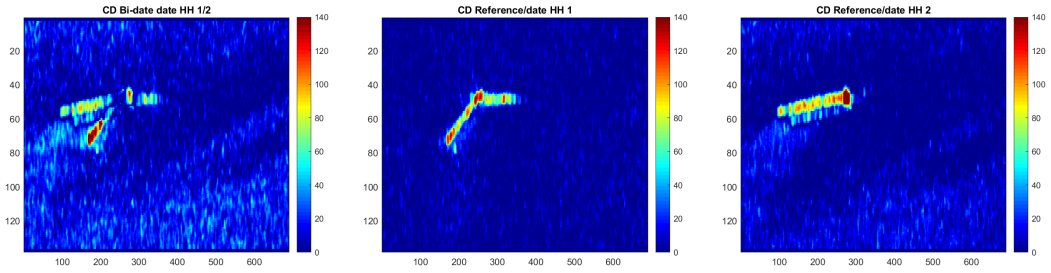


(a) CD Bi-date 1 and 2 (b) CD RP date 1 (c) CD RP date 2

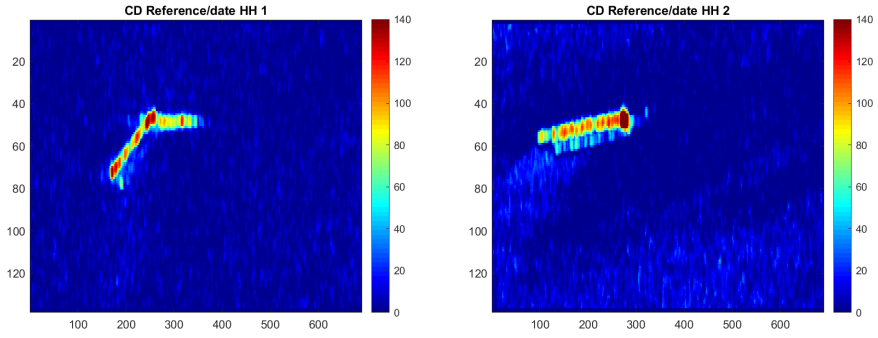


(d) CD MP date 1 (e) CD MP date 2

Figure 7.5: CD results for RP and MP modes: (a) classical bi-date with overlapping target, (b) FBR-RP (random pixel selection) CD with date 1, (c) FBR-RP (random pixel selection) CD with date 2, (d) FBR-MP (multitemporal selection) CD with date 1, (e) FBR-MP (multitemporal selection) CD with date 2

### 7.2.2 Study case in Singapore Region

We chose then a more complex example in Singapore in the industrial harbor of Jurong Island. Figure 7.6a shows the FBR image computed using 83 Sentinel GRD (Ground Range Detected) images of Singapore projected on Google Earth (area of interest in the yellow rectangle).

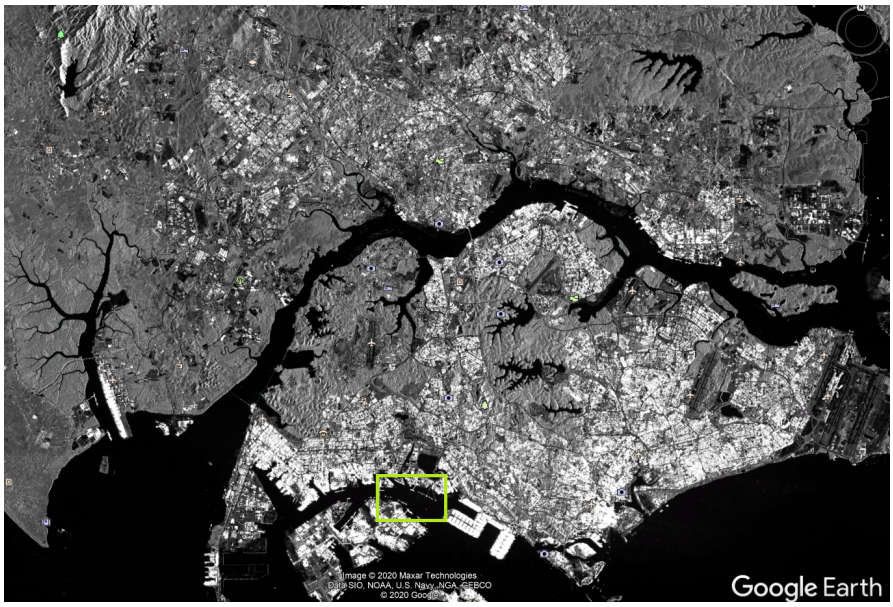


(a) FBR scene computed from Sentinel 1 GRD dataset (2017-2019) projected on Google Earth

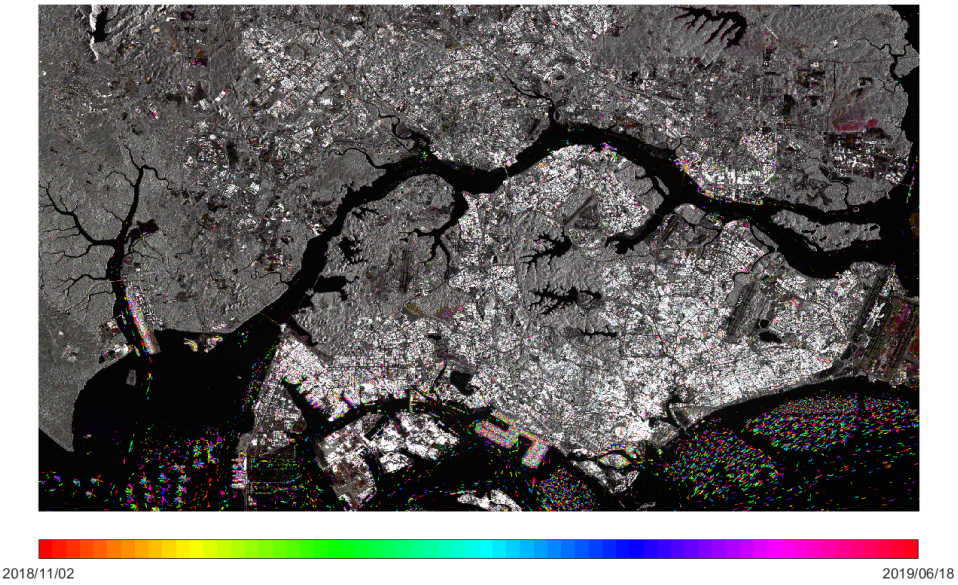


(b) REACTIV (from November 2018 to June 2019)

Figure 7.6: (a) FBR scene of Sentinel 1 GRD dataset above Singapore projected on Google Earth (years 2017 to 2019), (b) Illustration of maritime activity with REACTIV (November 2018 to June 2019)

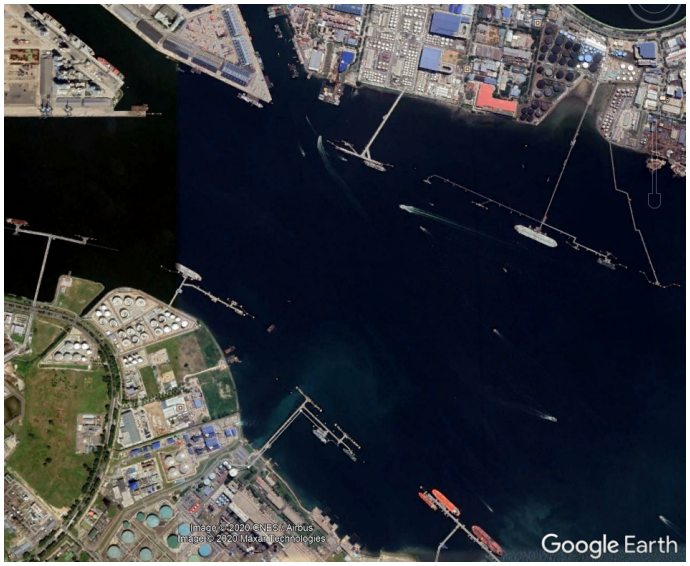


(a) Google Map 8 March 2017


(b) FBR (50% transparency) and Google Map (50% transparency)

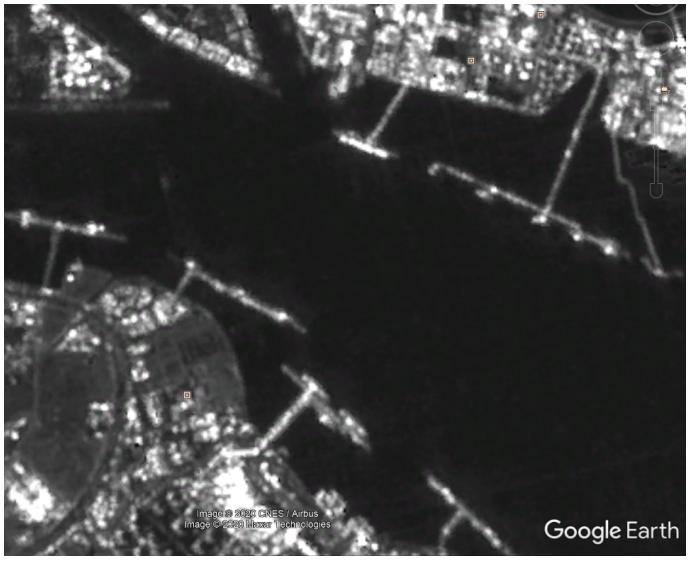


(c) FBR image VH

Figure 7.7: Area of interest: Jurong Island industrial harbor (**a**) Google Map image, (**b**) 50% transparency Google Earth and 50% transparency FBR VH and (**c**) FBR VH only

We present a result of REACTIV software in figure 7.6b to have an overview of the dense maritime traffic in this area. REACTIV software represents only the biggest changes in the time-series; however, it gives an excellent idea of the maritime activity over a long time-series. As we can observe from Figure 7.6, the FBR scene represents visually only stable structures and discards the ephemeral objects such as ships. The characteristics of the Sentinel data used in this study can be found in Table 2.1 of Chapter 2. In addition, Figure 2.3b represents the operations performed for each GRD image of the stack. The images of the stack were afterward coregistrated according to the first image of the stack using the function « Coregistration » of SNAP (Sentinel Application Platform) software [48].

Since the environment is constituted of man-made structures, we chose to use SAR images with always the same observation configuration, and thus the same orbit number. Indeed, most man-made structures cannot be considered to possess an azimuthal symmetry, and a subtle change in the observation angle can drastically affect their backscattered signals. Using different orbits to compute the FBR image might corrupt the estimation of a stable background. The study of harbors is a challenge in target detection; indeed, metallic structures are associated with high scattering contributions. For instance, it is challenging to discriminate mooring quays and actual ships. Besides, the number of ships evolves from a date to another. Some ships can remain in the same position during several acquisitions, but also different ships can occupy the same pixels on consecutive acquisitions. This partial or full overlapping in time can produce misinterpretation in the CD results with classical methods. This example is a direct application of the FBR procedure to estimate a stable background within the observed scene and detect only ephemeral objects at each acquisition.

Figure 7.7 presents the zoom of the FBR Scene in the area of interest. From top to bottom are shown the Google Map Image from 8 March 2017, then the FBR image with Google Map in 50 % transparency, and finally, on the bottom, the FBR image only in VH polarisation. As we can observe, the FBR image matches well with the optical image; the metallic moorings give strong radiometric signals and are well visible on the FBR image. The harbor structures are well preserved, and all ephemeral objects have been removed.

### Bi-date Change Detection analysis

We study a configuration of temporally superimposed targets adjacent to a permanent scatterer (mooring quays). In Figure 7.8, we can observe ships circled in red for two dates. They share the same position during the two acquisitions and are adjacent to mooring quays. We can notice from these images that most of the ships present in the scene are moored to the quays. In this configuration, the detection of boats is rendered difficult, contrary to the open sea case. The change detection was computed, for both VH and VV, as previously described in Section 7.2.1 with the two consecutive dates of Figure 7.8 for classical bi-date change detection and then separately with the computed FBR image.

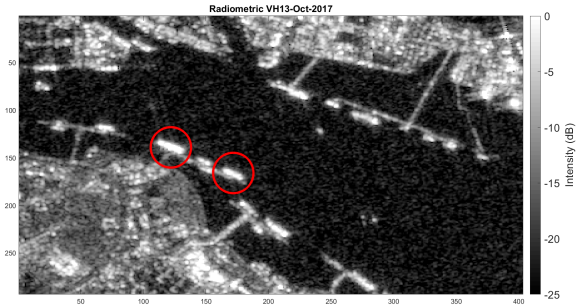


(a) Radimetric VH 13/10/2017

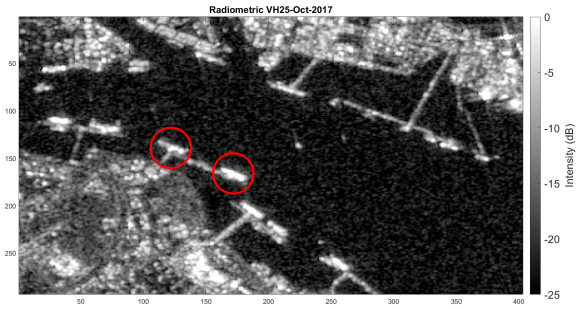


(b) Radiometric VH 25/10/2017

Figure 7.8: Consecutive radiometric images for VH polarisation: (**a**) Radiometric VH 13 October 2017, (**b**) Radiometric VH 25 October 2017 (Sentinel 1 GRD data).

From the classical bi-date change detection shown in figures 7.9a and 7.9b, the moored boats do not appear in the detection map since there is time overlapping. Within the FBR CD maps in Figure 7.9c, 7.9d, 7.9e, and 7.9f, where the FBR change detection is illustrated, it is possible to identify them more efficiently since the CD is operated from the FBR image, which is a target free scene. This is valid for both polarizations. Therefore, the interpretation is improved and the CD map from a FBR method gives more consistent results when the user is interested in evaluating the content of ephemeral targets at a specific date.

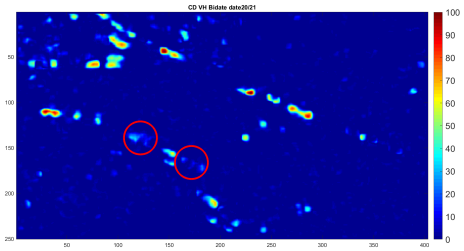

(a) Classical Bi-date VH

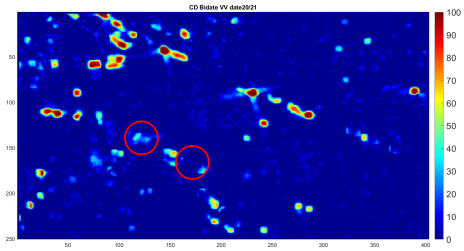

(b) Classical Bi-date VV

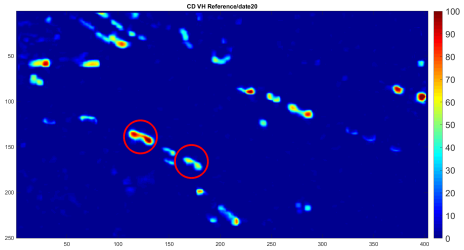

(c) FBR and 13/10/2017 VH

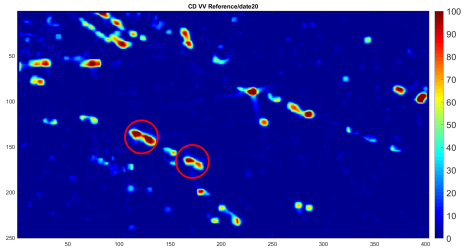

(d) FBR and 13/10/2017 VV

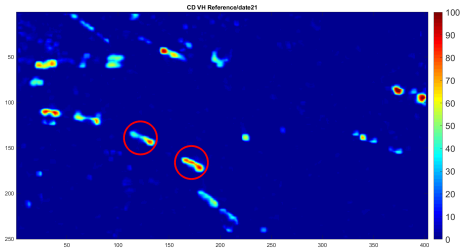

(e) FBR and 25/10/2017 VH

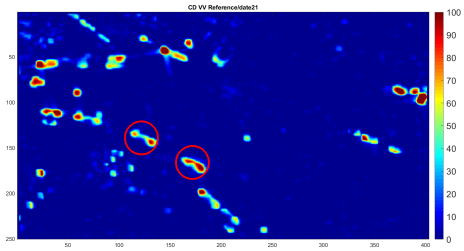

(f) FBR and 25/10/2017 VV

Figure 7.9: Raw output CD comparison for the dates 13/10/2017 and 25/10/2017 : (**a**) Classical Bi-date VH, (**b**) Classical Bi-date VV, (**c**) CD FBR for date 13/10/2017 VH, (**d**) CD FBR for date 13/10/2017 VV, (**e**) FBR-CD for date 25/10/2017 VH, (**f**) FBR-CD for date 25/10/2017 VH.

### Multitemporal Change Detection analysis

A classical strategy for change detection in time-series is to perform a bi-date change detection sequentially to obtain binary words relative to a specific sequence of changes. Similarly, we can obtain binary words comparing each image of the time series with the FBR image. For the sake of simplicity and ease of the interpretations, we presented the result for the HV channel on the first four images of the stack. These four images can be found in Appendix B.2. The results are presented in Figure 7.10a for the classical sequential bi-date procedure and in Figure 7.10b for the FBR change detection framework we proposed. For the result shown in Figure 7.10a, the obtained binary corresponds to the transition between sequential bi-dates. Since four dates were chosen, three tests were performed sequentially to create the binary words $A_{1\to2}A_{2\to3}A_{3\to4}$ where

$A_{n \to n+1}$ corresponds to the binary outcome of the test between date n and n+1. If a change occurred between date n and n+1, the outcome is 1; if no change occurred, the outcome is 0.

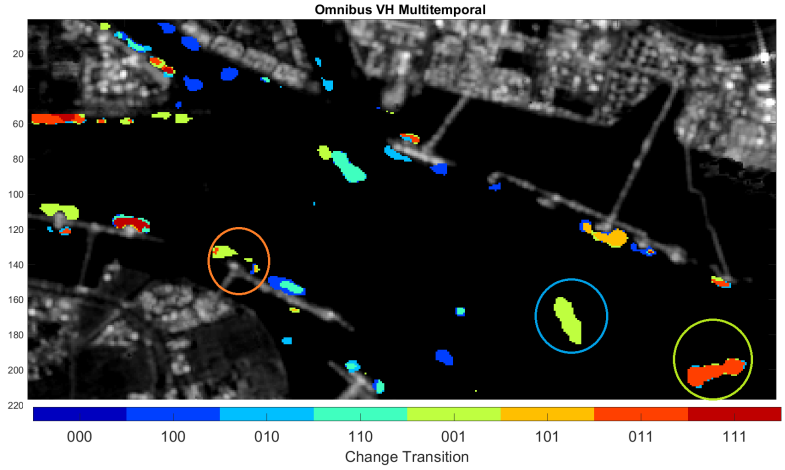


(a) Sequential bi-date VH

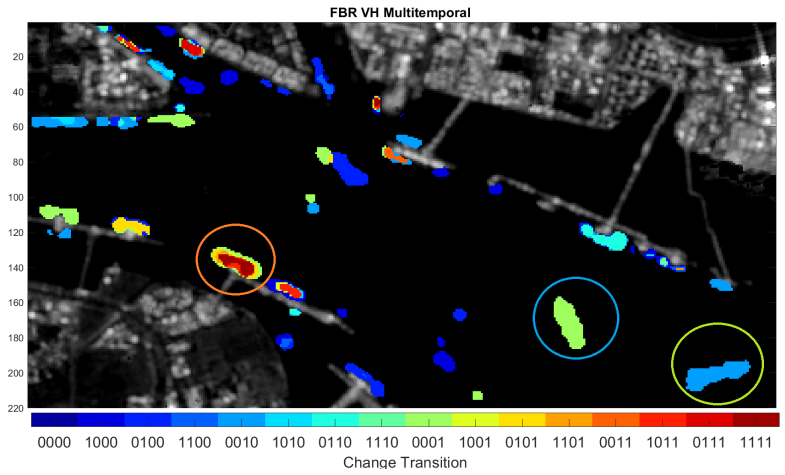


(b) FBR VH

Figure 7.10: (**a**) Four dates sequential bi-date change detection analysis, (**b**) CD FBR computation on the four first dates.

For the result shown in Figure 7.10b, the obtained binary word corresponds to the outcome of the test between our FBR image and the current scene. Since four dates were chosen, four tests were performed sequentially to create the binary word $B_{FBR \to 1} B_{FBR \to 2} B_{FBR \to 3} B_{FBR \to 4}$ where $B_{FBR \to n}$ corresponds to the binary outcome of the test between the FBR image and the date n. This outcome can then be interpreted as 0 if no target is present and 1 if a target is present.

We focused on the three different scenarios circled within Figure 7.10. The area circled in light green gave a binary word "011" for the sequential bi-date test in Figure 7.10a since a boat appeared at date 3 and disappeared at date 4. The results of the FBR procedure in Figure 7.10b gave "0010" since the target was only present on date 3.

The area circled in blue gave a binary word "001" for the Omnibus test in Figure 7.10a since the boat appeared on date 4 and was not present on date 3. The results of the FBR procedure in Figure 7.10b gave "0001" since the target was only present on date 4.

The area circled in orange was a high attendance zone where ships were present for each acquisition from date 1 to date 4. The result with the sequential bi-date test is more difficult to interpret due to the partial and total target overlapping between each acquisition. With the FBR procedure, the outcome is "1111" near the mooring quay since targets have been detected at each date. However, the size of targets may vary from acquisition to another, so different binary words are found around the center of detection. In general, the interpretation of such a map is not convenient due to the high number of possible combinations (maximum $2^{(D-1)}$ with D dates), and this remains a problem. The type of representation typically depends on the application (Number of changes, first change, last change, change combination).

As explained before, the main advantage of the proposed method is that it is possible to retrieve the information relative to ephemeral targets at a specific date. It can be a great interest for operators to obtain a detection output at a specific date corresponding to what specifically happened at this day. For instance, if the amount of changes has been judged unusual, a change map corresponding to the ephemeral objects present in the scene is available.

**Ship number estimation within the scene using FBR procedure**

We focus now on the estimation of the number of ships for each acquisition. First, a mask was defined to exclude possible changes coming from the land areas, as shown in annex Figure B.1 in light blue. It is now possible to estimate the number of ships for each acquisition by using the FBR procedure and setting a threshold on the raw output CD for each acquisition. The change detection map can be superimposed with the reference image when the user is interested in a specific date to improve the interpretation, as shown in Figure 7.11b,d, and can evaluate the ship traffic for a given date.

The Matlab function **bwconncomp** is used to determine the number of binary objects forming a group of pixels detected within the scene. The estimated ship number for each acquisition date is presented in figure 7.11e for VH channel. To validate the results, it is important to have AIS (Automatic Identification System) signals to obtain information about ships present in the scene at the time of the acquisition. Unfortunately, we did not have historical AIS signals to verify the accuracy of the detection. In order to verify the consistency of the results in some way, we propose to consider the dates where we detect the lowest and the highest number of ships. For these dates, we display in Figure 7.11 the radiometric images and the CD maps obtained from our FBR method.

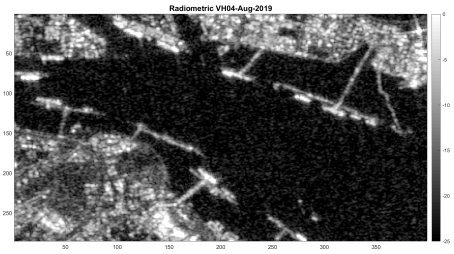


(a) Radiometric 4 August 2019

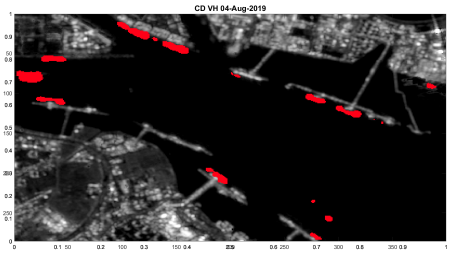


(b) CD FBR 4 August 2019

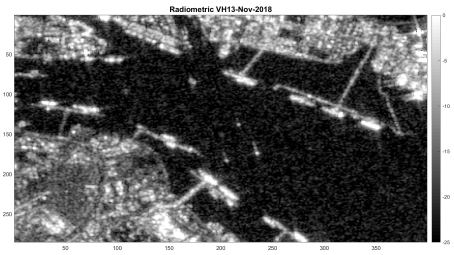


(c) Radiometric 13 November 2018

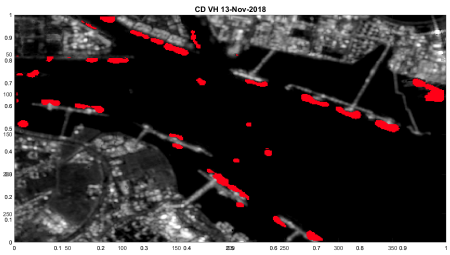


(d) CD FBR 13 November 2018

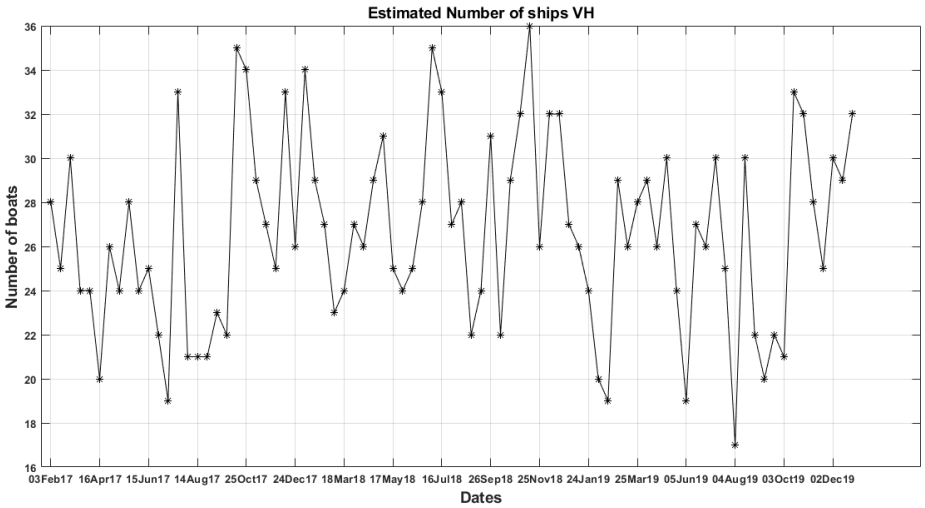


(e) Estimated number of ships per acquisitions (VH)

Figure 7.11: Images of highest and lowest attendance detected with the FBR method: (**a**) Radiometric 4 August 2019, (**b**) CD FBR 4 August 2019, (**c**) Radiometric 13 November 2018, (**d**) CD FBR 13 November 2018 and (**e**) Estimated number of ships per acquisition in the area of interest.

These acquisitions corresponded to the 13 November 2018 as shown in Figure 7.11c for the highest attendance of 36 ships and to the 4 August 2019 for the lowest attendance in Figure 7.11a with 17 ships. As we can observe from the radiometric images visually, most of the quays were free of ships, and few ships were visible in the middle of the harbor for the image acquired on 4 August 2019. On the contrary, for the 13 November 2018, the number of ships moored to the quays and in the middle of the harbor appears to be significantly higher. The results seem to be reasonably coherent with what we can observe on the radiometric images. However, it is not possible to verify

on each image the number of boats with only SAR images. It would be interesting to evaluate the procedure on a dataset with ground truth (optical images, for example, or AIS dataset) to fully characterize the method.

**Verification with AIS signals: Sentinel 1 image acquired on 22 August 2020**

In this example, we propose to compute the FBR image from 2017 to 2019 as done previously and evaluate the results of change detection using live AIS signals captured from marinetraffic.com.

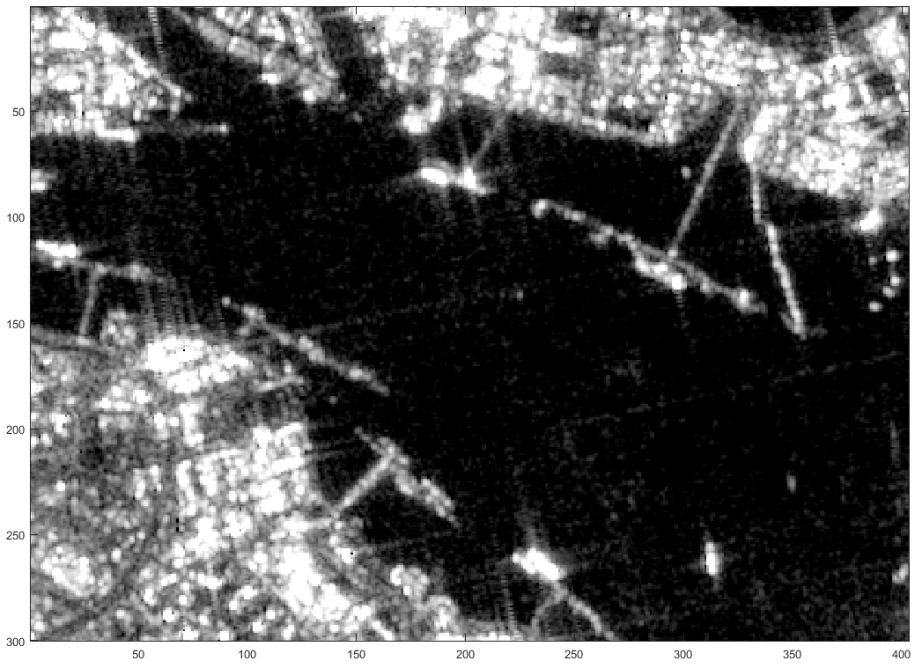


Figure 7.12: Sentinel 1 GRD VV acquired the 22 August 2020 at 11h25min30s (scaled [-20 5dB])

The SAR image of interest has been acquired the 22 August 2020 at 11h25min30s UTC; the detection results on VV channel are presented in Figure 7.12. The acquisition of Sentinel 1 is around 30s for a given footprint. Figure 7.13a presents the capture of live AIS signal collected at the time of the Sentinel acquisition, and figure 7.13b presents the detection map projected on the FBR image. For AIS, the color code gives the type of ships. When there an arrow shape, it means the ship is moving. When there is a dot or a ship shape, it means that the ship is not moving. When the color is plain, the AIS signal is recent (but recent may mean some minutes ago), whereas a transparent color means an old AIS information (some hours ago). The ships circled in red on both AIS and detection maps represent big vessels with a size superior to 30m that are all well detected. The ships circled in green are smaller ships or groups of smaller ships that are also well

detected. In Figure 7.13b, we circled in blue the detection of objects without AIS.Finally, in Figure 7.13a, we circled in blue every ship with AIS signal that is not detected and is not visible as well on the SAR image.


(a) AIS signal

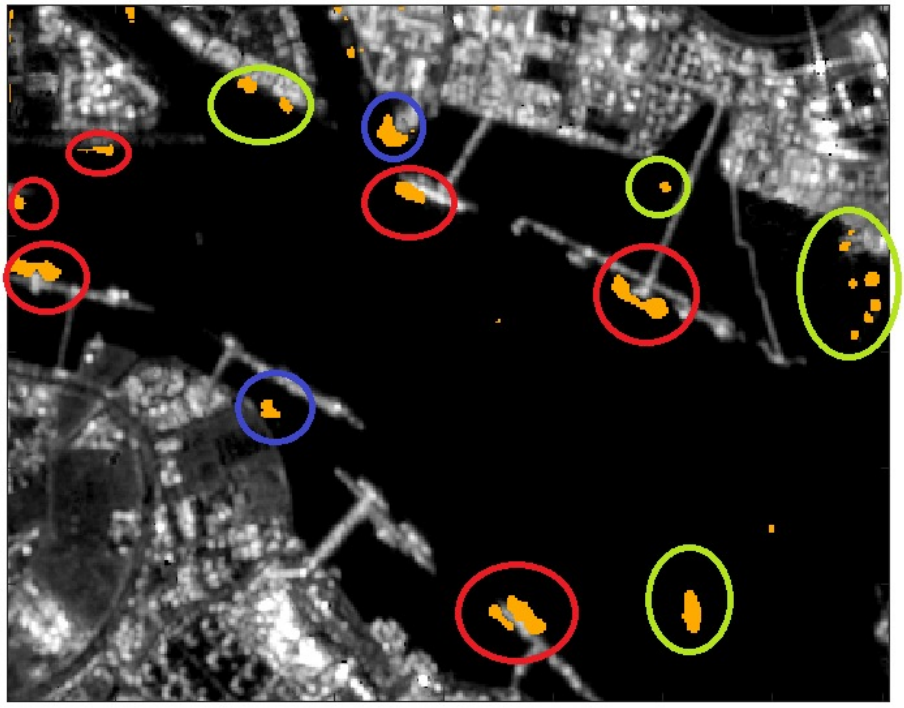

(b) FBR-CD VV

Figure 7.13: (**a**) AIS signal captured from marinetraffic.com the 22 August 2020 at 11h25min30s UTC, (**b**) Associated FBR-CD projected on the FBR image in background

For blue circle 2 and 4, all AIS signals are transparent, corresponding to old signals. When the satellite passes over, there may be no targets there. For blue circle 3, 5 AIS signals are present and recent. They correspond to tugs. They are typically 30m*10m, so about two pixels in size. None is detected. For blue circle 5, we can notice that most AIS signals are transparent, so old, or with an arrow, so moving. There is only one AIS signal meaningful, corresponding to a tug. For blue circle 1, disregarding the old signals, there are some AIS signals not detected. Looking at the SAR image, it seems there are some ships not detected.

Considering the resolution of Sentinel 1 (20x20m), the result is encouraging. Some ships may not have a signature on the SAR image due to their shape, material, or simply because they are too small. However, our method gives a fair estimation of ephemeral objects that are physically detectable by Sentinel 1 SAR images. We can notice that most of the ships present are moored or near the harbor infrastructures, which encourages the benefit of our method in such environments.

## 7.3 Discussion on FBR procedure for maritime surveillance application

As presented, the proposed method is interesting to obtain a change map of objects that are not part of each date's background. In particular, its interest has been demonstrated in the challenging environment of a harbor.

Outside of the harbors, two important phenomenons for maritime surveillance may affect our method: the state of the sea surface and the tidal effect. Indeed, Singapore is in a zone with a low tidal effect, and inside harbors, we can consider that the sea state remains unchanged because protected by the surrounding lands and infrastructures.

The sea state's effect has to be checked in different situations (sea state, resolution, sensor frequency of operations etc.). The coastal tidal effect is one phenomenon that also causes several issues (appearance of rocks for example) and may corrupt the background estimation of the scene since the background would evolve periodically. Since the tidal effect is a predictable phenomenon, we could map the available acquisitions with a given tidal state when the study area is subject to a strong tidal effect. The tidal effect could then be avoided by computing one FBR image per tidal state that would hopefully give more accuracy on the background estimation of the image at a given time and then a better detection result.

**Summary**: This chapter illustrated the use of FBR CD for maritime surveillance with an application using a UAVSAR dataset and a Sentinel 1 GRD dataset. The second example showed the great interest of this method in harbor environments where it is usually challenging to obtain accurate results due to strong backscattering signals coming from harbor infrastructures.

In terms of interpretation, the FBR offers the remarkable ability to estimate the change for each date (with respect to an estimated stable scene), instead of sequential bidate changes. This is one significant advantage compared to sequential method of change detection. As shown through the different results, the FBR procedure is interesting when the purpose is to determine the number of ephemeral objects at a specific date. The computation of the FBR image can become a difficult task with a background subject to temporal periodical variation (tidal effect), or with an important background change (demolition of a quarter). These configurations have to be taken into account to improve the proposed method and implement it in a wider range of applications. The proposed framework is also designed to consider future satellite missions that can offer a much higher temporal resolution and therefore a possibility to better estimate the background of the scene implying more accurate detection results.

# Chapter 8

# Foliage Penetration (FoPen) applications

**Objectives** : In this chapter, we address the problem of FoPen (Foliage Penetration) missions. This SAR application is performed at low radar frequencies (L-band or lower) to penetrate the foliage and let the wave reach the ground. Two missions will be investigated to benefit from multitemporal acquisitions and therefore evaluate the gain in the detection of target concealed below the canopy. The TROPISAR mission, a polarimetric dataset acquired at P-band by SETHI radar (developed by ONERA) and CARABAS II challenge data acquired with CARABAS II airbone radar developed by FOI (Swedish Defense Research Agency). We will, at this occasion, evaluate the detection using polarimetric FBR images for TROPISAR mission. In a second time we will exploit the different flight headings acquired for CARABAS II challenge dataset to generate a FBR scene. Afterward we will compare the performance of detection either using a single flight heading for the computation of the FBR scene or various flight headings.

We chose two missions to evaluate the performances of the FBR procedure for FoPen change detection applications quantitatively. The TROPISAR mission has been acquired in French Guyana by ONERA at different frequencies (P and L bands) for several applications (FoPen detection, tomography and biomass estimation)[17]. The second mission of interest, CARABAS II, has been acquired by the FOI (Swedish Defense Research Agency) in Sweden at 70MHz with several target

deployment and flight headings. More specific information about the mission can be found in [16]. In this chapter, we will first briefly introduce the specificities of FoPen SAR detection. In a second time, we will compare the performances of CD methods in bi-date, overall omnibus, and FBR-based cases for the TROPISAR mission. Afterward, we will evaluate the performances of FBR-CD method for the mission CARABAS-II where targets are present in different acquisitions and target positions.

## 8.1 Specificity of FoPen detection

The detection of man-made structures in SAR FoPen applications has been studied for instance in [96, 97] by projecting the radar signal in target and clutter (interference) subspaces using a single acquisition. This method is interesting because only one acquisition is necessary. For this approach, the model of interferences is based on a canonical representation of trunks [15].Indeed, at low frequencies, backscattered signal can be modeled as a coherent combination of four possible contributions trunk/ground as we can see in Figure 8.1. Interactions 2 and 3 constitute the strongest mechanisms. The trunks are, in that case, considered as dielectric cylinders.

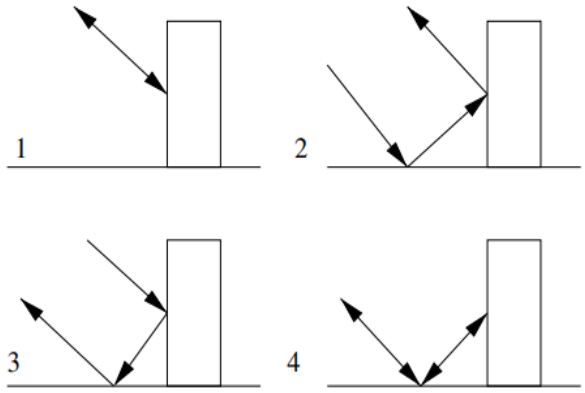


Figure 8.1: Contributions involved at low frequency for the backscattered signal of a trunk (considered as a dielectric cylinder) from [15]

However, it is challenging to create a model that can be efficiently applicable everywhere considering the variety of forest. Indeed, the terrain, the forest (density of trees, geometry, dieletric properties) and topography need to be accurately known as they significantly impact the nature of the backscattered signal. Depending on the type of forest (and on the radar frequency), the branches interactions might also be considered, which brings additional difficulty for modeling the scene interferences. This detection method relies on the differences between the scattering pattern of the target on the one hand and the trees on the other hand.

Using time-series could enable us to benefit from additional differences: the target that we look for can be considered as an ephemeral object, while trees remain at the same position, whatever the date of acquisition. Therefore, the use of change detection in multitemporal SAR images is an interesting solution to overcome these issues. We can suppose that the trunks/branches constitute a stable deterministic signal in time during a reasonable acquisition span. We aim to compute a FBR image of a forest at low frequencies and in a second time to detect ephemeral man-made targets in FoPen environment using CD between two or more SAR images as in [98, 33]. This framework may be interesting at low frequencies since most of the backscattered contribution is coming from the trunks and big branches as well as interactions between the ground and trunks [34]. Two dataset will be investigated for FoPen detection, TROPISAR (P-band in tropical forest with 8 acquisitions) and CARABAS II (VHF 70 MHz with 3 set of 8 acquisitions monitored at different flight headings).

## 8.2 TROPISAR mission

We propose first to investigate a polarimetric dataset. This mission has been acquired above the French Guyana by an airbone radar (SETHI) developed by ONERA. The selected set of SAR images consists of 8 P-Band coregistered images of tropical forest where cars have been parked under foliage at a specific date.

### 8.2.1 Data Presentation

During this experiment, some vehicles and a trihedral have been placed along a small dirt road under foliage on the 24 August 2009 (image tropi402) as we can observe in Figure 8.2.

Table 8.1: SETHI charactecteristics and dataset information for temporal P-band TROPISAR products used for the analysis

| **Technical Characteristics of Sethi SLC products for TROPISAR Mission** | |
|---|---|
| **Polarisation** | HH+HV+VH+VV |
| **Range resolution** | 1.2 m |
| **Azimuth resolution** | 1.5 m |
| **Centrale Frequency** | 400 MHz |
| **wavelength** | 0.75m |
| **Incidence Angle** | 30° |
| **Acquisition dates** | From 10 August to 1 September 2009 |
| **Location** | `http://maps.google.com/maps?q=5.275216,-52.923660` |

The tables 8.1 and 8.2 presents the parameters of SETHI radar and the acquisition dates of

Table 8.2: Acquisition dates for the P-band temporal stack and corresponding images according to [17]

| **Acquisition dates and corresponding image name** | |
|---|---|
| **10 August 2009** | tropi007 |
| **12 August 2009** | tropi104 |
| **14 August 2009** | tropi208 |
| **17 August 2009** | tropi305 |
| **24 August 2009** | tropi402 |
| **30 August 2009** | tropi506 |
| **30 August 2009** | tropi507 |
| **1 September 2009** | tropi603 |

the image used for this study.

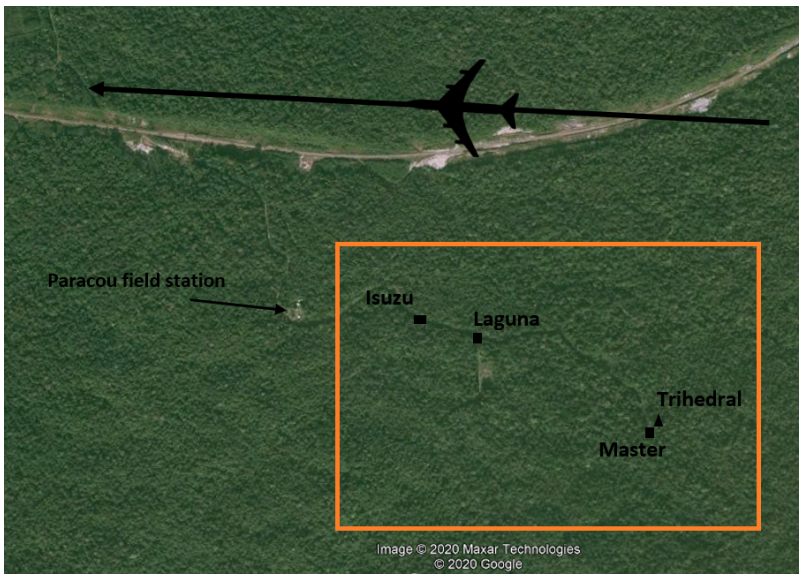


(a)

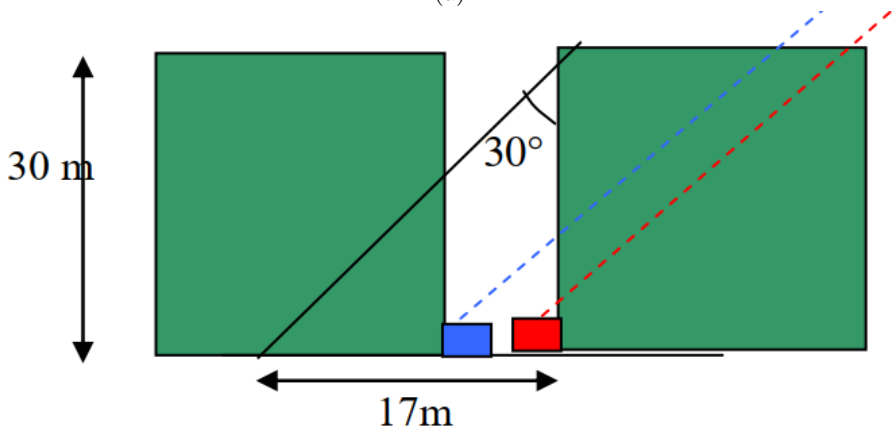


(b)

Figure 8.2: (a) Test site and targets disposition of targets for TROPISAR mission over the field station of Paracou, adapted from [6], (b) Drawing of the configuration (side view), green blocks represent the forest, blue box being the Isuzu and red box the laguna from [6]

The results for change detection between two dates at L-band and P-band are presented in [6],

and the following conclusions can be drawn: the detection is more efficient at P-band compared to L-band. It is a well-expected result considering the extremely dense nature of the tropical forest in French Guyana. Besides, this study showed that 3 targets out of 4 could be detected using this method, the Laguna being undetectable in any configuration. As we can observe in the diagram taken from the same article, if a car is parked on the left side of the road (radar wave coming from the right side), the radar wave travels through less vegetation compared to a car parked on the right side. In conclusion, the laguna cannot be detected because of the strong two ways attenuation estimated of 14dB in HH and 17.6 dB in VV. Since a set of 8-band images is available for this mission, we want to investigate the gain of using several acquisitions to detect those targets. We will study the possibility to generate a FBR scene of the acquisition and afterwards perform change detection to evaluate its benefits.

### 8.2.2 Change Detection analysis

The exact position of the Laguna being unknown, we will not consider it in the detection problem. We will, therefore, consider the 3 targets for which we can create a ground truth. In Figure 8.3b are shown the Isuzu (target 1 red rectangle), the Master (target 2 on the left side in the white rectangle) and the trihedral (target 3 on the right side in the white rectangle)

As we can observe in Figure 8.3a it is not possible to distinguish visually the targets that have been placed in the observed scene due to the high clutter of the tropical forest. Different CD statistics to highlight the targets will be presented first qualitatively by showing the raw output of the test. Afterward, the detection will be evaluated quantitatively by calculating experimentally the probability of detection (PD) and probability of false alarm (PFA) according to the available ground truth.

Different Pauli representation are presented in Figure 8.4. In Figure 8.4a is shown the Pauli representation of the first date of acquisition tropi402 calculated with an average box of 3x3 pixels, it is still not possible to distinguish the targets easily from this simple polarimetric representation. In Figure 8.4b is presented the temporal Pauli representation and in Figure 8.4c the associated FBR scene in Pauli representation.

In this study we are interested in the clutter cancellation of the surrounding background that is mainly constituted of trunks. We compare three statistical tests for this study: the GLRT (omnibus) calculated on the 8 acquisitions, a bi-date change detection with the closest acquisition to tropi402 (which is tropi506) and finally, the change detection with the FBR procedure considering the whole candidate pixels and the image tropi402.

First the raw outputs of the algorithm in bi-date case $\gamma_G$, omnibus case $\gamma_{GM}$ and from the FBR

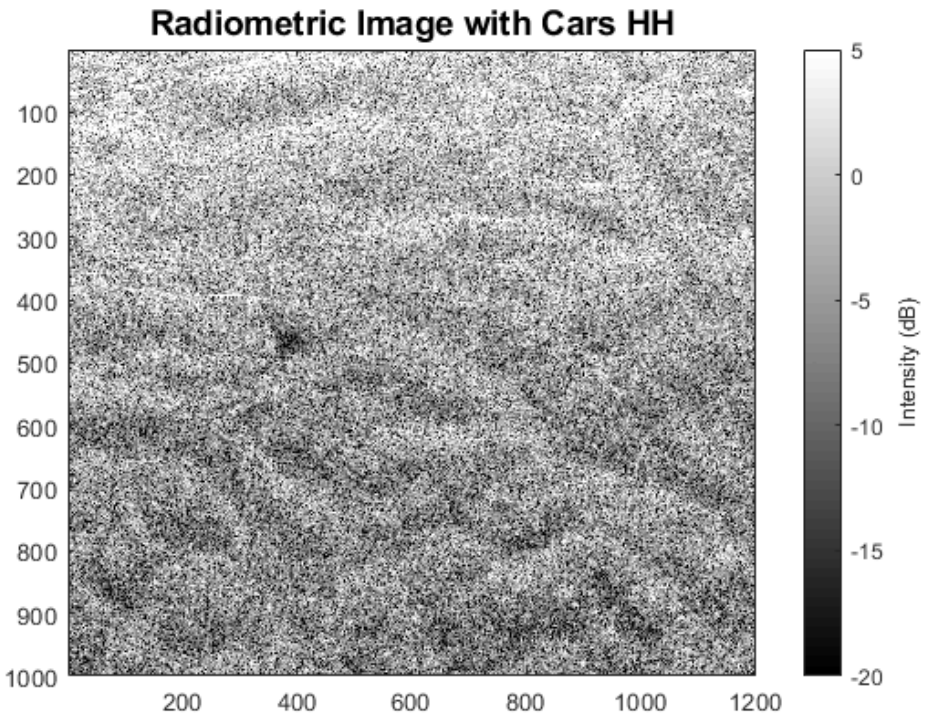


(a) HH Image with targets


(b) Ground Truth

Figure 8.3: (a) radiometric HH image tropi402 containing targets monitored at P-band the 24 August 2009. (b) Associated ground truth : target 1 (Isuzu), target 2 (Master on left side) and target 3 (P-band trihedral on right side)

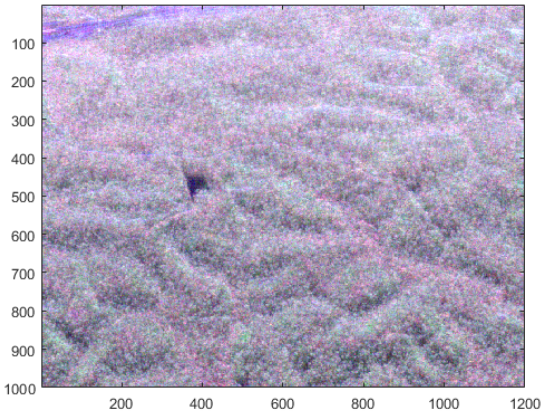


(a) Pauli spatial tropi402

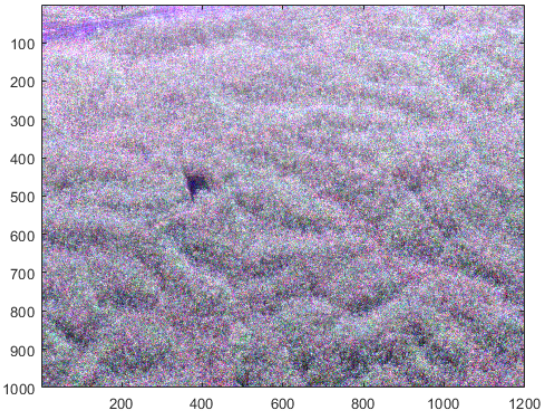


(b) Pauli temporal

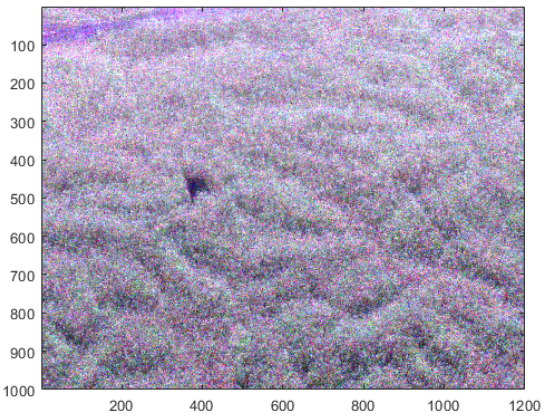


(c) Pauli FBR

Figure 8.4: (a) Spatial Pauli representation of image tropi007 (3x3 spatial average box), (b) temporal Pauli representation, (c) FBR Pauli representation, R=$|HH - VV|$(representing Double Bounce), G= $2|HV|$(Volume), B=$|HH + VV|$ (Single Bounce), scaled [-20 5] dB

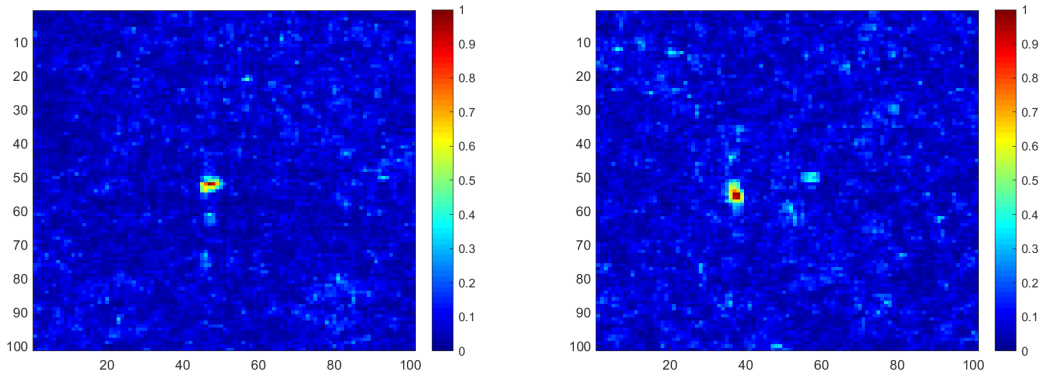

(a)



(b)

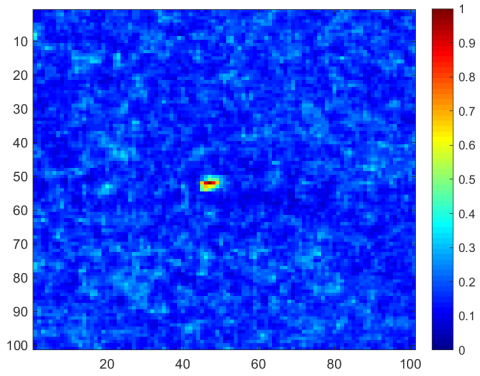

(c)

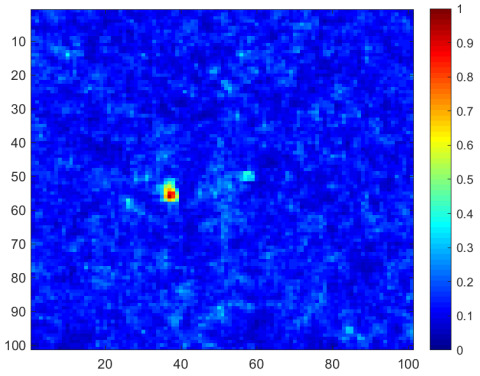

(d)

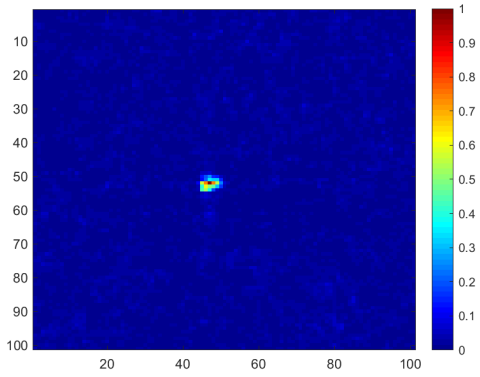

(e)

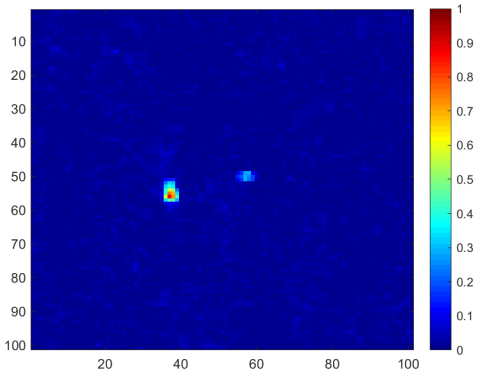

(f)

Figure 8.5: CD Full Polarimetric: (a) Bi-date detection of target 1 (tropi402 vs tropi 506), (b) Bi-date detection target 2 and 3 (tropi402 vs tropi 506), (c) Omnibus detection of target 1 (whole time-series), (d) Omnibus detection of targets 2 and 3 (whole time-series), (e) FBR detection of target 1 (FBR image vs tropi 402) and (f) FBR detection of target 2 and 3 (FBR image vs tropi 402). Average spatial window = 3x3 (N=9)

procedure $\gamma_{MP}$ are present in Figure 8.5. In addition, the corresponding ROC curves computed from the ground truth are presented Figure 8.6, for each polarisation and for the full polarimetric case. For the bi-date case and omnibus case, in Figure 8.5a,8.5b,8.5c and 8.5d we can observe that

the clutter of the forest remain high and visually the possibility of false alarm seems high. On the contrary Figure 8.5e and 8.5f the clutter has been successfully cleared using the FBR procedure. In order to evaluate the performance quantitatively, we use the ground truth Figure 8.3b and compute the Probability of detection $PD = \frac{TP}{NT}$ and the probability of false alarm as $PFA = \frac{FP}{NB}$ with $TP$ the number of pixels truly detected as target (True Positive), $NT$ the number of pixels defined as target in the scene (3 targets of 5x5 pixels), $FP$ the number of background pixels detected as target (False Positive) and $NB$ the number of pixels defined as background.

The figure 8.6a, 8.6b and 8.6c represent the PD-PFA curves in the monopolarisation case and show that the performance are better in HH, HV and VV for lower PFA (below 0.1). The figure 8.6d represents the performence using the full polarimetric vector. The same general comment can be done regarding the computed PD and PFA.

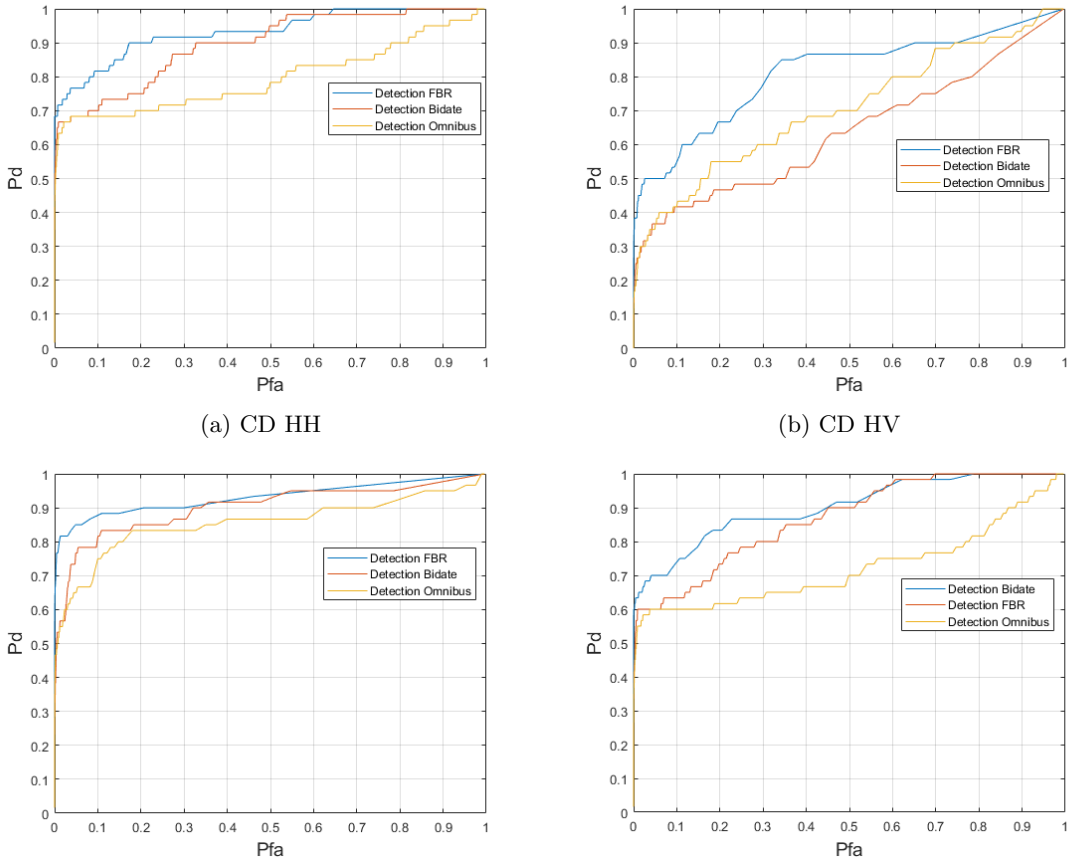


(a) CD HH

(b) CD HV

(c) CD VV

(d) CD Polarimetric

Figure 8.6: CD ROC, blue curve FBR change detection, red curve Bi-date, yellow curve omnibus detection: (a) HH, (b) HV and (c) VV, (d) FullPol

In general, the main advantage of the CD based procedure for target detection is that no a priori information on the target or the background are required. Increasing the knowledge on the background by using several measurements of temporally stable pixels provides better detection

capabilities of targets. With this study, we have shown that the FBR based change detection enables a good clutter noise cancellation to decrease the probability of false alarm significantly and increase the probability of detection with a small spatial averaging window.

### 8.2.3 Discussion

For this example, we have evaluated the detection of vehicles (and corner reflector) hidden under the canopy of a tropical forest. This detection has been made possible through the use of low radar frequencies that enable to penetrate through the foliage and reach the ground. We have compared three statistics to evaluate quantitatively the gain of using several acquisitions to build a FBR scene that can be used afterwards for change detection and detect objects at a given acquisition. However, in this specific case, we have to note that there is a short time between acquisitions (2 to 7 days) and between the first and last acquisition (22 days). In addition, acquisitions at P-band probably favors a stable temporal background of the scene and therefore appear robust to intrinsic temporal variations of the vegetation such as growth of vegetation and seasonal effects. It would be then interesting to study such strategy with a longer time span over tropical forest to highlight possible limitations introduced by the seasonal variations of the environment.

## 8.3 The CARABAS II challenge

We now investigate the second dataset, CARABAS II challenge, for FoPen application. This campaign has been acquired in monopolarisation case (HH) with several flight headings for the same scene and with different target deployments. We want to evaluate the possibility of using several flight headings to compute a FBR image. Computing a FBR image with different flight headings seems at a first sight not rigorous since the backscattered signal is a priori different from an observation angle to another. However, we can reasonnaly assume that the trees possess an azimuthal symmetry property. Especially at low frequencies where the main contributing structures are trunks, generally modeled as vertical dielectric cylinders. Here, two sets of SAR images have been acquired with close flight headings (FH=225°and FH=230°) and the other one with an orthogonal direction (FH=135°).

### 8.3.1 CARABAS characteristics and data presentation

CARABAS II is a VHF SAR imaging system developed by FOI (Swedish Defense Research Agency), the main characteristics of this campaign are presented in Table 8.3. The campaign itself consists of the observation of 4 groups of targets, called missions or target deployments, shown in Figure 8.7. A color is attributed for each target deployment in Figure 8.7 and the associated characteristics are described in Figure 8.8a. For each target deployment, two passes have been acquired with 3 flight headings: 225, 230 and 135° (0°would be a flight heading towards the north, the flight heading is to be considered as a clockwise direction according to the north) as presented in the Figure 8.8a.

Table 8.3: CARABAS II charactecteristics and dataset information for the challenge dataset

| **Technical Characteristics of CARABAS II challenge dataset** | |
|---|---|
| **Mode** | Strip map |
| **Polarisation** | HH |
| **Range pixel spacing** | 1 m |
| **Azimuth pixel spacing** | 1 m |
| **Range resolution** | 2.5 m [5] |
| **Azimuth resolution** | 2.5 m [5] |
| **Centrale Frequency** | 63 MHz |
| **Bandwidth** | 65 MHz |
| **wavelength** | VHF |
| **Incidence Angle** | 58° |
| **Acquisition dates** | 2002 (summer) |
| **Location** | `http://maps.google.com/maps?q=66.385712,19.242308` |

We can notice with Figure 8.8a that for targets deployments 2, 3 and 4, there is always a config-

uration where the vehicles are parked parallel to one of the flight path and therefore perpendicular to the other flight path. For target deployment 5, the vehicles are organized in a way that for all flight headings the vehicles will be tilted of around 45° so that no specular reflection will be seen by the radar. In addition, we can observe from Figure 8.8 that the targets are organized in a gradient of sizes, with 3 possible sizes of vehicles : TGB11 (4.4x1.9x2.2 m), TGB30 (6.8x2.5x3.0 m) and TGB40 (7.8x2.5x3 m) presented in Figure 8.8b, 8.8c and 8.8d. The environment is a sparse forest with long and thin trunks with relatively smooth ground surface.


Figure 8.7: Representation of the scene with positions of target deployment (called missions in the challenge)

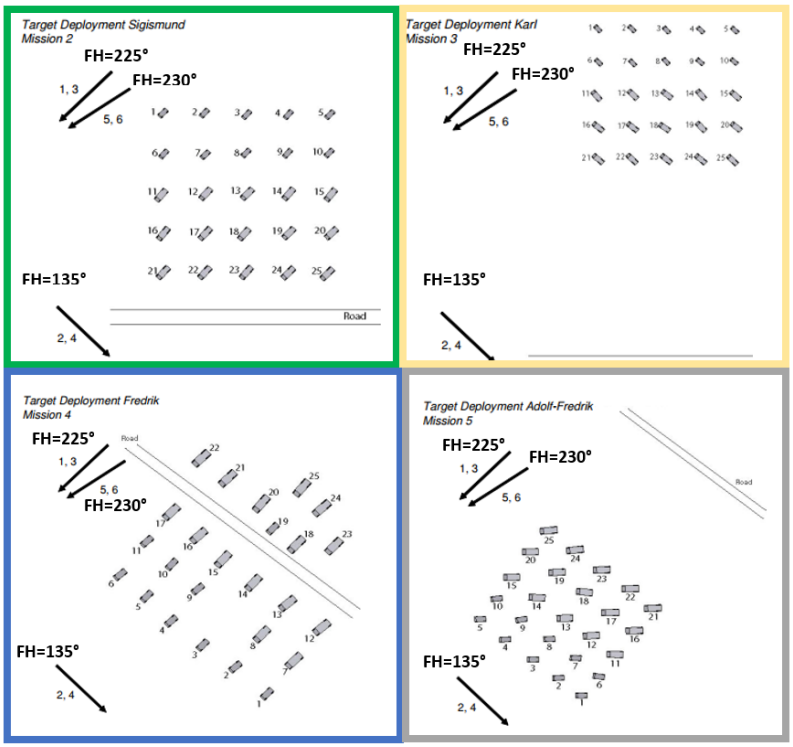


(a) Target deployment presentation and relative orientation compared to the flight headings adapted from [16]

(b) TGB11

(c) TGB30

(d) TGB40

Figure 8.8: (a) Target deployments and representation of flight headings for each target deployment. (b) TGB11 vehicle, (c) TGB30 vehicle and (d) TGB40 vehicle from [16]

First, we create 3 sets of 8 images (each set corresponds to a flight heading), each of them containing the different target deployments. Therefore, for each target deployment, we will generate 3 FBR images corresponding to each flight heading and evaluate the gain of using several acquisitions compared to a bi-date based framework for each flight heading. Then, we will consider an azimuthal symmetry of the environment and gather the data from flight heading 225 and 230° to generate a set of 16 images. One FBR image will be computed and used for change detection with the images acquired with flight heading 225 and 230 °. In that way, we want to evaluate the gain in detection compared to a framework with the same flight heading. Finally, we will exploit the whole set of 24 images to generate an FBR image and evaluate the impact on the detection. The table that summarizes images name for each configuration is presented in Appendix C.1.

### 8.3.2 Detection using same flight heading

First, three FBR images are computed for each flight heading. We present in Figure 8.9 , one image of the stack acquired with FH=135° and the associated FBR image for FH=135°. We recall that targets are present for each of the 8 SAR images for each flight heading. As we can observe in Figure 8.10, the scene is indeed free of targets within the target deployment areas framed in red (for target deployment 2 and 3) and white (for target deployment 4 and 5).

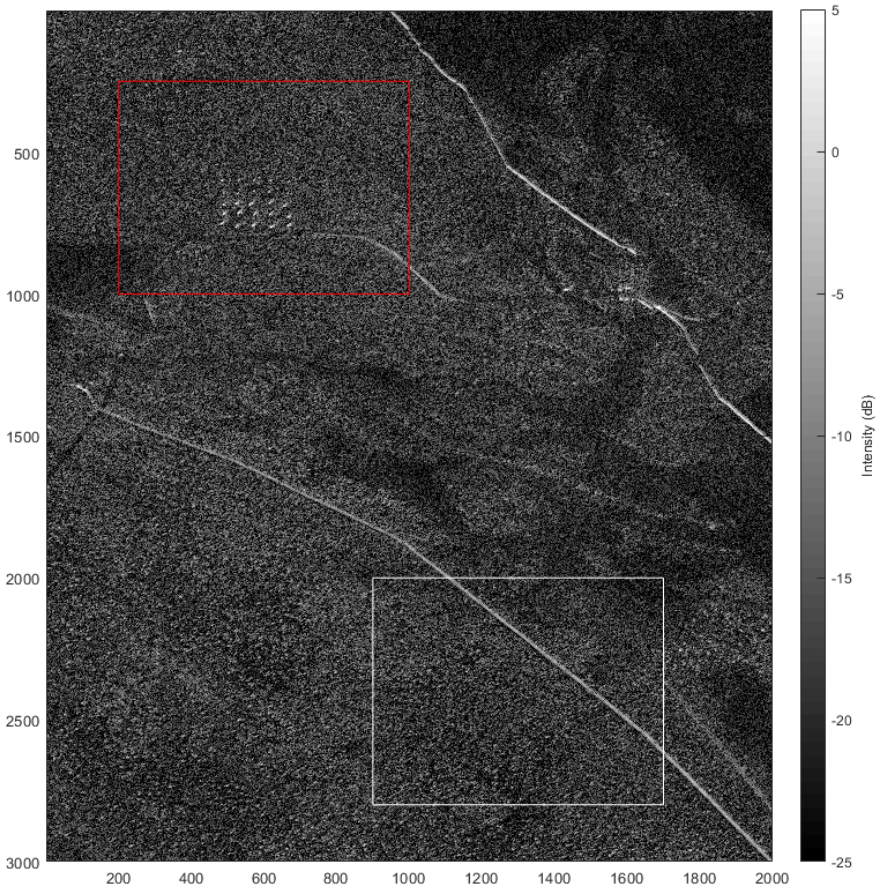


Figure 8.9: HH Image with vehicles *v02_2_2_1.a.Fbp.RFcorr.Geo.Magn*

We present some examples of detection for target deployment 2 (framed in green in Figure 8.8a) for bi-date case and the FBR detection case. The results are presented for 2 orthogonal flight headings to observe the impact of the orientation of targets compared to the radar flight heading. The raw output of the detectors are shown in Figure 8.11 for $FH = 135°$ and $FH = 230°$. We can see the impact of the orientation of targets compared the flight heading. Indeed, the targets

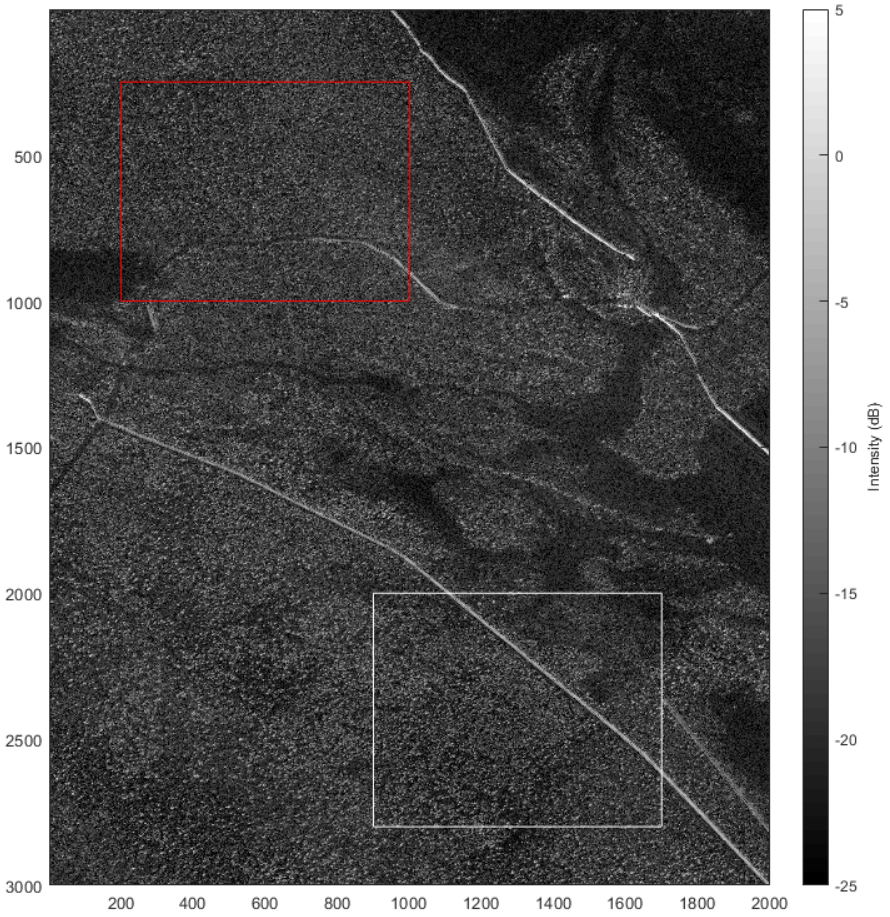


Figure 8.10: FBR Image for FH=135°$FBR_{135}$ (computed with 8 images)

are parked in parallel to the flight heading $FH = 230$, so a bigger metallic area is subject to the emitted waves. In contrast, for $FH = 135°$, the targets are parked in the orthogonal direction compared to the flight path, so the radar sees potentially a smaller surface.

Indeed, we can see a smaller RCS change monitored for targets in the top part of Figures 8.11a and 8.11b compared to Figures 8.11c and 8.11d. Regarding the clutter cancellation, we can see the benefit of FBR CD compared to the bi-date case where bright points can be observed around the targets that may lead to false alarms.

In the proposed challenge paper, the output of the detector is processed afterward with a CFAR filter to decrease the number of false alarms. Besides, for the probability of detection, the rule is to validate the detection if at least one pixel is detected as target in a radius of 10m according to the ground truth. For this study, we will directly consider the raw output of the detection to evaluate

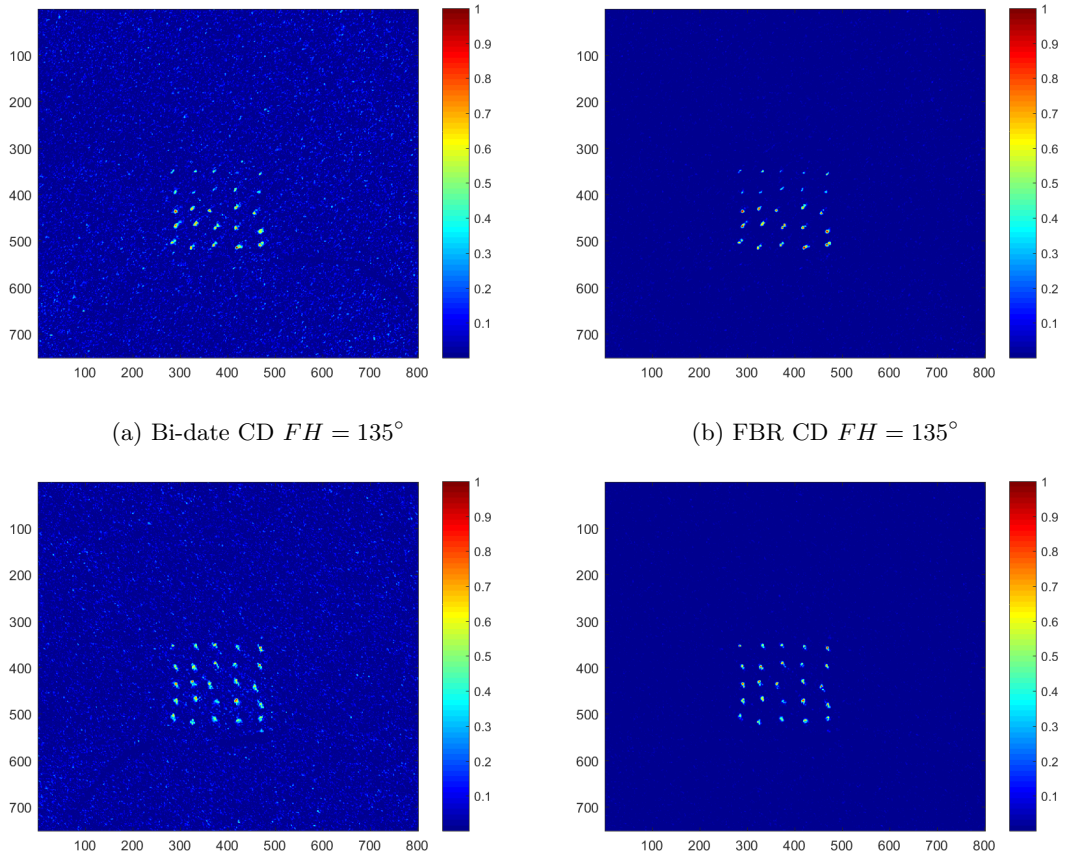

(a) Bi-date CD $FH = 135°$

(b) FBR CD $FH = 135°$

(c) Bi-date CD $FH = 230°$

(d) FBR CD $FH = 230°$

Figure 8.11: Change detection raw output for target deployment 2: bi-date CD and FBR CD for two different flight headings $FH = 135°$ and $FH = 230°$. (a) Bi-date CD *v02_2_2_1.a.Fbp.RFcorr.Geo.Magn* vs *v02_4_2_1.a.Fbp.RFcorr.Geo.Magn* , (b) FBR CD with *v02_2_2_1.a.Fbp.RFcorr.Geo.Magn* (c) Bi-date CD *v02_2_5_1.a.Fbp.RFcorr.Geo.Magn* vs *v02_4_5_1.a.Fbp.RFcorr.Geo.Magn* (d) FBR CD with *v02_2_5_1.a.Fbp.RFcorr.Geo.Magn*. Averaging window (N=3x3)

the comparison between a bi-date framework and the FBR proposed framework. In addition we use the ground truth provided by the dataset with a radius of 5 meters around the center of the targets. The procedure for the detection evaluation will be the same as in the TROPISAR mission study, a pixel-based detection evaluation. In the Figure 8.12 we can observe the overall detection result for each flight heading between the FBR framework and a bi-date framework. Each curve represents the detection performance for 200 vehicles (8x25 vehicles per flight heading). At $PFA = 10^{-3}$ the curves shows that PD=0.6 to 0.7 for the bi-temporal tests depending on the flight heading and reaching in all cases PD=0.9 for the FBR detection of each flight headings. It is an interesting improvement on the detection that have been observed earlier in the case of TROPISAR mission. For a next step, we want to build an FBR image using two flight headings dataset $FH = 225°$ and $FH = 230°$ and evaluate visualy and quantitatively the gain in detection and impact on the false

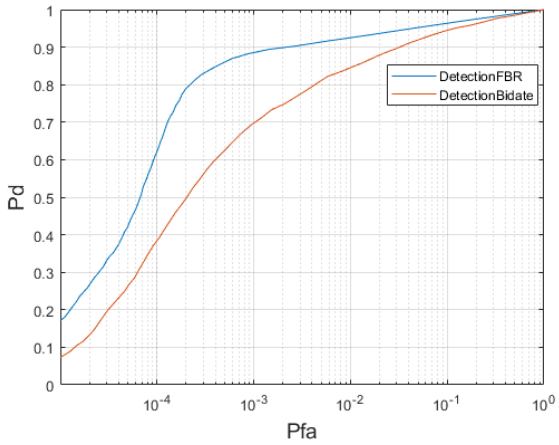


(a) ROC $FH = 135°$

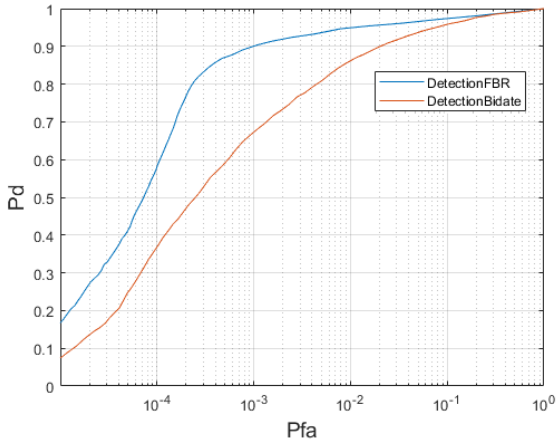


(b) ROC $FH = 225°$

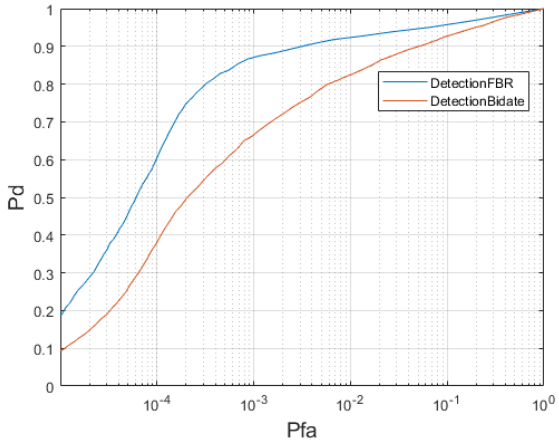


(c) ROC $FH = 230°$

Figure 8.12: Overall ROC (Receiver Operating Characteristic) curves per flight heading for a bi-date framework CD and FBR CD : (a) ROC for FH=135°, (b) ROC for FH=225°and (c) ROC for FH=230°

alarms.

### 8.3.3 Considering two datasets with close FH

We present in this part the results obtained by computing a FBR image from different flight headings. The FBR image is computed only with two close flight heading (225° and 230°).

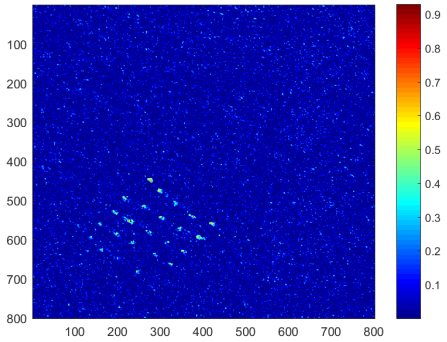


(a) Bi-date CD $FH = 225°$

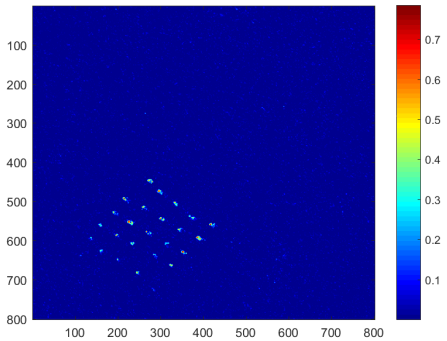


(b) FBR(computed with $FH = 225°$) CD

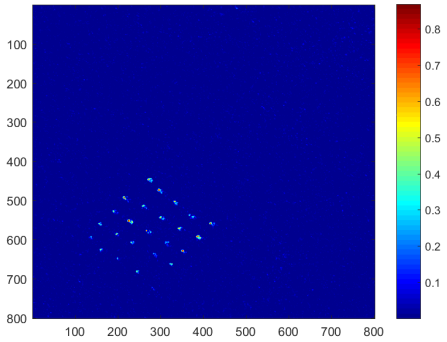


(c) FBR(computed with $FH = 225°$ and $FH = 230°$) CD

Figure 8.13: Change detection raw output for target deployment 5: bi-date CD and FBR CD for $FH = 225°$. (a) Bi-date CD *v02_5_3_1.a.Fbp.RFcorr.Geo.Magn* vs *v02_3_3_1.a.Fbp.RFcorr.Geo.Magn*, (b) FBR ($FH = 225$) CD with *v02_5_3_1.a.Fbp.RFcorr.Geo.Magn*, (c) FBR ($FH = 225$ and $FH = 230$ ) CD with *v02_5_3_1.a.Fbp.RFcorr.Geo.Magn*

We present some examples of raw output detection for the target deployment 5 (framed in grey in the Figure 8.8). In this example, we show the raw output detection in a bi-date case using $FH = 225°$, a FBR detection using the FBR image computed only for $FH = 225°$ and the detection using the FBR image computed with $FH = 225°$ and $FH = 230°$. As we can see in Figure 8.13, both FBR detection visually highlights the targets even though they are mixed with the clutter in bi-date case in Figure 8.13a. This configuration of target is, as presented earlier, tilted compared to the flight headings (vehicles not parked in parallel or perpendicular with respect to the flight paths) so the detection is naturally less efficient because the double bounces are theoretically not coming back to the radar. Indeed, the targets are, in average, more challenging to see in this configuration as we can observe in Figure 8.13. We present the overall ROC curve for the four target deployments in a bi-date CD framework monitored at $FH = 225°$, a FBR framework computed with only $FH = 225°$ and a FBR framework computed with $FH = 225°$ and $FH = 230°$. The detection evaluation is performed with the 8 images of the stack monitored at $FH = 225°$.

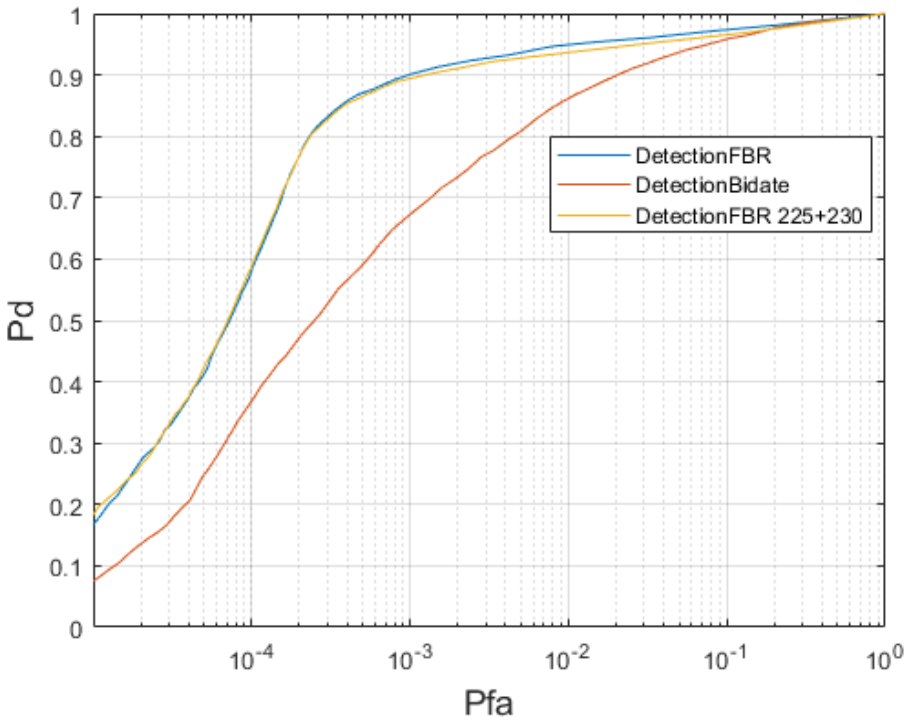


(a) ROC $FH = 225°$

Figure 8.14: Overall ROC (Receiver Operating Characteristic) curves for $FH = 225°$. For a bi-date framework CD in red, FBR CD (FBR image computed with $FH = 225°$) in blue and FBR CD (FBR image computed with $FH = 225°$ and $FH = 230°$ in yellow

As we can observe from the ROC curves in figure 8.14, the overall detection on the 200 vehicles using $FH = 225°$ and $FH = 230°$ is not better than the FBR framework using only $FH =$

225°. We can observe a slight degradation of detection from PFA= $10^{-3}$ and PFA= $10^{-1}$. In general the detection stay better than a bi-temporal consideration however, in that case, bringing more information from another close flight heading does not improve the detection compared to a detection using the same flight heading.

### 8.3.4 Considering heterogeneous flight headings

In this example, we propose to generate FBR images considering the possible flight headings combinations and evaluate the impact on the overall detection. The detection evaluation is again performed with the set of 200 vehicles monitored for FH=225°. In Figure 8.15 is represented the results considering this time two addiotionnal cases: a FBR image computed with FH=225° and FH=135° and the FBR image considering the three flight headings. From the ROC curves in Figure 8.15, we can observe, for the curve in green, a degradation of the detection when only two orthogonal flight headings are considered to generate the FBR image (16 images). Conversely, when the whole flight headings are considered (purple curve) the detection results are equivalent to the one obtained for the two close flight headings.

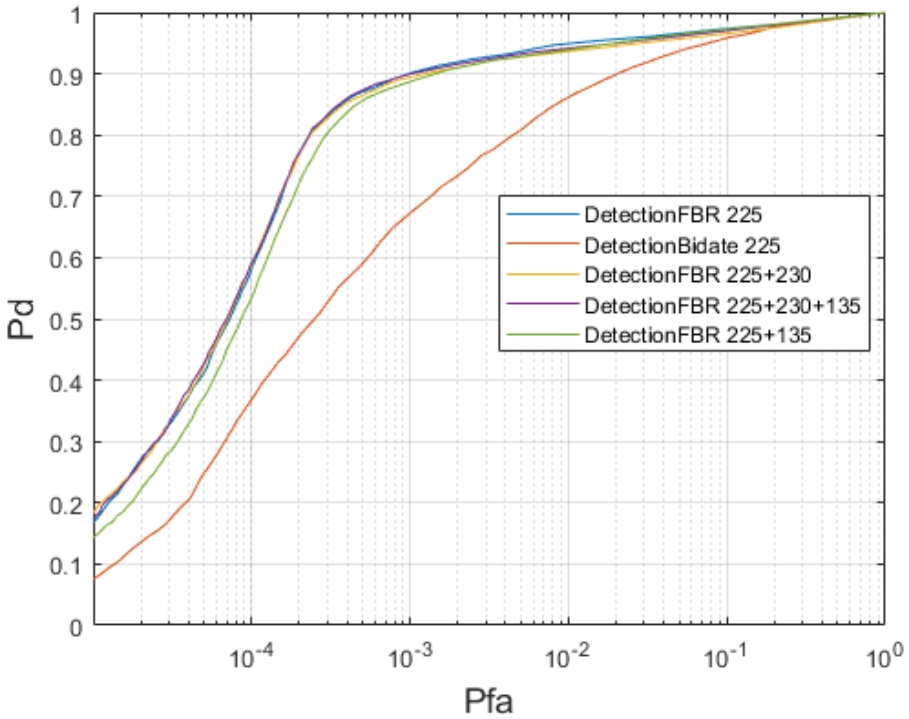


(a) ROC for dataset with $FH = 225°$

Figure 8.15: Overall ROC (Receiver Operating Characteristic) curves for $FH = 225°$. For a bi-date framework CD in red, FBR CD (FBR image computed with $FH = 225°$) in blue, FBR CD (FBR image computed with $FH = 225°$ and $FH = 230°$) in yellow, FBR CD (FBR image computed with all FH) in purple and FBR CD (FBR image computed with $FH = 225°$ and $FH = 135°$)

### 8.3.5 Example of detection with azimuthal symmetry /asymmetry

Finally, we present a change map obtained between the FBR image computed with the three flight headings and an image from the set FH=135°(mission 3). As we can observe here, where the environment is mostly composed of forest, the hypothesis of azimuthal symmetry is well respected. Indeed, we do not observe changes in forest areas except where the targets are present circled in orange. However, the hypothesis of symmetry is transgressed as we can see along the forest borders and roads producing a change pattern circled in green. It is a well-expected result that can be a problem in case of automatic change detection because false alarms are increased due to the azimuthal asymmetry property of structures.

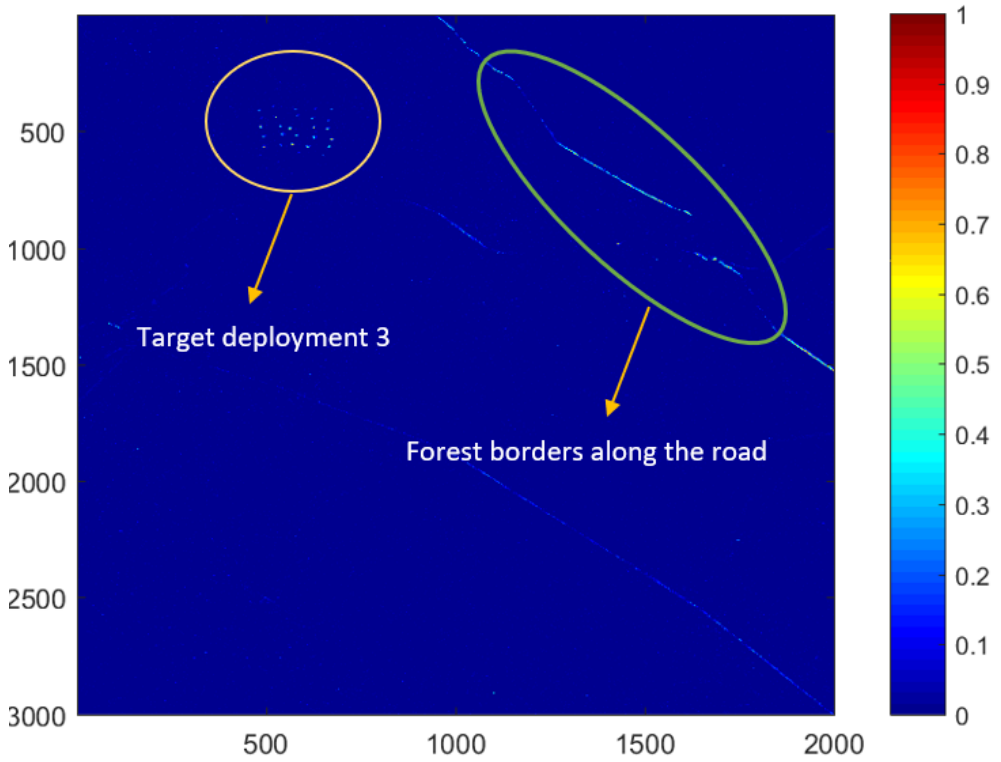


(a) Change map for $FH = 135°$

Figure 8.16: Change detection output between a FBR image computed with the whole dataset (24 image containing 3 flight headings) and an image of target deployment 3 from the set acquired at $FH = 135°$. Problems of detection where azimuthal symetry is not respected : example of a detection between the FBR image computed combining the 3 flight headings and one image with FH=135°

### 8.3.6 Discussion

For this challenge dataset, we were interested in benefiting from the different configurations of acquisition to evaluate if a gain of detection was noticed compared to a change detection involving a single reference image and a mission image. Considering flight headings separately, the gain in the detection of vehicles is well improved when using FBR frameworks thanks to an efficient clutter cancellation. Visually, the targets are well highlighted and the computed ROC curves showed an improvement compared to a bi-date framework for each flight heading. Afterward, we built the FBR image from the set of two close flight heading acquisitions and evaluated the detection gain. According to the results, the use of more images computed with a close flight heading still improves the detection compared to a bi-date detection. However, it does not improve the overall detection compared to a FBR framework considering a single flight heading at 225°. Considering strongly heterogeneous flight headings still enables better detection compared to a bi-date case, but it decreases overall performance. It seems experimentally possible for this type of forest (long thin trunk) to consider an azimuthal symmetry of the environment and use different flight heading to compute change detection to highlight vehicles under foliage. However, this assumption is naturally true in forest environment. It generates false alarms where the azimutal symmetry is not respected near roads or forest borders.

**Summary** : In this chapter, we approached the problem of FoPen applications. P-band measurements above tropical forest and VHF measurements above a sparse Scandinavian forest have been studied to evaluate the benefit of FBR framework. The clutter cancellation has been successful in TROPISAR mission, giving better detection and decreasing the number of false alarm compared to a bi-date detection framework. We also observed the same improvement in a sparse Scandinavian forest. In this work, we tried to combine different flight heading to highlight the possible improvement in the detection. In areas where the azimuthal symmetry is respected, we can see for this example that we can combine different images to generate a FBR image without significant risks on the detection (but without important improvement also). However combining flight headings produces detection problems in areas where the azimuthal symmetry is not respected for example near the borders of forests or along roads.

# Conclusion and perspectives

## Conclusion

The first objective of this thesis has been to develop a methodology producing a change map that highlights possible targets present within a given SAR acquisition by benefiting from SAR time-series. As illustrated, change detection techniques represent a good opportunity to highlight targets in environment such as harbor areas or forests observed at low frequencies thanks to the cancellation of the strong backscattering signals of the surrounding background.
Considering that target-free SAR images are not available in practice in open-access data, our idea was to benefit from available time-series to generate a scene that consists only of the static background. We denoted this image the Frozen Background Reference image that aimed to represent the temporally homogeneous background in the scene such as buildings, trees, infrastructures, and the clutter noise. This image does not correspond to an actual SAR acquisition but represents an acquisition that would have been acquired without ephemeral targets.
We use afterward this image to visualize the signature of possible targets at a given acquisition.

### Summary of the chapters

The first part constituted of three chapters, presented the key aspects of SAR images, the presentation and the preparation of data used for multi-temporal analysis as well as the main challenges encountered in SAR time-series change detection techniques in the frame of target detection.
In the second part, we introduced the methodology used to generate the FBR image. Chapter 4 focused on the temporal behavior analyses of pixels in SAR time-series and pixels' selection strategy representing a homogeneous temporal behavior to build our FBR image. Chapter 5 illustrated the pixel selection method with different examples and investigated the impact of the number of images used to generate the FBR image. Chapter 6 presented possible change detection strategies from this FBR image, depending on the introduced pixel selection methods. Considering a random selection of remaining pixels does not influence the detection capabilities. We could observe that

the contribution of all remaining candidate pixels improves the detection significantly in the case of low SNR.

Performing a change detection from this FBR image provides different advantages. First, the possible misinterpretations when ephemeral targets overlap in time are avoided, and the resulting change map corresponds to the actual content of ephemeral objects present at a given acquisition. This aspect has been illustrated in chapter 7 for the detection of vessels and ships in the industrial harbor between Jurong Island and Singapore. The second advantage is the promising clutter cancellation obtained by benefiting from the contribution of all remaining homogeneous candidate pixels. It has been illustrated in chapter 8 for the detection of targets concealed under the canopy. The change detection accuracy depends on the computed FBR image. Considering time-series with a long time span increases the possibility that a permanent change occurred, especially in urban areas, such as infrastructure or building construction/deconstruction. For forest environments, the impact of temporal decorrelation and growth of the vegetation has to be taken into account when computing the FBR image for future studies. We saw indeed at low frequencies over a short acquisition period that the method was successful in highlighting targets.

# Perspectives

## Technical perspectives

This thesis has developed a new approach for change detection based on a fictive SAR image, empty of mobile targets. To do so, we have defined three main steps: the selection of the temporally stable pixels, the formation of the fictive SAR image, and the detection of changes between this image and any other collected SAR image. Each of these steps can be further investigated, improved, or at least modified.

### Selection of stable pixels

The pixels we want to select have to be temporally stable. In this study, we have chosen to use the variation coefficient for a Rayleigh-Nagakami law to select these pixels, meaning that we rely on the amplitude of these latter.

We have seen that a theoretical value for this variation coefficient $CV_{theo}$ can be derived for stable zones to define a threshold to select the stable pixels. The standard deviation of this value decreases with $\sqrt{D}$, $D$ being the number of dates in the SAR time-series. Ideally, the larger is the number of dates, the better is the estimation of $CV_{theo}$. This quantity is theoretically independent

of the frequency and the polarization.

Practically, how many dates do we need at a minimum? Is there a maximum? We have slightly investigated this question in this Ph.D. study, partly because of the reduced number of time-series at our disposal.

We have seen that 30 images were necessary for the Singapore region observed with Sentinel-1 (C-band), while 20 images were sufficient for the area of San Francisco seen with UAVSAR at L-band. Besides, to establish these results, we have studied the error between different FBR images. But this detection test expression varies depending on how to select the pixels to form the final image. In the example quoted just above, the candidate pixels have been averaged. Would it have an impact on the number of required dates if we choose the random selection?

* * *

As far as the polarization is concerned, the selection is made in parallel for each channel. We could develop a way to perform this selection by considering these channels simultaneously. We could, for instance, investigate the temporal stability of the polarimetric signatures.

* * *

Finally, we have illustrated a single way to define these stable pixels. Our initial goal was to remove mobile objects, such as vehicles, in urban areas. Construction or destruction of buildings may induce variations that may spoil our detection. In other environments like forests, we could observe seasonal effects if the time-series are long. We studied short time-series over forests, and we did not face these kinds of variations. It would be essential to study these configurations, as they would undoubtedly impact the selection process. For instance, we could define consecutive sets of temporally stable pixels, each set corresponding to a particular temporal sequence. For this purpose, it is crucial to build data sets, including a detailed ground truth of the scene over observation.

**The formation of the fictive SAR image**

Once the candidate pixels have been selected, we have to form the SAR image representing the stable background for each azimuth and range. This study illustrated this step with two different methods: the averaging of the candidate pixels or the random selection among these candidate pixels. The first impact can be directly seen in the distribution of the intensity of these two images. In the so-called ”random” case, we preserve the statistic distribution, while in the averaging case, this distribution is squeezed. Intuitively, we expect that the ”random” case leads to a fictive SAR

image that can be directly exploited, as any other regular SAR image. We have tested its use in change detection, but this assumption must be checked for other applications. For instance, it would be interesting to extend our study to polarimetry or interferometry, if possible, to analyze the physical consistency of this fictive image. In the case that we consider all the remaining pixels, the advantage is obvious. Visually, the resulting SAR image has been strongly denoised, and it is then possible to better detect smaller features. However, the use of the detection test is more tricky because the number of pixels involved for the detection is varying from a pixel to another. Concerning the physical meaning of the resulting image, the question holds; again, it would be important to analyze, for instance, the polarimetric signature of stable scatterers to check for their physical consistency.

These two ways of producing the fictive image are two examples that can be replaced by other methods. We can change the process to select the pixels or to perform the average, for instance.

#### The detection of changes

In this study, our goal was to detect changes in noisy environments using SAR images. We have shown that it was possible to improve detection performances compared with classical bidate solutions significantly. As discussed above, future studies may be conducted to adapt these strategies, either to a varying background or to detect variations that cover a more extended time. It will have a direct consequence on the strategy to select the candidate pixels.

In the case of varying backgrounds, two types of variations can be considered. First, this variation is predictable as it is for seasonal changes. In that case, a background image may be constructed "per season." As an example, for maritime environments, we could study how to deal with strong tidal effects. In the second case, the background change is not predictable. A possible objective would be to integrate these changes in a continuous mode to update the reference image regularly. The literature in video surveillance applications might be an interesting source of methodologies to consider due to the forthcoming short revisit time expected for SAR monitoring systems.

### Extension to other applications or to other environments

#### Application to other environments

In this thesis, we focused on the detection of mobile targets, whatever the environment. In practice, with our data sets, we studied two harbor areas and a forest. For the latter, the short period between the first and the last acquisition did not permit us to investigate the effect of additional

changes - with different temporalities - on target detection.

Forest would be an interesting area to further investigate, but this time over a long period to test the robustness of our method. For instance, is it still possible to detect vehicles through foliage, whatever the seasonal changes? To do so, we would have to work with L-band data, like ALOS, to manage to deal with quite long time-series. We can also expect that higher frequencies (X-band with TerraSAR-X) could be exploited with our method for target detection. Indeed, if a vehicle may be placed within a forest, it means that the tree density may be locally sparse. Also, relying on the changes in tree crowns, we could expect to remove their signature.

* * *

In other areas, like deserts, we can expect to see no changes, whatever the length of the time-series. However, because of the high penetration capabilities through sand, we can expect to detect subsurfaces changes reflecting the presence of potential water ressources as in [99]. The use of different frequencies may be introduced to generate different reference images. For instance, we expect that high frequencies (Sentinel-1 at C-band for instance) would give an information related to the surface or upper subsurfaces of the ground whereas lower frequencies would characterize sub-surfaces since it can penetrate deeper through dry sand. The detection of changes at different frequencies may give information on the possible subsurface activity such as water channel activation. However, this will imply some technical issues linked to the differences in the acquisition geometry.

**Other applications**

In this thesis, we focused on small and ephemeral targets. We could adapt our method either to larger but still ephemeral targets (like flooding), to small but longer changes (like the survey of illegal constructions or the progressive deterioration of protected buildings), and to larger and longer changes (like fires or earthquakes) to provide change maps.

* * *

Another group of applications is linked to the use of the FBR image only. Indeed our method provides a SAR image with a clutter potentially significantly lowered while keeping the resolution. Also, all the permanent structures are highlighted, leading to a tool that could be used to provide a cartography of the roads and the buildings of a given area.

With Sentinel-1 archives, we can also imagine a tool to image very slow changes comparing

FBR images computed each year, over all the SAR images available in this time slot. It can be the progression of desert areas or changes along the coasts due to increased water level.

# Contributions and collaborations

## Contributions

### Journals

• T. Taillade, L. Thirion-Lefevre, R. Guinvarc'h, "Detecting Ephemeral Objects in SAR Time-Series Using Frozen Background-Based Change Detection". Remote Sens. 2020, 12, 1720

### Conference proceedings

• T. Taillade, L. Thirion-Lefevre and R. Guinvarc'h, "L-band Polarimetric Change Detection on SAR Images: Fire Burn Scars in California," IGARSS 2019 - 2019 IEEE International Geoscience and Remote Sensing Symposium, Yokohama, Japan, 2019, pp. 9956-9959

• T. Taillade, L. Thirion-Lefevre and R. Guinvarc'h, "A New Way for Detecting Man-Made Targets and Structures within Forests using Time Series of Polarimetric SAR images," IGARSS 2020 - 2020 IEEE International Geoscience and Remote Sensing Symposium, accepted.

### Workshops

• T. Taillade, R. Guinvarc'h, L. Thirion-Lefevre. "A new framework for polarimetric change detection in time series SAR images: the empty scene." ASC/CSA Advanced SAR workshop, 2019, Saint-Hubert, Canada

## Collaborations

• 3 months research stint at CRISP laboratory (Center for Remote Imaging and Processing) in NUS (National University of Singapore) on the detection of fire burn scars using SAR images.

# Appendix A: Sentinel 1 revisit time around the world

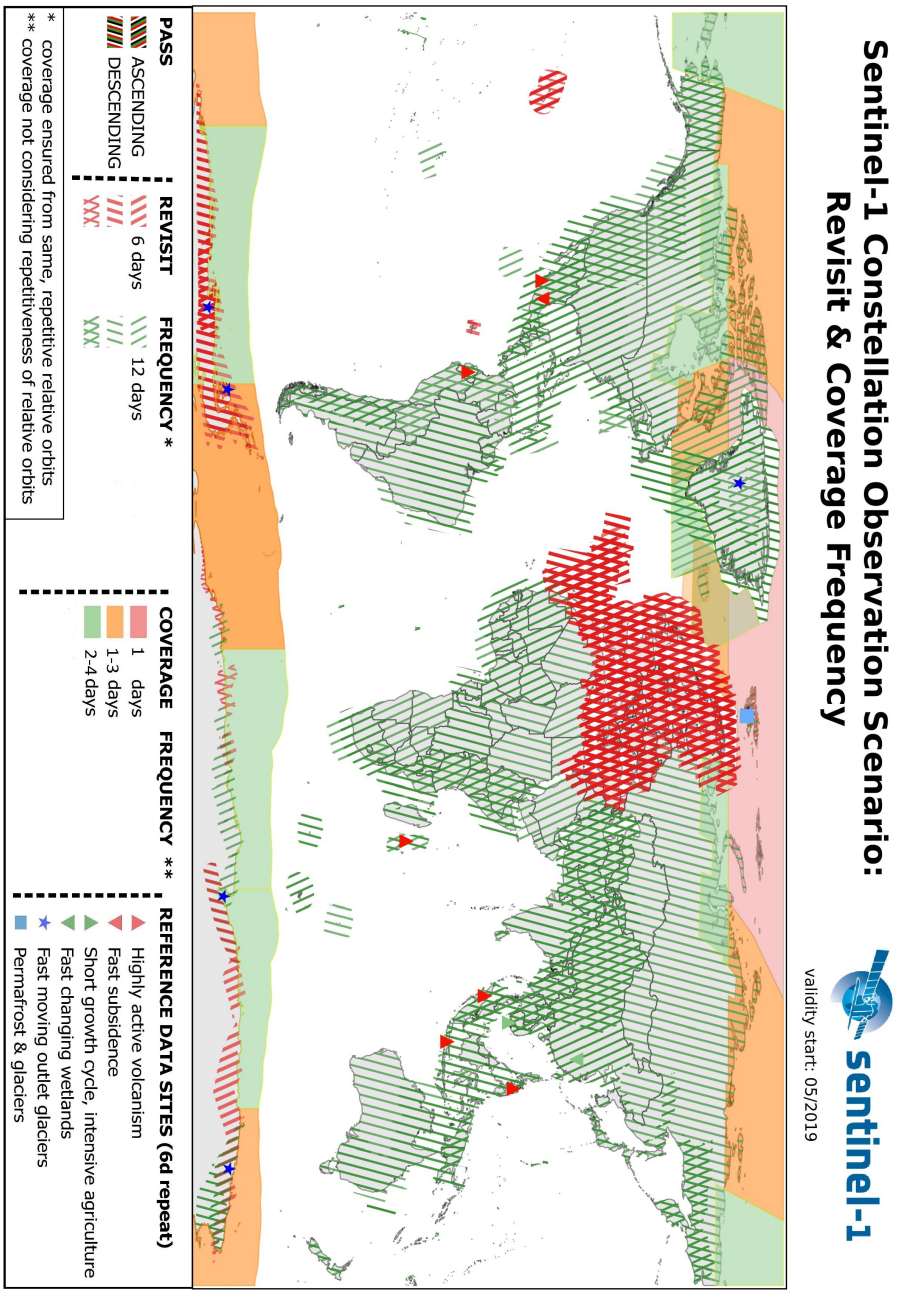


Figure A.1: Revisit time and acquisition mode of Sentinel 1 constellation (2019)

# Appendix B: Industrial Harbor monitoring

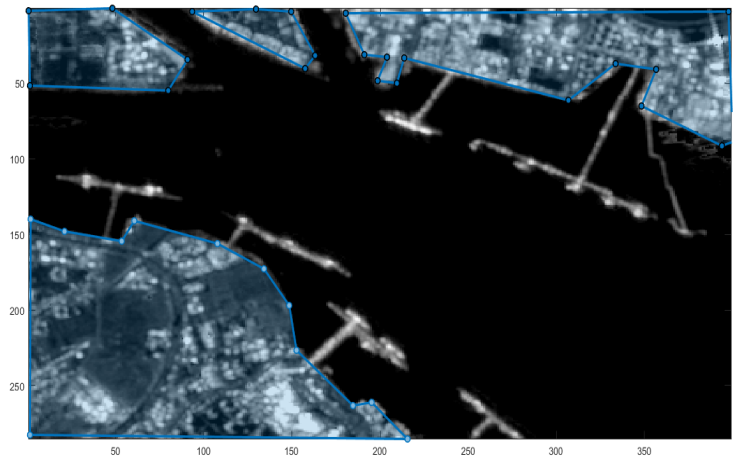


Figure B.1: Mask used to exclude change from the land.

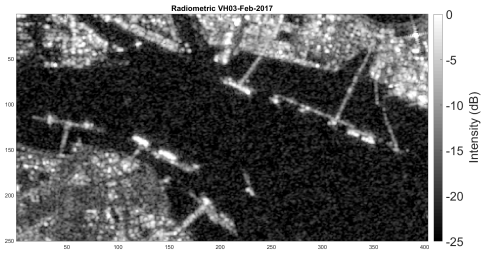


(a) Date 1 : 3 February 2017

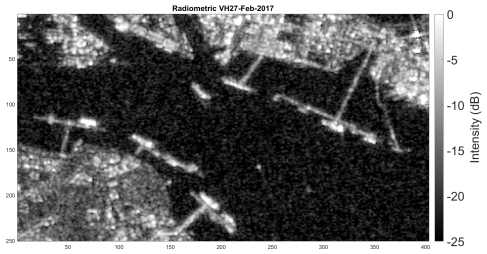


(b) Date 2 : 27 February 2017

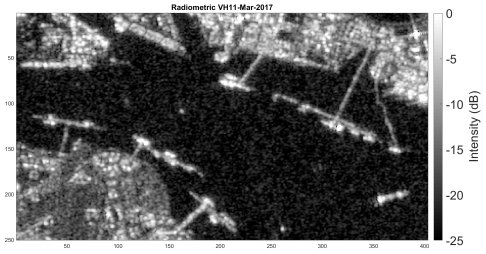


(c) Date 3 : 11 Mars 2017

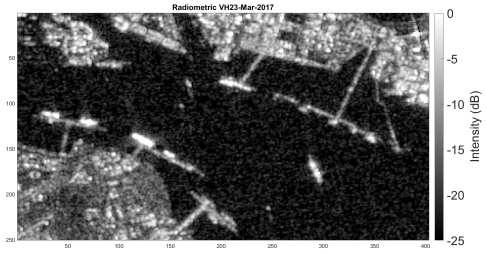


(d) Date 4 : 23 Mars 2017

Figure B.2: 4 first Images HV of the stack (15 February 2017 missing): (**a**) 3 February 2017, (**b**) 27 February 2017, (**c**) 11 Mars 2017, (**d**) 23 Mars 2017 (Sentinel 1 GRD images)

# Appendix C: CARABAS II Challenge table

| Image file name | Flight Heading (deg) | Incidence Angle (deg) | RFI | Deployment | Forest Site | Target heading (deg) |
|---|---|---|---|---|---|---|
| | | | 0=Low 1=High | | | |
| v02_2_1_1.a.Fbp.RFcorr.Geo.Magn | 225 | 58 | 1 | Sigismund | 2 | 225 |
| v02_2_2_1.a.Fbp.RFcorr.Geo.Magn | 135 | 58 | 0 | Sigismund | 2 | 225 |
| v02_2_3_1.a.Fbp.RFcorr.Geo.Magn | 225 | 58 | 1 | Sigismund | 2 | 225 |
| v02_2_4_1.a.Fbp.RFcorr.Geo.Magn | 135 | 58 | 0 | Sigismund | 2 | 225 |
| v02_2_5_1.a.Fbp.RFcorr.Geo.Magn | 230 | 58 | 1 | Sigismund | 2 | 225 |
| v02_2_6_1.a.Fbp.RFcorr.Geo.Magn | 230 | 58 | 1 | Sigismund | 2 | 225 |
| v02_3_1_2.a.Fbp.RFcorr.Geo.Magn | 225 | 58 | 1 | Karl | 2 | 315 |
| v02_3_2_1.a.Fbp.RFcorr.Geo.Magn | 135 | 58 | 0 | Karl | 2 | 315 |
| v02_3_3_1.a.Fbp.RFcorr.Geo.Magn | 225 | 58 | 1 | Karl | 2 | 315 |
| v02_3_4_1.a.Fbp.RFcorr.Geo.Magn | 135 | 58 | 0 | Karl | 2 | 315 |
| v02_3_5_2.a.Fbp.RFcorr.Geo.Magn | 230 | 58 | 1 | Karl | 2 | 315 |
| v02_3_6_1.a.Fbp.RFcorr.Geo.Magn | 230 | 58 | 1 | Karl | 2 | 315 |
| v02_4_1_1.a.Fbp.RFcorr.Geo.Magn | 225 | 58 | 1 | Fredrik | 1 | 225 |
| v02_4_2_1.a.Fbp.RFcorr.Geo.Magn | 135 | 58 | 0 | Fredrik | 1 | 225 |
| v02_4_3_1.a.Fbp.RFcorr.Geo.Magn | 225 | 58 | 1 | Fredrik | 1 | 225 |
| v02_4_4_1.a.Fbp.RFcorr.Geo.Magn | 135 | 58 | 0 | Fredrik | 1 | 225 |
| v02_4_5_1.a.Fbp.RFcorr.Geo.Magn | 230 | 58 | 1 | Fredrik | 1 | 225 |
| v02_4_6_1.a.Fbp.RFcorr.Geo.Magn | 230 | 58 | 1 | Fredrik | 1 | 225 |
| v02_5_1_1.a.Fbp.RFcorr.Geo.Magn | 225 | 58 | 1 | Adolf-Fredrik | 1 | 270 |
| v02_5_2_1.a.Fbp.RFcorr.Geo.Magn | 135 | 58 | 0 | Adolf-Fredrik | 1 | 270 |
| v02_5_3_1.a.Fbp.RFcorr.Geo.Magn | 225 | 58 | 1 | Adolf-Fredrik | 1 | 270 |
| v02_5_4_1.a.Fbp.RFcorr.Geo.Magn | 135 | 58 | 0 | Adolf-Fredrik | 1 | 270 |
| v02_5_5_1.a.Fbp.RFcorr.Geo.Magn | 230 | 58 | 1 | Adolf-Fredrik | 1 | 270 |
| v02_5_6_1.a.Fbp.RFcorr.Geo.Magn | 230 | 58 | 1 | Adolf-Fredrik | 1 | 270 |

Figure C.1: Summary table of CARABAS II challenge

# Appendix D: Résumé étendu en Français

## D.1 Cadre de l'étude

Cette thèse porte sur la détection de changements dans les images SAR (Synthetic Aperture Radar) pour la détection de cibles, principalement dans des environnements à forte réflectivité tels que les forêts observées à basses fréquences radar, les villes ou les zones portuaires. Nous souhaitons détecter les changements associés aux objets potentiellement mobiles tels que les véhicules ou les bateaux. Dans ces configurations, la détection des cibles est difficile en raison du fort signal de rétrodiffusion des structures naturelles ou artificielles environnantes.

Une première option pour la détection repose sur l'utilisation d'une seule image SAR. Dans ce cas, différentes approches permettent de mettre en évidence la cible si elle possède des caractéristiques différentes de son environnement [3, 2, 4, 92, 100].

Une autre stratégie peut être utilisée pour la détection de cible, basée sur la détection de changement entre deux images SAR ou plus. Dans ce cas, à supposer qu'une image sans cible soit disponible, la détection de changement entre cette image SAR (image de référence) et une autre image SAR (image "mission") avec d'éventuelles cibles permet de supprimer la contribution de l'environnement et met en évidence les cibles d'intérêt [6, 33, 1].

La détection de changement est appropriée pour mettre en évidence les cibles dans une scène observée contenant des forts diffuseurs car la contribution de l'environnement est supprimée. Cependant, le choix des stratégies de CD implique d'avoir idéalement accès à une scène sans cible. Des campagnes spécifiques pour la détection de cibles peuvent fournir de telles scènes et une vérité terrain détaillée qui permet d'évaluer la détection. Cependant, dans la pratique, le contenu d'une scène est inconnu pour les images SAR de satellites dont les images sont en libre accès (par exemple, Sentinel 1, UAVSAR). Dans ce cas, les résultats de détection de changement entre deux ou plusieurs scènes peuvent être ambigus si une cible est présente plusieurs jours ou lorsque des cibles de natures différentes occupent la même position géographique lors de plusieurs acquisitions (chevauchement temporel partiel ou total).

Dans cette thèse, nous supposons donc que toute image SAR est constituée d'objets immobiles (ex: bâtiments ou arbres) qui sont présents de manière permanente dans les images SAR et d'objets éphémères (cibles) qui peuvent apparaitre et disparaitre d'une acquisition à l'autre (ex: voitures ou bateaux). Nous proposons d'exploiter des séries temporelles d'image SAR en libre

accès pour générer une image SAR de référence contenant uniquement ce qui est temporellement stable ou permanent. Nous réaliserons ensuite une détection de changement avec cette image FBR pour mettre en évidence les cibles présentes à une acquisition donnée. Avec cette technique, nous espérons pouvoir isoler et analyser la signature des cibles.

## D.2 Organisation du manuscrit

La première partie comprend trois chapitres introduisant les éléments clés pour la compréhension et l'analyse des images SAR, présente les principaux jeux de données utilisés lors de l'étude et enfin illustre les différentes stratégies de détection de changements dans les séries temporelles d'images SAR. La deuxième partie présente le concept d'image FBR, sa construction, sa représentation et les stratégies de détection de changement associée. Enfin, la dernière partie, composée de deux chapitres, présente les applications de notre méthode sur deux environnements contraignants pour la détection de cibles: la surveillance maritime en milieu portuaire et la détection de cibles dans des contextes FoPen.

## D.3 L'imagerie SAR et les enjeux futurs

L'imagerie SAR (Synthétique Aperture Radar) ou RSO (Radar à Synhtèse d'Ouverture) est une technique d'imagerie radar permettant de génrerer une image caractéristique de la rétrodiffusion élétromagnétique des diffuseurs dans une scène observée. Un porteur muni d'un radar (spatio ou aéro-porté) émet des impulsions en se déplaçant et récupère les signaux rétrodiffusés par la scène observée. La diversité fréquentielle apportée par le chirp émit et la diversité angulaire apportée par le mouvement relatif du porteur par rapport à la scène observée permet de reconstruire une image représentant les contributeurs élétromagnétiques de la scène.

Cette technique d'imagerie permet, contrairement à l'imagerie optique, d'obtenir une image qui est indépendante des conditions météorologiques, des conditions de visibilité lié à de possibles nuages de fumée ou encore des conditions de luminosité. C'est une des raisons majeures pour lesquels ce type d'imagerie est très prisé de nos jours. Un autre avantage notable de la technologie SAR est la pénétration dans des milieux tels que la forêt, la neige sèche ainsi que le sable sec. De manière générale, l'utilisation de basses fréquences radar (en dessous de la bande L donc pour des longeurs d'onde supérieur à 30cm) favorise d'autant plus la pénétration en fonction des conditions et des propriétés du milieu observé.

En contrepartie, les image SAR ne peuvent pas être interprétées aussi simplement que les images

optique du fait, d'une part, des considérations physiques intrinsèques à l'environnement et d'autre part à la géométrie d'acquisition. De ce fait, des artefacts peuvent être observés sur les images SAR comme des distorsions ainsi que des signatures multiples d'objets correspondant en réalité a des multiples trajets de l'onde effectués entre différents contributeurs de la scène.
Au cours des dernières années et dans les années à venir, un grand nombre de satellites SAR on été lancés et vont être mis en service à différentes fréquences d'utilisations permettant une couverture quasi "temps réel" de la surface de la terre. Ces images offrent la possibilité d'étudier des phénomènes dans des domaines très variés allant de l'océanographie, l'étude des terres agricoles, l'étude de la biomasse à la surveillance des territoire. Depuis quelques années, l'accessibilité au séries temporelles d'images SAR a été rendu plus facile et permet désormais d'étudier les phénomènes sous un nouveau prisme. A cet effet, les solutions apportées par les contributions liées à l'étude des séries temporelles d'image SAR constituent un enjeu majeure pour les années futures.

## D.4 Détection de changements pour la détection de cibles dans les images SAR

### D.4.1 Les approches pour la détection de changement dans les séries temporelles d'images SAR

A l'heure actuelle, plusieurs approches de détection de changement dans les séries temporelles d'images SAR ont été développées. Nous proposons d'approfondir et étudier deux stratégies fondamentalement différentes. La première est basé sur des approches bi-temporelles. Un test séquentiel ou exhaustif (toutes les combinaisons possibles) entre les combinaisons bi-temporelles de la série est effectué [59, 45, 62]. La seconde stratégie vise à étudier l'homogénéité globale de la série pour décider si un changement s'est produit ou non [76, 77]. Si le but est de dater les ruptures, différentes stratégies sont mises en œuvre pour les extraire.

### D.4.2 Détection de changement pour la détection de cibles

La détection de cibles dans les séries temporelles d'images SAR semble à première vue triviale car nous pouvons associer leur comportement temporel à des changements de type "step" ou des changements impulsifs. Cependant, la détection des véhicules ou des navires devient plus ambiguë dans les zones à forte fréquentation du fait de leur chevauchement spatio-temporel impliquant une comparaison relative et conduisant à une mauvaise interprétation de la détection. Il semble donc plus confortable d'avoir accès à une scène sans cible avec uniquement l'environnement statique pou-

vant être utilisé pour la détection de changement et ainsi améliorer la visualisation, l'interprétation et la détection d'un éventuel objet éphémère pour une acquisition donnée.
D'une part, nous pouvons rencontrer des difficultés à détecter la cible en utilisant une seule image SAR car cette cible peut avoir les mêmes propriétés ou des propriétés proches des objets environnants en arrière-plan. D'autre part, l'utilisation de séries temporelles d'images SAR peut conduire à une mauvaise interprétation due à des cibles éphémères qui se chevauchent dans le temps.
Nous proposons donc de bénéficier des caractéristiques temporelles intrinsèques des pixels pour construire une image de référence appelée image Frozen Background Reference (FBR) qui consistera uniquement en des structures temporellement stables dans la série temporelle. À partir de cette image FBR, la détection de changement peut être effectuée avec n'importe quelle autre image SAR de la scène pour mettre en évidence des cibles éphémères à une date spécifique.

## D.5 L'image FBR: concept et stratégies pour la détection d'objets éphémères

Le but d'une image FBR est de représenter un comportement temporellement stable d'une scène pour une période d'acquisition donnée. Une analogie peut être faite avec les applications de vidéo-surveillance visant à séparer ce qui appartient au fond et les objets apparaissant de manière éphémère. Nous sélectionnons dans la série temporelle à chaque case distance et azimut, un ensemble de pixels qui représentent un comportement temporellement stable de la scène et rassemblons leur contribution dans une image appelée image FBR. Nous souhaitons obtenir une image sans cible éphémères représentant un état stable électromagnétiquement (diffuseurs permanents) et statistiquement (bruit de fond) de la scène. Le schéma général est présenté dans la figure D.1. Le framework prend en entrée une série temporelle d'images SAR, sélectionne les pixels qui sont temporellement homogènes pour chaque case distance et azimuth et calcule l'image FBR. Par la suite, pour toute image SAR, une détection de changement est effectuée pour mettre en évidence les objets éphémères à une date donnée. D'autres stratégies peuvent être basées sur la détection de changement entre des images FBR calculées sur différentes saisons pour obtenir un changement global à une échelle de temps différente (qui serait davantage liée à des changements établis dans le temps). On peut également envisager de mettre à jour l'image FBR en tenant compte du résultat de la détection de changement.

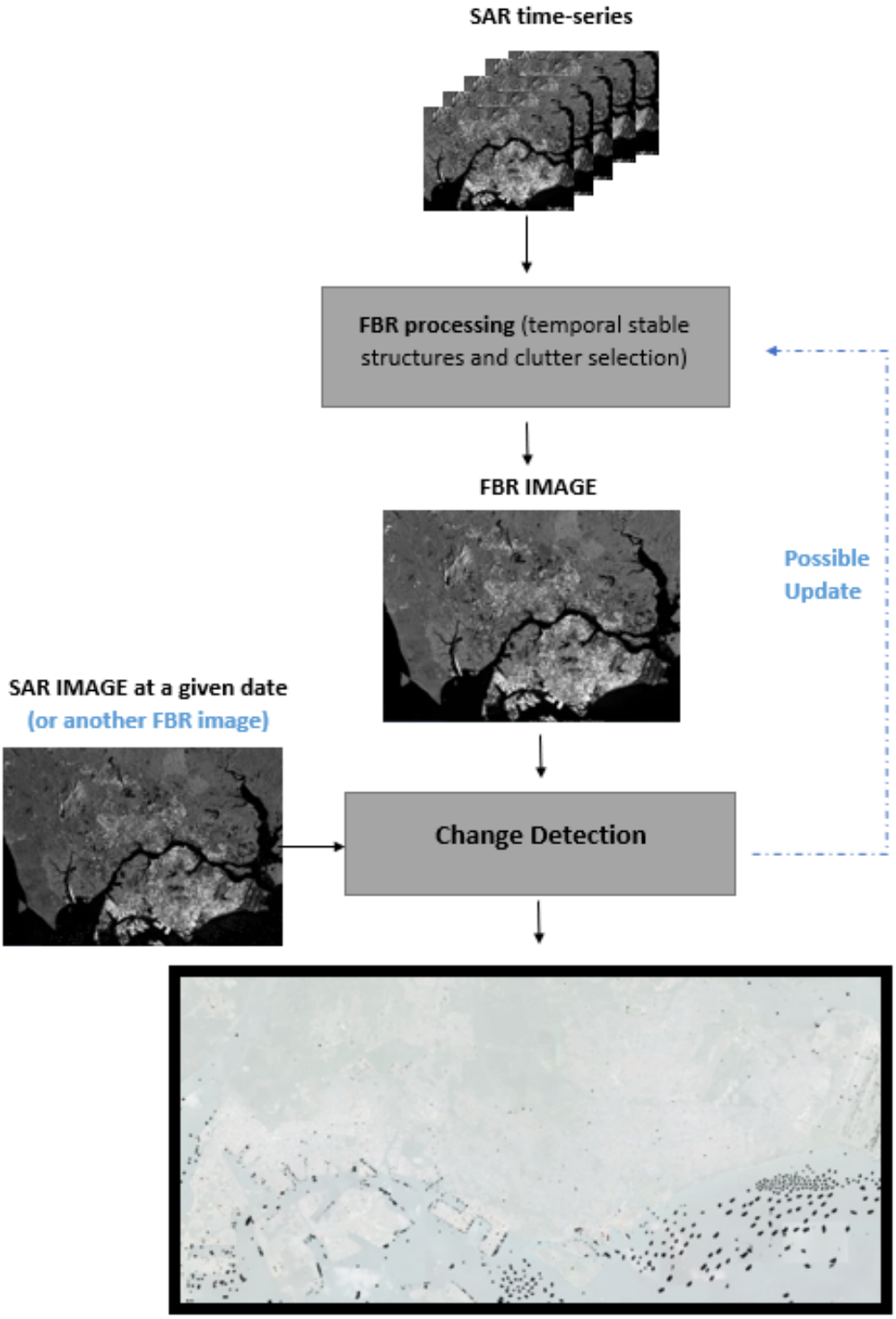


Figure D.1: Illustration du concept de l'image FBR et exemple d'objets détectés le 02 mars 2019 dans la région de Singapour projetés sur Google Earth en arrière-plan: les points noirs représentent les endroit où les changements les plus significatifs se sont produits par rapport à l'image FBR (apparition de bateaux)

### D.5.1 Sélection des pixels temporellement stable et représentation de l'image FBR

L'idée générale de ce procédé est d'extraire des éléments de la série temporelle qui engendrent une inhomogénéité temporelle, ou inversement, nous souhaitons conserver un groupe de pixels qui conserve une homogénéité temporelle à partir du calcul de leur coefficient de variation. Le coefficient de variation CV est ensuite calculé de manière itérative et comparé à un seuil. A chaque itération, nous obtenons un nouveau vecteur de sortie où le pixel présentant la valeur la plus éloignée de la moyenne a été extraite. L'algorithme est répété jusqu'à ce que l'ensemble des pixels restants temporels satisfasse le critère d'homogénéité. La liste de pixels candidats peut être donc utilisée pour former une image représentative d'une scène figée. Deux approches on étés étudiées dans cette thèse pour former l'image FBR:

- La sélection aléatoire d'un pixel parmis la liste des pixels candidats (random pixels: RP)
- L'utilisation de tous les pixels candidats sous forme d'une moyenne incohérente (moyenne des amplitudes ou intensités) (multitemporal pixels: MP)

Ce procédé étant exécuté pour chaque case distance et azimuth dans la direction temporelle permet de garder la résolution et ainsi évite de mélanger spatialement des pixels pouvant représenter différents phénomènes physiques. La méthode a été développée initialement pour des signaux monopolarisés mais a été étendu a des signaux radar pouvant comporter plusieurs polarisations par une procédure effectuée en parrallèle pour chaque polarisation.

### D.5.2 Détection de changement à partir de l'image FBR

La sélection des pixels candidats pour représenter l'image FBR de la scène figée pouvant être exécutée de manière différentes, la détection de changement a été adaptée en conséquence. De manière classique, le GLRT (Generalized likelihood ratio test ou rapport de vraisemblance généralisé) est utilisé pour la détection de changement.

Dans le cas où la sélection des pixels est faite de manière aléatoire (RP), le test peut être effectué de manière classique car la statistique entre l'image FBR générée et l'image mission est supposée conservée.

Dans le cas où plusieurs pixels sont utilisés pour former l'image FBR (MP), le test statistique a été adapaté pour prendre en compte la différence entre le nombre d'échantillons en jeu entre l'image FBR et l'image mission.

D'un point de vue général, l'utilisation de la méthode RP améliore l'interprétation des résultats

de détection de changement car seulement les objets éphémères présents dans l'image mission sont supposés être détectés, cependant, les performences de détection restent équivalentes comparées a une détection bi-temporelle classique. La méthode MP montre qu'il est possible d'améliorer les performences de détection. Par simulation, il est possible d'observer une amélioration des performances de détection d'autant plus que le nombre de pixels stables en jeu dans la construction de l'image de fond est grand.

## D.6 Principaux résultats pour des applications concrètes de détection de cibles

Dans le but d'illustrer et d'évaluer les avantages de la méthode développée, nous proposons d'étudier différents scénario concret ou la détection de cibles est compromise: les zones portuaire où de forts rétrodiffuseurs sont présents (quais d'amarrage, infrastructures) et les zones forestières observées à basses fréquences où la contribution des troncs génère des forts signaux de rétrodiffusions.

### D.6.1 La surveillance maritime

La détection des navires en pleine mer est généralement effectuée avec une seule image SAR car le contraste entre le niveau de rétrodiffusion de la mer et celle d'un éventuel navire est assez fort. Dans les zones portuaires, plusieurs diffuseurs tels que les quais d'amarrage, les plates-formes industrielles, ou plus généralement les infrastructures portuaires, peuvent produire de forts signaux de rétrodiffusion. Cela rend plus difficile la détection des navires avec une seule image et génére des fausses alarmes. L'emploi d'une image FBR peut être une alternative intéressante dans les environnements portuaires pour détecter les navires amarrés dans les zones à forte fréquentation.

D'après les résultats obtenues, la méthode proposée est intéressante pour obtenir une carte de changement des objets éphémères, qui, dans le cas présent sont des bateaux. En particulier, son intérêt a été démontré pour la détection de cible dans un port industriel entre l'ile de Jurong Island et la principale ile de Singapour grâce à l'utilisation de signaux AIS .

Dans le cadre de l'étude sur la surveillance maritime, deux phénomènes majeures peuvent affecter notre méthode et doivent être étudiés dans le futur: l'état de la surface de la mer et l'effet de marée. En effet, Singapour se trouve dans une zone à faible effet de marée, et à l'intérieur des ports, on peut considérer que l'état de la mer reste relativement calme car protégé par les terres et infrastructures environnantes.

L'effet de l'état de la mer doit être vérifié dans différentes situations (état de la mer, résolution,

fréquence d'utilisation du capteur, etc.). L'effet de marée côtière est un phénomène qui cause également plusieurs problèmes (apparition de rochers par exemple) et peut corrompre l'estimation FBR de la scène puisque le fond évoluerait périodiquement. L'effet de marée étant un phénomène prévisible, nous pourrions joindre les acquisitions disponibles avec un état de marée donné lorsque la zone d'étude est soumise à un fort effet de marée. L'effet de marée pourrait alors être évité en calculant une image FBR par état de marée qui donnerait plus de précision sur l'estimation de fond de l'image sur une période donnée d'une part et un meilleur résultat de détection d'autre part.

### D.6.2 Les applications FoPen

Ce qui fait la spécificité et la difficulté de la détection de cibles sous couvert forestier est la forte rétrodiffusion issue de l'intéraction entre les troncs et le sol. La détection de changement est donc une méthode simple et efficace pour éliminer les contributions des troncs et ne garder que les contributions des objets éphémères présents dans la scène. Nous avons utilisés deux jeux de données issues de capteurs différents pour évaluer le comportement de la méthode développée.
Pour la première étude, nous avons évalué les performances pour la détection de véhicules (et réflecteur) cachés sous la canopée d'une forêt tropicale avec les données de la mission TROPISAR mesurées par le radar SETHI développé par l'ONERA (Office National d'Etudes et de Recherches Aérospatiales). Cette détection a été rendue possible grâce à l'utilisation de basses fréquences radar qui permettent de pénétrer à travers le feuillage et d'atteindre le sol. Nous avons comparé trois statistiques pour évaluer quantitativement le gain de l'utilisation de plusieurs acquisitions pour construire une scène FBR. Cependant, dans ce cas précis, il faut noter qu'il y a un court délai entre les acquisitions (2 à 7 jours) et entre la première et la dernière acquisition (22 jours). De plus, les acquisitions en bande P favorisent probablement une stabilité temporelle de la scène et semblent donc robustes aux variations temporelles intrinsèques de la végétation telles que la croissance de la végétation et les effets saisonniers. Il serait alors intéressant d'étudier une telle stratégie avec une durée d'acquisition plus longue sur la forêt tropicale pour mettre en évidence les éventuelles limitations introduites par les variations saisonnières de l'environnement.

Dans la seconde étude, nous nous sommes intéressés à l'utilisation de différentes configurations de vols (caps) présentent dans le jeu de donnée issue du challenge CARABAS-II mesuré par le FOI (Swedish Defense Research Agency) pour évaluer si la détection pouvait être améliorée par rapport à une détection de changement impliquant une seule image de référence et une image de mission. En considérant des caps d'acquisitions séparément, la détection des véhicules est bien

amélioré lors de l'utilisation de l'image FBR grâce à une suppression efficace de la contribution des troncs. Visuellement, les cibles sont bien mises en évidence et les courbes ROC calculées montrent une amélioration par rapport à une détection de type bi-date pour chaque cap. Par la suite, nous avons construit l'image FBR à partir de deux sets d'acquisitions avec des cap de vol rapprochés et évalué le gain sur la détection. Au vu des résultats, l'utilisation de plus d'images calculées avec un cap de vol proches améliore encore la détection par rapport à une détection bi-date. Cependant, il n'améliore pas la détection globale par rapport à un cadre FBR considérant un seul cap de vol à 225 degrés. La prise en compte de caps de vol fortement hétérogènes permet toujours une meilleure détection par rapport à un cas bi-date, mais cela diminue les performances globales. Il semble expérimentalement possible pour ce type de forêt (tronc long et fin) de considérer une symétrie azimutale de l'environnement et d'utiliser un cap de vol différent pour effectuer la détection de changement afin de mettre en évidence les véhicules sous le feuillage. Cependant, cette hypothèse est naturellement vraie en milieu forestier, cela génère de fausses alarmes là où la symétrie azimutale n'est pas respectée à proximité des routes ou des bordures de forêt.

## D.7 Conclusion

Le premier objectif de cette thèse a été de développer une méthodologie produisant une carte de changement qui met en évidence les cibles éphémères présentes dans une acquisition SAR donnée en bénéficiant de séries temporelles d'images SAR. Comme illustré, les techniques de détection de changement représentent une bonne solution pour mettre en évidence des cibles présentes dans des milieux comme les zones portuaires ou les forêts observées à basse fréquence grâce à la suppression des signaux de rétrodiffusion de l'environnement temporellement stable.

Étant donné que les images SAR sans cible ne sont pas disponibles en pratique dans les données en libre accès, notre démarche a été de bénéficier des séries temporelles disponibles pour générer une scène constituée uniquement d'un fond statique. Nous avons désigné cette image, l'image FBR, qui vise a représenter l'arrière-plan temporellement homogène de la scène, comme les bâtiments, les arbres, les infrastructures et le bruit de fond. Cette image ne correspond pas à une acquisition SAR réelle mais représente une acquisition qui aurait été acquise sans cibles éphémères.

Nous utilisons ensuite cette image pour visualiser la signature de cibles présente à une acquisition donnée.

### D.7.1 Principaux avantages de la méthode

La méthode proposée permet de mettre en évidence le contenu temporellement non-stationnaire présent dans une acquisition SAR donnée et donc la présence de cible éphémères commes les véhicules ou les bateaux. Elle rempli donc son premier objectif qui est de supprimer les effets non désirable des méthodes classiques bi-temporelles lorsque plusieurs cible se chevauchent temporellement.

D'un point de vue général, les choix de sélection aléatoires (RP) et multitemporels (MP) permettent de mettre en évidence les cibles éphémères et sont satisfaisante pour les applications étudiées. Une amélioration de la détection des cibles est constatée dans le cas MP d'autant plus que le nombre de pixels stable pour générer l'image FBR est grand.

### D.7.2 Principaux inconvénients

Les événements durable dans le temps comme la construction ou la destruction de bâtiments peuvent induire des variations susceptibles de mener à de mauvaises interprétations sur la détection. Considérant les futures missions avec un temps de revisite faible (quelques heures), nous pouvons considérer ces événements comme long et durables et peuvent être solutionnés par une mise à jour de l'image FBR au vu des résultats de détection de changement.

Dans d'autres environnements comme les forêts, nous pourrions observer des effets saisonniers si l'acquisition est faite sur une longue période. Nous n'avons pas été confrontés à ce genre de variations dans nos études mais elles sont a considérer pour les travaux futurs.

## D.8 Perspectives

Dans cette thèse, nous nous sommes intéréssés à une nouvelle approche de détection de changement basée sur la construction d'une image SAR fictive, dénuée de cibles mobiles. Pour ce faire, nous avons défini trois étapes: la sélection des pixels stables temporellement, la formation de l'image SAR fictive et la détection des changements entre cette image et toute autre image SAR collectée. Chacune de ces étapes peut être étudiée, améliorée ou au moins modifiée.

### D.8.1 Perspectives techniques

Nous avons vu que le coefficient de variation $CV_{theo}$ permet de sélectionner des pixels stables. L'écart type de cette valeur diminue avec $\sqrt{D}$, $D$ étant le nombre de dates dans la série temporelle. Idéalement, plus le nombre de dates est grand, meilleure est l'estimation de $CV_{theo}$. Cette grandeur théorique est cependant indépendante de la fréquence et de la polarisation et peut être limitante dans les cas où l'environnement peut être plus sensible à certaines polarisation. L'utilisation seulement de l'amplitude pour la sélection des pixels stable peut poser question et peut être complétée par une stabilité de phase entre canaux polarimétriques pour chaque acquisition.
La notion de qualité de l'image FBR est a étudier plus profondément, voir même à définir. Dans cette thèse, nous avons étudiés l'impact du nombre de dates utilisées pour générer cette image et avons vu qu'il était possible d'utiliser 20 dates dans le cas du dataset UAVSAR et un trentaine de dates dans le cas de Singapour. En pratique, de combien de dates avons-nous besoin au minimum? Y a-t-il un maximum? Ceci peut être lié directement à différent facteurs comme l'activité de la zone considérée et l'heure à laquelle le capteur passe sur la scène. Il est essentiel par la suite de construire un jeu de donné avec une vérité terrain afin d'étudier plus profondément cette question. En effet, les jeux de données que nous avons utilisé avec vérité terrain étaient constitués d'un faible nombre de date rendant cette expérience difficile à mener.

Finalement, dans le cadre de détection automatique de cibles, cette méthode peut être utilisée comme "prescreening" pour mettre en évidence la présence de potentiels cibles, qui par la suite peut être combinée à des étapes post-traitement réfutant ou affirmant la présence d'une cible par analyse morphologique (forme et taille de l'objet détecté).

### D.8.2 Extension vers d'autres applications

Dans d'autres domaines, comme l'étude des déserts, on peut s'attendre à ne voir aucun changement, quelle que soit la durée de la série chronologique. Cependant, en raison des capacités de pénétration élevées des basses fréquences à travers le sable sec, nous pouvons nous attendre à détecter des changements sous la surface reflétant la présence de chenaux potentillement actifs comme dans [99]. L'utilisation de fréquences différentes peut être introduite pour générer différentes images de référence. Par exemple, nous nous attendons à ce que les hautes fréquences (Sentinel-1 en bande C par exemple) donnent une information liée à la surface ou aux sous-surfaces supérieures du sol alors que les fréquences plus basses caractériseraient les sous-surfaces puisqu'elles peuvent pénétrer plus profondément à travers le sable sec. Cependant, cela impliquera des problèmes techniques liés

aux différences de géométrie d'acquisition et doit être ainsi considéré dans les études.

Nous nous sommes intéréssés dans cette étude à de petites cibles mobiles mais les changements peuvent être considérés bien évidemment pour des phénomènes étendu comme les innondations ou les activités illégales dans les forêts (orpaillage par example).

Finalement, l'utilisation seule de l'image FBR peut être envisagée car elle représente les éléments stable dans la série temporelles et peut permettre de mettre en évidence des rétrodiffuseurs permanent même de faible amplitude dans des environnement où il n'était pas forcément attendu d'en voir grâce à la diminution du bruit de châtoiment.

# Bibliography


[1] A. Mokadem, *Analysis of scattering by urban areas in the frame of NLOS target detection in SAR images.* PhD thesis, Supélec, 2014.

[2] R. Durand, *Processeurs SAR basés sur des détecteurs de sous-espaces.* PhD thesis, Université Paris 10, November 2007.

[3] F. Brigui, *Algorithmes d'imagerie SAR polarimétriques basés sur des modèles à sous-espace : application à la détection de cible sous couvert forestier.* PhD thesis, Université Paris Ouest Nanterre La Défense, December 2010.

[4] K. El-Darymli, P. McGuire, D. Power, and C. Moloney, "Target detection in Synthetic Aperture Radar imagery: A State-of-the-Art Survey," *Journal of Applied Remote Sensing*, vol. 7, pp. 071598–071598, 01 2013.

[5] L. M. H. Ulander, P. Frolind, A. Gustavsson, H. Hellsten, T. Jonsson, B. Larsson, and G. Stenstrom, "Performance of the CARABAS-II VHF-band synthetic aperture radar," in *IGARSS 2001. Scanning the Present and Resolving the Future. Proceedings. IEEE 2001 International Geoscience and Remote Sensing Symposium*, vol. 1, pp. 129–131 vol.1, 2001.

[6] H. Oriot, "Change Detection Analysis for Under-Cover Detection in L and UHF Bands," in *ESA Special Publication*, vol. 713 of *ESA Special Publication*, p. 43, Aug. 2013.

[7] C. Guaragnella and T. D'Orazio, "A Data-Driven Approach to SAR Data-Focusing," *Sensors*, vol. 19, no. 7, 2019.

[8] L. Thirion-Lefevre, R. Guinvarc'h, and E. Colin-Koeniguer, "The Combined Effect of Orientation Angle and Material on PolSAR Images of Urban Areas," *Remote Sensing*, vol. 12, p. 1632, May 2020.

[9] "User Guide Sentinel 1." `https://sentinel.esa.int/web/sentinel/user-guides/sentinel-1-sar/acquisition-modes`. accessed on 25/08/2020.

[10] "Change Detection in multitemporal remote sensing images." `https://earth.esa.int/documents/973910/2642313/LB1to3.pdf`. accessed on 10/07/2020.

[11] A. Mian, *Contributions to SAR Image Time Series Analysis.* PhD thesis, Université Paris-Saclay, September 2019.

[12] "Image template." `https://commons.wikimedia.org/wiki/File:Roc-draft-xkcd-style.svg`. accessed on 28 August 2020.

[13] T. Bouwmans, F. Porikli, B. Höferlin, and A. Vacavant, *Handbook on Background Modeling and Foreground Detection for Video Surveillance*. Taylor and Francis Group, CRC Press, 2014.

[14] C. Santamaria, M. Stasolla, V. Fernandez Arguedas, P. Argentieri, M. Alvarez, and H. Geridanus, "Sentinel-1 maritime surveillance," tech. rep., European Commission, 2015.

[15] L. Thirion, I. Chênerie, and C. Galy, "Application of a coherent model in simulating the backscattering coefficient of a mangrove forest," *Waves in Random Media*, vol. 14, no. 2, pp. S299–S316, 2004.

[16] M. Lundberg, L. M. H. Ulander, W. E. Pierson, and A. Gustavsson, "A challenge problem for detection of targets in foliage," in *Algorithms for Synthetic Aperture Radar Imagery XIII* (E. G. Zelnio and F. D. Garber, eds.), vol. 6237, pp. 160 – 171, International Society for Optics and Photonics, SPIE, 2006.

[17] P. C. Dubois-Fernandez, T. Le Toan, S. Daniel, H. Oriot, J. Chave, L. Blanc, L. Villard, M. W. J. Davidson, and M. Petit, "The TropiSAR Airborne Campaign in French Guiana: Objectives, Description, and Observed Temporal Behavior of the Backscatter Signal," *IEEE Transactions on Geoscience and Remote Sensing*, vol. 50, no. 8, pp. 3228–3241, 2012.

[18] C. Wiley, "Pulsed doppler radar methods and apparatus," U.S. Patent 3196436, Aug. 1954.

[19] C. W. Sherwin, J. P. Ruina, and R. D. Rawcliffe, "Some Early Developments in Synthetic Aperture Radar Systems," *IRE Transactions on Military Electronics*, vol. MIL-6, no. 2, pp. 111–115, 1962.

[20] S. Quegan, T. Le Toan, J. Chave, J. Dall, J.-F. Exbrayat, D. H. T. Minh, M. Lomas, M. M. D'Alessandro, *et al.*, "The European Space Agency BIOMASS mission: Measuring forest above-ground biomass from space," *Remote Sensing of Environment*, vol. 227, pp. 44 – 60, 2019.

[21] "Ionospheric Effects on SAR, InSAR and SAR Polarimetry - Theory and Experiences with ALOS/PALSAR." `http://earth.esa.int/fringe07/participants/578/pres_578_meyer.pdf`. accessed on 21/08/2020.

[22] F. Ulaby, D. Long, W. Blackwell, C. Elachi, A. Fung, C. Ruf, K. Sarabandi, H. Zebker, and J. Van Zyl, *Microwave Radar and Radiometric Remote Sensing.* University of Michigan Press, 2014.

[23] K. Van Tricht, A. Gobin, S. Gilliams, and I. Piccard, "Synergistic Use of Radar Sentinel-1 and Optical Sentinel-2 Imagery for Crop Mapping: A Case Study for Belgium," *Remote Sensing*, vol. 10, p. 1642, 10 2018.

[24] T. Sarzynski, X. Giam, L. Carrasco, and J. S. H. Lee, "Combining Radar and Optical Imagery to Map Oil Palm Plantations in Sumatra, Indonesia, Using the Google Earth Engine," *Remote Sensing*, vol. 12, p. 1220, Apr 2020.

[25] B. Mahafza, *Radar Systems Analysis and Design Using MATLAB.* Chapman and Hall/CRC, 2005.

[26] M. Soumekh, *Synthetic Aperture Radar Signal Processing: with MATLAB Algorithms.* John Wiley & Sons, 1999.

[27] C. Ozdemir, *Inverse Synthetic Aperture Radar Imaging With MATLAB Algorithms.* Wiley Series in Microwave and Optical Engineering, Wiley, 2012.

[28] H. Oriot, *Imagerie SAR haute résolution aéroportée.* Habilitation à diriger des recherches, Universite de Paris-Sud centre d'Orsay, May 2018.

[29] J.-S. Lee and E. Pottier, *Polarimetric radar imaging: from basics to applications.* CRC Press, 2017.

[30] P. Paillou, "Mapping Palaeohydrography in Deserts: Contribution from Space-Borne Imaging Radar," *Water*, vol. 9, no. 3, 2017.

[31] M. Schlund and M. W. J. Davidson, "Aboveground Forest Biomass Estimation Combining L- and P-Band SAR Acquisitions," *Remote Sensing*, vol. 10, no. 7, 2018.

[32] R. Treuhaft, F. Goncalves, J. Santos, M. Keller, M. Palace, S. Madsen, F. Sullivan, and P. M. De Alencastro Graça, "Tropical-Forest Biomass Estimation at X-Band From the Spaceborne TanDEM-X Interferometer," *Geoscience and Remote Sensing Letters, IEEE*, vol. 12, pp. 239–243, 02 2015.

[33] L. M. H. Ulander, M. Lundberg, W. Pierson, and A. Gustavsson, "Change detection for low-frequency SAR ground surveillance," *IEE Proceedings - Radar, Sonar and Navigation*, vol. 152, no. 6, pp. 413–420, 2005.

[34] B. Hallberg, G. S. Lars, M. H. Ulander, and P. Frolind, "Individual tree detection using CARABAS-II," in *IGARSS 2003. 2003 IEEE International Geoscience and Remote Sensing Symposium. Proceedings (IEEE Cat. No.03CH37477)*, vol. 3, pp. 1639–1641, 2003.

[35] F. k. Li and W. T. K. Johnson, "Ambiguities in Spaceborne Synthetic Aperture Radar Systems," *IEEE Transactions on Aerospace and Electronic Systems*, vol. AES-19, no. 3, pp. 389–397, 1983.

[36] A. Freeman, "On ambiguities in SAR design," *EUSAR 2006: 6th European Conference on Synthetic Aperture Radar*, 2006.

[37] S. Cloude, *Polarimetry: the characterisation of polarisation effects in EM scattering*. PhD thesis, University of Birmingham, 1987.

[38] L. Thirion-Lefevre and R. Guinvarc'h, "The double Brewster angle effect," *Comptes Rendus Physique*, vol. 19, no. 1, pp. 43 – 53, 2018.

[39] E. Krogager, "New decomposition of the radar target scattering matrix," *Electronics Letters*, vol. 26, no. 18, pp. 1525–1527, 1990.

[40] W. L. Cameron, N. N. Youssef, and L. K. Leung, "Simulated polarimetric signatures of primitive geometrical shapes," *IEEE Transactions on Geoscience and Remote Sensing*, vol. 34, no. 3, pp. 793–803, 1996.

[41] S. R. Cloude, "Target decomposition theorems in radar scattering," *Electronics Letters*, vol. 21, no. 1, pp. 22–24, 1985.

[42] W.-M. Boerner, "Basics of SAR Polarimetry I." `https://apps.dtic.mil/dtic/tr/fulltext/u2/a471015.pdf`, 02 2007. accessed on 21/07/2020.

[43] J. M. Nicolas, "Application de la Transformée de Mellin: Etude des Lois Statistiques de L'imagerie Cohérente," tech. rep., Télécom Paris: Paris, France, 2006.

[44] J. W. Goodman, "Some fundamental properties of speckle," *J. Opt. Soc. Am.*, vol. 66, pp. 1145–1150, Nov 1976.

[45] K. Conradsen, A. A. Nielsen, J. Schou, and H. Skriver, "A test statistic in the complex Wishart distribution and its application to change detection in polarimetric SAR data," *IEEE Transactions on Geoscience and Remote Sensing*, vol. 41, pp. 4–19, Jan 2003.

[46] A. P. Doulgeris and T. Eltoft, "Scale Mixture of Gaussians Modelling of Polarimetric SAR Data," in *Proceedings of the 7th Nordic Signal Processing Symposium - NORSIG 2006*, pp. 18–21, 2006.

[47] C. Oliver and S. Quegan, *Understanding Synthetic Aperture Radar Images*. EngineeringPro collection, SciTech Publ., 2004.

[48] "Sentinel Application Platform (SNAP)." `http://step.esa.int/main/toolboxes/snap/`. accessed on 20 April 2020.

[49] E. Pottier, L. Ferro-Famil, M. Fitrzyk, and Y. Desnos, "PolSARpro-Bio: An ESA Educational Toolbox Used For Self-Education in the Field of PolSAR, Pol-InSAR AND Pol-TomoSAR Data Analysis," in *IGARSS 2018 - 2018 IEEE International Geoscience and Remote Sensing Symposium*, pp. 6568–6571, 2018.

[50] "StaMPS/MTI Manual." `https://homepages.see.leeds.ac.uk/~earahoo/stamps/StaMPS_Manual_v3.1.pdf`. accessed on 25/07/2020.

[51] R. Abdelfattah and J. M. Nicolas, "InSAR image co-registration using the Fourier–Mellin transform," *International Journal of Remote Sensing*, vol. 26, no. 13, pp. 2865–2876, 2005.

[52] "Copernicus Open Access Hub." `https://scihub.copernicus.eu/`. accessed on 21/08/2020.

[53] S. Hensley, K. Wheeler, G. Sadowy, C. Jones, S. Shaffer, H. Zebker, T. Miller, B. Heavey, E. Chuang, *et al.*, "The UAVSAR instrument: Description and first results," in *2008 IEEE Radar Conference*, pp. 1–6, 2008.

[54] "Data Search - UAVSAR." `https://uavsar.jpl.nasa.gov/cgi-bin/data.pl`. accessed on 21/08/2020.

[55] M. Davidson, "Copernicus L-band SAR Mission Requirements Document," tech. rep., European Space Agency, 10 2018.

[56] R. Torres, S. Lokas, H. L. Moller, M. Zink, and D. M. Simpson, "The TerraSAR-L mission and system," in *IGARSS 2004. 2004 IEEE International Geoscience and Remote Sensing Symposium*, vol. 7, pp. 4519–4522 vol.7, 2004.

[57] M. Preiss, D. Gray, and N. Stacy, "Detecting scene changes using synthetic aperture radar interferometry," *Geoscience and Remote Sensing, IEEE Transactions on*, vol. 44, pp. 2041 – 2054, 09 2006.

[58] P. Lombardo and C. J. Oliver, "Maximum likelihood approach to the detection of changes between multitemporal SAR images," *IEE Proceedings - Radar, Sonar and Navigation*, vol. 148, no. 4, pp. 200–210, 2001.

[59] L. M. Novak, "Change detection for multi-polarization multi-pass SAR," in *Algorithms for Synthetic Aperture Radar Imagery XII* (E. G. Zelnio and F. D. Garber, eds.), vol. 5808, pp. 234 – 246, International Society for Optics and Photonics, SPIE, 2005.

[60] J. Inglada and G. Mercier, "A New Statistical Similarity Measure for Change Detection in Multitemporal SAR Images and Its Extension to Multiscale Change Analysis," *IEEE Transactions on Geoscience and Remote Sensing*, vol. 45, no. 5, pp. 1432–1445, 2007.

[61] F. Bovolo and L. Bruzzone, "A wavelet-based change-detection technique for multitemporal SAR images," in *International Workshop on the Analysis of Multi-Temporal Remote Sensing Images, 2005.*, pp. 85–89, 2005.

[62] T. T. Le, *Change information extraction from Synthetic Aperture Radar Image Time Series*. PhD thesis, Université Grenoble Alpes, October 2015.

[63] S. Plank, S. Karg, and S. Martinis, "Full-polarimetric burn scar mapping – the differences of active fire and post-fire situations," *International Journal of Remote Sensing*, vol. 40, no. 1, pp. 253–268, 2019.

[64] X. Su, C.-A. Deledalle, F. Tupin, and H. Sun, "NORCAMA: Change analysis in SAR time series by likelihood ratio change matrix clustering," *ISPRS Journal of Photogrammetry and Remote Sensing*, vol. 101, pp. 247 – 261, 2015.

[65] C. Bayındır, J. D. Frost, and C. F. Barnes, "Assessment and Enhancement of SAR Noncoherent Change Detection of Sea-Surface Oil Spills," *IEEE Journal of Oceanic Engineering*, vol. 43, no. 1, pp. 211–220, 2018.

[66] S. Karimzadeh, M. Matsuoka, M. Miyajima, B. Adriano, A. Fallahi, and J. Karashi, "Sequential SAR Coherence Method for the Monitoring of Buildings in Sarpole-Zahab, Iran," *Remote Sensing*, vol. 10, p. 1255, Aug 2018.

[67] W. Zhao, C. Deledalle, L. Denis, H. Maître, J. Nicolas, and F. Tupin, "Ratio-Based Multitemporal SAR Images Denoising: RABASAR," *IEEE Transactions on Geoscience and Remote Sensing*, vol. 57, no. 6, pp. 3552–3565, 2019.

[68] W. Zhao, *Multitemporal SAR images denoising and change detection : applications to Sentinel-1 data*. PhD thesis, Université Paris-Saclay, Jan. 2019.

[69] D. Ciuonzo, V. Carotenuto, and A. De Maio, "On Multiple Covariance Equality Testing with Application to SAR Change Detection," *IEEE Transactions on Signal Processing*, vol. 65, no. 19, pp. 5078–5091, 2017.

[70] A. Mian, G. Ginolhac, J. Ovarlez, and A. M. Atto, "New Robust Statistics for Change Detection in Time Series of Multivariate SAR Images," *IEEE Transactions on Signal Processing*, vol. 67, no. 2, pp. 520–534, 2019.

[71] R. Touzi, A. Lopes, and P. Bousquet, "A statistical and geometrical edge detector for SAR images," *IEEE Transactions on Geoscience and Remote Sensing*, vol. 26, no. 6, pp. 764–773, 1988.

[72] T. T. Le, A. Atto, E. Trouvé, and J.-M. Nicolas, "Temporal adaptative filtering of SAR image time-series based on the detection of stable and changed areas," in *5th TerraSAR-X / 4th TanDEM-X Science Team Meeting - 2013*, (Oberpfaffenhofen, Germany), p. 4 pages, June 2013.

[73] E. Colin Koeniguer and J.-M. Nicolas, "Change Detection Based on the Coefficient of Variation in SAR Time-Series of Urban Areas," *Remote Sensing*, vol. 12, p. 2089, Jun 2020.

[74] A. Ferretti, C. Prati, and F. Rocca, "Permanent scatterers in SAR interferometry," *IEEE Transactions on Geoscience and Remote Sensing*, vol. 39, no. 1, pp. 8–20, 2001.

[75] G. Quin, B. Pinel-Puysségur, J. Nicolas, and P. Loreaux, "Mimosa: An automatic change detection method for sar time series," *IEEE Transactions on Geoscience and Remote Sensing*, vol. 52, no. 9, pp. 5349–5363, 2014.

[76] E. Koeniger, J.-M. Nicolas, B. Pinel-Puyssegur, J.-M. Lagrange, and F. Janez, "Visualisation des changements sur séries temporelles radar : méthode REACTIV Evaluée à l'échelle mondiale sous Google Earth Engine," *Revue Française de Photogrammétrie et de Télédétection*, pp. 99–108, sept. 2018.

[77] K. Conradsen, A. A. Nielsen, and H. Skriver, "Determining the Points of Change in Time Series of Polarimetric SAR Data," *IEEE Transactions on Geoscience and Remote Sensing*, vol. 54, no. 5, pp. 3007–3024, 2016.

[78] N. Otsu, "A Threshold Selection Method from Gray-Level Histograms," *IEEE Transactions on Systems, Man, and Cybernetics*, vol. 9, no. 1, pp. 62–66, 1979.

[79] Y. Bazi, L. Bruzzone, and F. Melgani, "An unsupervised approach based on the generalized Gaussian model to automatic change detection in multitemporal SAR images," *Geoscience and Remote Sensing, IEEE Transactions on*, vol. 43, pp. 874 – 887, 05 2005.

[80] B. G. Palm, D. I. Alves, V. T. Vu, M. I. Pettersson, F. M. Bayer, R. J. Cintra, R. Machado, P. Dammert, and H. Hellsten, "Autoregressive model for multi-pass SAR change detection based on image stacks," in *Image and Signal Processing for Remote Sensing XXIV* (L. Bruzzone and F. Bovolo, eds.), vol. 10789, pp. 385 – 393, International Society for Optics and Photonics, SPIE, 2018.

[81] O. Barnich and M. Van Droogenbroeck, "ViBe: A Universal Background Subtraction Algorithm for Video Sequences," *IEEE Transactions on Image Processing*, vol. 20, no. 6, pp. 1709–1724, 2011.

[82] I. Halfaoui, F. Bouzaraa, and O. Urfalioglu, "CNN-based initial background estimation," in *2016 23rd International Conference on Pattern Recognition (ICPR)*, pp. 101–106, 2016.

[83] J. Scott, M. A. Pusateri, and D. Cornish, "Kalman filter based video background estimation," in *2009 IEEE Applied Imagery Pattern Recognition Workshop (AIPR 2009)*, pp. 1–7, 2009.

[84] S. N. Anfinsen, A. P. Doulgeris, and T. Eltoft, "Estimation of the Equivalent Number of Looks in Polarimetric Synthetic Aperture Radar Imagery," *IEEE Transactions on Geoscience and Remote Sensing*, vol. 47, no. 11, pp. 3795–3809, 2009.

[85] D. Crisp, "The state-of-the-art in ship detection in Synthetic Aperture Radar imagery," tech. rep., Department of Defense, Australian Government, 05 2004.

[86] S. Brusch, S. Lehner, T. Fritz, M. Soccorsi, A. Soloviev, and B. Schie, "Ship surveillance with TerraSAR-X," *Geoscience and Remote Sensing, IEEE Transactions on*, vol. 49, pp. 1092 – 1103, 04 2011.

[87] K. El-Darymli, P. McGuire, D. Power, and C. Moloney, "Target detection in Synthetic Aperture Radar imagery: A State-of-the-Art Survey," *Journal of Applied Remote Sensing*, vol. 7, pp. 071598–071598, 01 2013.

[88] Zili Shan, C. Wang, H. Zhang, and Bo Zhang, "Ocean-land segmentation based on active contour model for SAR imagery," in *2010 International Conference on Computer and Communication Technologies in Agriculture Engineering*, vol. 1, pp. 215–218, 2010.

[89] P. Iervolino, *Ship detection with SAR : modelling, designing and real data validation.* PhD thesis, University of Surrey, 2016.

[90] A. Arnaud, "Ship detection by SAR interferometry," in *IEEE 1999 International Geoscience and Remote Sensing Symposium. IGARSS'99 (Cat. No.99CH36293)*, vol. 5, pp. 2616–2618 vol.5, 1999.

[91] C. Brekke, S. Anfinsen, and Y. Larsen, "Subband Extraction Strategies in Ship Detection With the Subaperture Cross-Correlation Magnitude," *IEEE Geoscience and Remote Sensing Letters*, vol. 10, pp. 786–790, 07 2013.

[92] R. Z. Schneider, K. P. Papathanassiou, I. Hajnsek, and A. Moreira, "Polarimetric and interferometric characterization of coherent scatterers in urban areas," *IEEE Transactions on Geoscience and Remote Sensing*, vol. 44, no. 4, pp. 971–984, 2006.

[93] A. Marino, M. Sanjuan-Ferrer, I. Hajnsek, and K. Ouchi, "Ship Detection with Spectral Analysis of Synthetic Aperture Radar: A Comparison of New and Well-Known Algorithms," *Remote Sensing*, vol. 7, p. 5416–5439, Apr 2015.

[94] L. M. Novak, G. J. Owirka, and C. M. Netishen, "Performance of a High-Resolution Polarimetric SAR Automatic Target Recognition System." `https://archive.ll.mit.edu/publications/journal/pdf/vol06_no1/6.1.2.polarimetricsar.pdf`. accessed on 10 April 2020.

[95] D. Velotto, M. Soccorsi, and S. Lehner, "Azimuth ambiguities removal for ship detection using full polarimetric X-band SAR data," in *2012 IEEE International Geoscience and Remote Sensing Symposium*, pp. 7621–7624, 2012.

[96] R. Durand, G. Ginolhac, L. Thirion-Lefevre, and P. Forster, "Back Projection Version of Subspace Detector SAR Processors," *IEEE Transactions on Aerospace and Electronic Systems*, vol. 47, no. 2, pp. 1489–1497, 2011.

[97] F. Brigui, G. Ginolhac, L. Thirion-Lefevre, and P. Forster, "New SAR target imaging algorithm based on oblique projection for clutter reduction," *IEEE Transactions on Aerospace and Electronic Systems*, vol. 50, no. 2, pp. 1118–1137, 2014.

[98] L. Novak, "FOPEN change detection experiments using a CARABAS public release data set," in *Algorithms for Synthetic Aperture Radar Imagery XVII* (E. G. Zelnio and F. D. Garber, eds.), vol. 7699, pp. 292 – 301, International Society for Optics and Photonics, SPIE, 2010.

[99] P. Paillou, S. Lopez, E. Marais, and K. Scipal, "Mapping Paleohydrology of the Ephemeral Kuiseb River, Namibia, from Radar Remote Sensing," *Water*, vol. 12, pp. 1441 – 1454, 05 2020.

[100] M. Sanjuan-Ferrer, I. Hajnsek, and K. Papathanassiou, "Detection of coherent scatterers in SAR data: application for urban environments," pp. 1–4, 2014.

université PARIS-SACLAY

ÉCOLE DOCTORALE
Physique et ingénierie : Electrons, Photons, Sciences du vivant (EOBE)

**Titre:** Une nouvelle approche pour la détection de changement dans les série temporelles d'images SAR: application à la détection de cibles

**Mots clés:** Détection de changement, détection de cibles, SAR

**Résumé:** La détection de cibles telles que des navires ou des véhicules dans les images SAR (Synthetic Aperture radar) est un défi important pour la surveillance et la sécurité. Dans certains environnements tels que les zones urbaines, portuaires ou les forêts observées à basses fréquences radar, la détection de ces objets devient difficile en raison des propriétés de rétrodiffusion élevées de l'environnement. Pour résoudre ce problème, la détection de changement (CD) entre différentes images SAR permet de supprimer l'effet de l'environnement et ainsi une meilleur détection des cibles. Cependant, dans différents environnements à forte fréquentation, un chevauchement temporel des cibles peut se produire et génère une erreur d'interprétation possible car l'issue de la détection de changement repose sur une différence relative entre des objets de tailles ou de propriétés différentes. C'est un problème critique lorsque le but est de visualiser et d'obtenir le nombre d'objets à une acquisition donnée, dans les zones à fortes fréquentations comme les ports ou les zones urbaines. Idéalement, cette détection de changement devrait se réaliser entre une image constituée seulement de l'environnement et une image contenant les cibles d'intêrets. Grâce à l'accessibilité actuelle aux séries temporelles d'images SAR, nous proposons de générer une scène de référence (Frozen Background Image - FBR) qui n'est constituée que de l'environnement temporellement statique. La détection de changement entre une image SAR et cette image FBR vise donc a obtenir une map des cibles éphémères présentes. Cette stratégie a été mise en œuvre pour la détection des navires en milieu portuaire et dans le contexte de véhicules cachés sous couvert forestier.

**Title:** A new strategy for change detection in SAR time-series: application to target detection

**Keywords:** Change detection, target detection, SAR images

**Abstract:** The detection of targets such as ships or vehicles in SAR (Synthetic Aperture Radar) images is an essential challenge for surveillance and security purpose. In some environments such as urban areas, harbor areas or forest observed at low radar frequencies, detecting these objects becomes difficult due to the high backscattering properties of the surrounding background. To overcome this issue, change detection (CD) between SAR images enables to cancel the background and highlight successfully targets present within the scene. However, in several environments, a temporal overlapping of targets may occur and generates possible misinterpretation because the outcome relies on the relative change between objects of different sizes or properties. This is a critical issue when the purpose is to visualize and obtain the number of targets at a specific day in high attendance areas such as harbors or urban environments. Ideally, this change detection should occur between a target-free image and one with possible objects of interest. With the current accessibility to SAR time-series, we propose to compute a frozen background reference (FBR) image that will consists only in the temporally static background. Performing change detection from this FBR image and any SAR image aim to highlight the presence of ephemeral targets. This strategy has been implemented for ship detection in harbor environment and in the context of vehicles hidden under foliage.

Université Paris-Saclay
Espace Technologique / Immeuble Discovery
Route de l'Orme aux Merisiers RD 128 / 91190 Saint-Aubin, France